

BOSTON UNIVERSITY
GRADUATE SCHOOL OF ARTS AND SCIENCES

Dissertation

**SINGLE MOLECULE CONDUCTANCE SPECTROSCOPY: PROBING THE
GOLD-BIO INTERFACE AT THE ATOMIC SCALE**

by

XIAOYUN PAN

B.S., Pennsylvania State University, 2017

M.S., Boston University, 2019

Submitted in partial fulfillment of the
requirements for the degree of
Doctor of Philosophy

2024

© 2024 by
XIAOYUN PAN
All rights reserved

Approved by

First Reader

Maria Kamenetska, Ph.D.
Assistant Professor of Chemistry
Assistant Professor of Physics
Assistant Professor of Materials Science and Engineering

Second Reader

Linda H. Doerrer, Ph.D.
Professor of Chemistry
Professor of Materials Science and Engineering

ACKNOWLEDGMENTS

First and foremost, I would like to express my deepest gratitude to my advisor, Prof. Masha Kamenetska. Her guidance, advice, and mentorship have been invaluable throughout this journey. I am grateful for her belief in me and my abilities; this achievement would not have been possible without her.

I am also immensely grateful to my second reader, Prof. Linda Doerrer, for her insightful input and thorough review of my work. Her insightful feedback has been instrumental in refining this thesis. I want to thank my dissertation committee members, including Prof. Björn Reinhard, Prof. Ksenia Bravaya, and Prof. Xi Ling. Their advice and expertise have contributed significantly to the quality of this work.

I am grateful for the opportunity to work alongside the members of the Kamenetska group: Brent Lawson, Hannah Skipper, Daniel Jackson, Brian Dawes, Zelin Miao, Favian Liu, Sigifredo Luna, and Nicolas Miller. The journey through graduate school would not have been as fun and enjoyable without the supportive and intellectually challenging environment created by this diverse and interdisciplinary team. I have learned a great deal from each of you, and I am thankful for the unique perspectives and insights you have brought to our collective work.

I am profoundly grateful to Brent Lawson for his substantial theoretical contributions to Chapters 3 and 4. His mentorship, particularly in calculation and instrumentation techniques, has been invaluable in this journey. I want to extend my sincere thanks to the Vazquez group at the Czech Academy of Sciences. Their theoretical work and insightful contributions were integral to the development of Chapter 4, and I am

immensely thankful for their partnership. Additionally, I sincerely appreciate Cheng Qian and Prof. Lu Wang from Rutgers University. Their theoretical acumen and significant contributions to Chapter 5 significantly shaped my research. I am also grateful to Andrea M Rustad, Amber Chow, and Katherine Matthews (Haverford College) for their collaborative efforts and contributions to Chapters 3, 5, and 6, respectively.

Finally, I would like to express my deepest gratitude to my family; their faith in my abilities and their understanding during the challenging times of this process have been invaluable. Especially, I would like to thank my husband, I-Yang. Your support and belief in me have been a constant source of strength throughout this journey. This achievement would not have been possible without you by my side. Thank you for your love, patience, and understanding. This thesis would not have been possible without the support and contributions of all these individuals. I am truly grateful for their love and belief in me.

Lastly, I believe that we, as a society, often do not give ourselves enough credit for our hard work. I would like to share a quote from the esteemed American artist, Calvin Cordozar Broadus Jr.:

“I want to thank me for believing in me, I want to thank me for doing all this hard work. I wanna thank me for having no days off. I wanna thank me for never quitting. I wanna thank me for always being a giver and trying to give more than I receive. I wanna thank me for trying to do more right than wrong. I wanna thank me for being me at all times.”

**SINGLE MOLECULE CONDUCTANCE SPECTROSCOPY: PROBING THE
GOLD-BIO INTERFACE AT THE ATOMIC SCALE**

XIAOYUN PAN

Boston University Graduate School of Arts and Sciences, 2024

Major Professor: Maria Kamenetska, Assistant Professor of Chemistry, Physics, and
Materials Science and Engineering

ABSTRACT

This thesis uses single molecule conductance spectroscopy to probe the binding mechanisms and conductance characteristics of various biologically relevant molecules with gold at the atomic level. Firstly, we identify imidazole as a pH-activated linker for forming stable single gold molecule junctions, which present several distinct configurations and reproducible electrical characteristics. We then examine the resulting conductance signatures and identify corresponding binding geometries, which involve up to four imidazole molecules binding in the junction in parallel. In addition, we discover the distinct conductance signatures that indicate the in-situ formation of molecule-metal-molecule chains within the molecular junction.

Building on this foundation, the investigation continues into the origin of the conductance enhancement observed in benzimidazole dimers compared to imidazole dimers. Density Functional Theory (DFT) calculations reveal that the parallel stacking of two benzimidazoles, due to the large π system between electrodes, represents the most energetically favorable configuration, leading to dimer conductance enhancement. The smaller size and greater conformational freedom of imidazole enable it to access a variety of stacking angles. Having understood the underlying mechanism, we use substituents to

promote the cooperative in situ assembly of imidazole derivatives into a parallel binding configuration, subsequently enhancing conductance.

Next, we shift our focus to adenine, one of the most important biological building blocks of deoxyribonucleic acid (DNA). By using structurally similar molecules, we can assign different conductance signals to various binding configurations of adenine. This approach also enables the differentiation between adenine and its biological derivatives, 2'-deoxyadenosine and 6-methyladenine. Using single molecule conductance signals, we demonstrate the potential of single molecule conductance spectroscopy as a biosensing platform.

Finally, we present a detailed study of the pH-activated intramolecular conductance features of histamine. By employing histamine and its derivatives, we associate different conductance features with specific binding sites. DFT calculation is used to simulate the different ethylamine configurations of histamine in molecular junctions, and flicker noise analysis is applied to identify and assign one of the conductance features to a hydrogen bond-assisted binding configuration. These results and insights collectively establish single molecule conductance spectroscopy as a robust platform for studying complex gold-biomolecule interactions.

TABLE OF CONTENTS

ACKNOWLEDGMENTS	v
ABSTRACT.....	vii
TABLE OF CONTENTS.....	ix
LIST OF TABLES.....	xii
LIST OF FIGURES.....	xiii
LIST OF ABBREVIATIONS.....	xxiii
CHAPTER ONE Introduction	1
1.1 Motivation.....	1
1.1.1 Gold-biomolecule interface	1
1.1.2 Scanning Tunneling Microscope-based Break Junction (STMBJ).....	2
1.1.3 Overview	3
1.2 Charge transport through a single molecule junction	3
1.2.1 Gold point contact and Landauer-Büttiker formalism.....	3
1.2.2 Charge transport of a molecular junction.....	5
1.3 Chemistry of molecular junctions.....	6
1.3.1 The anatomy of a molecular junction	6
1.3.2 Linker chemistry	7
1.3.3 Au–N linkers.....	7
1.4 Noncovalent interactions in single molecule junction	9
1.4.1 π – π stacking interactions in single molecule junction	9
1.4.2 Hydrogen bonding interactions in single molecule junctions.....	10

1.5 Thesis Outline	12
CHAPTER TWO Experimental Methods and Data Analysis	14
2.1 Home-built single molecule tunneling break junction setup	14
2.2 Molecule deposition procedures	17
2.3 Data analysis and visualization	18
2.4 DFT and transmission calculation	22
2.5 Flicker noise analysis	24
CHAPTER THREE pH-Activated Single Molecule Conductance and Binding	
Mechanism of Imidazole on Gold	28
3.1 Preface	28
3.2 Introduction	28
3.3 Results and Discussion	29
3.4 Conclusion	42
CHAPTER FOUR Cooperative Self-Assembly of Dimer Junctions Driven by π -Stacking	
Leads to Conductance Enhancement	43
4.1 Preface	43
4.2 Introduction	43
4.3 Additional theoretical calculation methods	45
4.3.1 Calculations of junction geometry and transmission properties	45
4.3.2 Binding energy at the junction	46
4.3.3 Gas-phase intermolecular energy calculation	46
4.4 Results and Discussion	47

4.5 Conclusion	64
CHAPTER FIVE Atomically Precise Binding Conformations of Adenine and Its Variants on Gold Using Single Molecule Conductance Signatures	66
5.1 Preface	66
5.2 Introduction.....	66
5.3 Additional calculation methods and polarizable continuum model.....	70
5.4 Results and Discussion	74
5.5 Conclusion	93
CHAPTER SIX Single Molecule Conductance Signature of Intramolecular Hydrogen Bonding in a Histamine Bound on Gold.....	95
6.1 Preface	95
6.2 Introduction.....	95
6.3 Results and Discussion	98
6.4 Conclusion	109
BIBLIOGRAPHY.....	110
CURRICULUM VITAE.....	132

LIST OF TABLES

Table 3-1. The pK_a values and dipole moments of the solvents used in this study.	32
Table 4-1. List of measured conductance histogram peak values and their ratios for six molecules studied. Each entry in Table 4-1 is an average of at least 4 experiments conducted on different days with a minimum of 5000 traces collected per experiment. The uncertainty, as measured by standard error, is less than 1%.	51
Table 4-3. Calculated intermolecular energies for all gas-phase dimers in the parallel (P) and antiparallel (AP) configurations; intermolecular energy ratios of substituted BI/Im dimer over BI/Im dimers.....	55
Table 4-4: Calculated conductance of BI and Im molecular junctions. For the dimers, conductance values of each of the individual molecules are given in parentheses. .	60
Table 5-1. Binding energies between Ade and the blunt Au ₂₀ pyramid in aqueous environment and in vacuum as obtained from DFT calculations.	74
Table 5-2. The most probable conductance values of all molecules as obtained by fitting the linear conductance histogram with Gaussian fits. The standard errors of the Gaussian fitted values for all molecules are less than 1%.	76
Table 5-3. Decomposition of the binding energies between Ade and the blunt and sharp Au ₂₀ pyramid.....	87

LIST OF FIGURES

- Figure 1-1. A. A representative STMBJ measurement of conductance versus electrode displacement showcasing the experimentally observed conductance steps at integer multiples of G_0 .^{34,35} The final drop in current signifies the rupture of the gold contact and the formation of the inter-electrode gap. B. An illustration of the chemical potential landscape of a molecular junction at zero bias. The transmission function, $T(\epsilon)$, plotted against energy, is represented by the red and blue Lorentzian curves, illustrating a typical transmission function. $T(\epsilon)$ can be significantly influenced by the coupling strength (Γ) between the electrode and molecule and the energy offset ΔE between the Fermi level (E_f) of the gold electrodes and the conducting orbital. A single level model is used to simplify the molecular orbitals to just the Highest Occupied Molecular Orbital (HOMO) and Lowest Unoccupied Molecular Orbital (LUMO)... 4
- Figure 1-2. Schematic representation of a typical molecular junction using 1,4-diaminobenzene. This example junction consists of two gold metal electrodes, two amine linker groups, and a benzene molecular backbone that allows current flow through. 6
- Figure 1-3. Chemical structure of adenine and histamine. Potential binding sites, such as the exocyclic amino group and imine moieties, are highlighted with red circles. 8
- Figure 1-4. A. Illustration of the staggered π - π stacking configuration of a pair of OPE-monothiol molecules, where the aromatic rings are shifted by a ring length. This configuration allows for effective overlap of the π orbitals, facilitating charge transport. (Reproduced from Wu et al., Nature Nanotechnology, 3(9), 569-574.)... 10

Figure 1-5. Illustration of the adenine-thymine base pair in DNA, showcasing the formation of two H-bonds.	11
Figure 2-1. A. Image of the custom-built STMBJ setup used in the Kamenetska lab. B. Schematic representation of the circuit diagram of the instrument.	15
Figure 2-2. Atomic Force Microscope magnetic stainless steel (alloy 430) disc in three processing stages: as purchased (left), after polishing (middle), and following gold evaporation (right).	16
Figure 2-3: Conductance histograms of control measurements using solvents only.	18
Figure 2-4. A. Single trace samples of gold-gold contact. B. Histogram of clean gold only, linearly binned and displayed on a logarithmic scale for clarity. C. Histogram with data logarithmically binned and displayed on a linear scale.	19
Figure 2-5. A. Sample conductance traces of 1,4-diaminobutane (C_4), offset for clarity. B. One-dimensional histogram of C_4 , with data logarithmically binned. C. Two-dimensional histogram of C_4 as a function of conductance (y-axis) and displacement (x-axis), with the histogram counts represented on the z-axis and by the color bar. Inset: Chemical structure of C_4	20
Figure 2-6. This example figure illustrates the total interaction energy landscape of histamine, with abrupt energy changes indicating conformation alterations during the push/pull process. Different color traces represent multiple iterations of the procedure.	23
Figure 2-7. A. Sample conductance (red) and displacement (blue) traces for a single flicker noise experiment, with G_{avg} indicating the average conductance during the hold period	

(blue bracket). B. Sample Noise Power Spectral Densities (PSDs) can be obtained by transforming the hold period conductance from the time domain to the frequency domain using the discrete Fourier transform (dFT). The yellow shaded region represents the noise power integrated from 100 Hz to 1000 Hz. C. Averaged conductance noise PSDs of 1-methylimidazole (1MeIm) in blue and 1,6-hexanediamine (C_6) in red; the black dashed line indicates the $f^{-1.4}$ dependence. 25

Figure 2-8. A. Correlation of noise power/ G^N with the average junction conductance (G_{avg}) for 1MeIm. The dashed grey line indicates where the correlation equals zero, corresponding to a scaling exponent N of 1.7. B. Two-dimensional histogram of noise power/ G_{avg} against G_{avg} for C_6 , black lines showing the 2D Gaussian fits. Inset: Chemical structure of C_6 . C. Two-dimensional histogram of noise power/ G_{avg} against G_{avg} for 1MeIm, black lines showing the two-dimensional Gaussian fits. Inset: Chemical structure of 1MeIm. 27

Figure 3-1. A) Sample conductance traces measured in the presence of imidazole dip coated on the gold sample from water. Inset: Chemical structure of imidazole with atomic positions numbered B) Linear binned histograms of Im deposited out of water, showing the high-G region (bin size = 10^{-4}) and the low-G region (inset; bin size = 10^{-6}). The dashed lines represent four and two Gaussian fits to the high-G and low-G regions, respectively. The most likely conductance values corresponding to the centers of these distributions are found to be $1.9 \times 10^{-2} G_0$, $4.0 \times 10^{-2} G_0$, $6.2 \times 10^{-2} G_0$, and $8.1 \times 10^{-2} G_0$; be $1.2 \times 10^{-4} G_0$ and $2.4 \times 10^{-4} G_0$ for low-G. C) 1D log-binned conductance histograms constructed from at least 4000 traces of imidazole dip coated

onto gold from various solvents. D) Conductance histograms of Im deposited out of aqueous solutions of varying pH constructed without data selection from at least 5000 traces. E) The proposed mechanism for Im binding Au in basic conditions through the 3N lone pair. F) Proposed mechanism for the Au-catalyzed deprotonation of imidazole in basic conditions and for the formation of Au-Im⁻-Au junctions. 30

Figure 3-2. Conductance histograms of imidazole dissolved in acidic aqueous solvents and polar aprotic organic solvents were obtained from a minimum of 4000 traces. 33

Figure 3-3: Conductance histograms for 2-Methylimidazole and 4-Methylimidazole, constructed from 4000 traces. Measurements were taken at pH levels both above (solid lines) and below (dashed lines) the *pKa* values of the molecules. 35

Figure 3-4. A) Conductance histograms of Im, 4-MeIm, and 2-MeIm in pH 9 and 1-MeIm in pH 12 were constructed from at least 5000 traces. Inset: structures of the molecules. B) Conductance histograms of Im constructed from at least 9000 traces each, measured on samples prepared with aqueous solutions at pH 12 containing differing concentrations of imidazole. 37

Figure 3-5: A) 2D conductance-displacement histogram constructed from 10000 traces of imidazole dip coated from water. B-E) The calculated structure and binding energy of various Au-Im configurations: (B) three Im⁻ ions bound in parallel on blunt Au₁₉ pyramids (hydrogen atoms omitted for clarity); (C) the Au-Im⁻-Au complex; (D) the Au-Im⁻-Au chain; (E) the Im-Au complex. The labels on atoms around the Au-N bonds in (D) and (E) indicate the total charge on the atom. 38

Figure 4-1. Geometry of the gas-phase BI dimer in the a) parallel and b) antiparallel configuration.....	47
Figure 4-2. a) Sample conductance traces showcasing a clean gold (Au) junction (depicted in yellow) and an Au-BI-Au junction (shown in black). b) A schematic representation of a molecular junction featuring BI and two gold electrodes. A bias is applied across the junction, and the resulting current is measured.....	48
Figure 4-3. a) 2D histogram of benzimidazole; inset: chemical structure of benzimidazole. b) 2D histogram of imidazole; inset: chemical structure of imidazole. c) 1D histogram of benzimidazole (blue) and imidazole (red). The green dashed box contains the conductance region of interest in this work.	49
Figure 4-4. a) Unit cell used in the simulations to probe the angular dependence of the total energy in Im and BI junctions with two molecules. B) Total energy (relative to the minimum value of each species) as a function of the relative angle between both molecules, calculated for two Im (red) and two BI (blue) molecules adsorbed on the same tip structures. The inset illustrates the relative angle θ from a top view of the molecules and tip structures.....	53
Figure 4-5: Energy scan of BI and Im dimers, as a function of θ , with and without vdW contributions.	54
Figure 4-6. a) Transmission spectra of individual Im and BI molecular junctions. Real-space representation of the most conducting transmission eigenchannel at the center of the Brillouin zone for b) BI at -0.4 eV, c) BI at the Fermi energy, and d) Im at the Fermi energy.	56

Figure 4-7. a) Transmission spectra of Im and BI dimers. Real-space representation of the most conducting transmission eigenchannel for b) BI dimers at the Fermi energy and c) Im dimers at the Fermi energy.....	57
Figure 4-8. Torsional angle α between tip and molecule, and calculated conductance scans of BI and Im monomers as a function of α	60
Figure 4-9. (a) Conductance histograms of 2-methylimidazole (2MeIm) and 2-phenylimidazole (2PhIm). Inset: Chemical structures of 2MeIm and 2PhIm. b) Conductance histograms of 2-phenylbenzimidazole (2PhBI) and 2-methylbenzimidazole (2MeBI). Inset: Chemical structures of 2PhBI and 2MeBI. Both conductance histograms are cut off at $10^{-3} G_0$ to focus on the HG region only.	61
Figure 4-10. Full conductance histograms of a) 2-methylimidazole (2MeIm) and 2-phenylimidazole (2PhIm); b) 2-phenylbenzimidazole (2PhBI) and 2-methylbenzimidazole (2MeBI). All four molecules show low conductance features at $10^{-4} G_0$	62
Figure 4-11: Energy profile of 2PhIm, calculated as in Figure 4-4, as a function of the relative angle between both Im units. 2Im and 2BI are reproduced from Figure 4-4 for comparison.....	64
Figure 5-1. (A) Chemical structures of the two dominant adenine (Ade) tautomers with the non-H atoms numbered. (B) A cartoon of junction evolution while the two electrodes are pulled apart in the presence of Ade. (C) Sample conductance traces of clean gold (Au) junction (yellow) and Au-Ade-Au junction (black)..	68

Figure 5-2. DFT-calculated frontier molecular orbitals and their corresponding energies for the isolated N7H, N9H, and anionic forms of the Ade molecule in the gas phase... 69

Figure 5-3: Conductance histograms of Ade measured at different pH levels: pH 2, pH 7, and pH 12..... 71

Figure 5-4. (A) Chemical structure of benzimidazole (BIm), purine (Pu), 4-azabenzimidazole (CN3) and 5-azabenzimidazole (CN1) with atomic positions numbered. (B) Conductance histograms of Ade, BIm, and Pu were binned from at least 6000 traces without any data selection. All molecules were measured using the dip-coating method from water as detailed in the SI. We identify at least two distinct conductance features labeled LG (yellow shading) and HG (green and red shading) in all or a subset of the molecules. (C) Conductance histograms of CN3 and CN1 compiled from at least 6000 traces without any data selection measured using the dip-coating method in pH 12. (D) Two-dimensional conductance-displacement histogram constructed from 7000 traces of Ade dip-coated from water with no data selection. 75

Figure 5-5. Linear binned (bin size = 10^{-4}) histograms of (A)Pu (black), Ade (green), BIm (pink) , (B) CN3 (blue), and CN1 (red). Inset: Ade linear histogram (green) with two Gaussian fits (black dashed line) representing the HG1 and LG peaks..... 77

Figure 5-6. Conductance histograms of (A) Pu and (B) BIm measured at pH 2 and pH7. 78

Figure 5-7. Conductance histograms of Ade and 6MePu. Inset: chemical structure of 6MePu..... 80

Figure 5-8. Definition of C-N-H-H dihedral angles and the exocyclic C-N bond lengths of (A) Ade and (B) 1,4 benzenediamine (BDA). 81

Figure 5-9. Optimized geometries for the binding of Ade on the blunt Au₂₀ pyramid at the (A) N1, (B) N3, (C) N7 and (D) N9 sites. Yellow, gray, blue and white represent the Au, C, N and H atoms, respectively. The dotted lines represent the interactions between the Au atoms and the closest N atoms on Ade. The total interaction energy $\Delta E_{INT}(s)$ is also included for each binding configuration. (E) Decomposition of $\Delta E_{INT}(s)$ into the frozen interaction energy ($\Delta E_{FRZ}(s)$), polarization energy ($\Delta E_{POL}(s)$) and charge transfer energy ($\Delta E_{CT}(s)$)..... 85

Figure 5-10. Optimized geometries for the binding of Ade on the sharp Au₂₀ pyramid at the (A) N1, (B) N3, (C) N7 and (D) N9 sites. Yellow, gray, blue and white represent the Au, C, N and H atoms, respectively. The dotted lines represent the interactions between the Au atoms and the closest N atoms in Ade. (E) Decomposition of the interaction energies between the Ade anion and the sharp Au₂₀ pyramid at different binding sites. For each binding site on Ade, the total interaction energy ($\Delta E_{INT}(s)$) is partitioned into the frozen interaction energy ($\Delta E_{FRZ}(s)$), polarization energy ($\Delta E_{POL}(s)$) and charge transfer energy ($\Delta E_{CT}(s)$)..... 86

Figure 5-11. Relaxed structures of proposed binding geometries of N3/N7/N9 (black), N7/N9(red), and N3/N7(green) to Au₁₈ pyramids and their corresponding transmission spectra. 90

Figure 5-12. (A) Chemical structure of N6-methyladenine (M6A) and 2'-deoxyadenosine (2'-dAdo) with the non-H atoms numbered. (B) Conductance histograms generated

from at least 6000 traces collected in the presence of M6A (blue), 2'-dAdo (red), Ade (green, dashed line) deposited in neutral aqueous conditions..... 92

Figure 6-1. A. Chemical structures of histamine (hist) and its tautomeric forms; in the π (left) and τ (right) forms, the proton is at the N1 and N3 position, respectively. B. Monocation form of hist mostly exists at pH between 6 and 9.75; the free base form of hist mostly exists above pH 9.75. C. The most probable structure of monocationic hist in the gas phase, as predicted by DFT calculations (FHIaims, light basis set). A positive charge is added to the overall system to account for positively charged ammonium group..... 97

Figure 6-2. Sample conductance traces for clean Au only (yellow) and in the presence of the hist molecule (black)..... 99

Figure 6-3. A. Conductance histograms of hist at pH 7 (yellow) and pH 12 (black). Conductance features of hist are labeled as A, B, and C, from highest to lowest conductance, respectively. B. Chemical structures of 4-Methylimidazole (4MeIm) in red, 3-Methylhistamine (3MeHist) in blue, and 1-Methylhistamine (1MeHist) in green. C. Conductance histograms of 4MeIm (red), 3MeHist (blue), and 1MeHist in pH 12 (green). Red and blue shaded regions represent conductance overlap of control molecules and hist. D. Two-dimensional histogram of hist at pH 12, with the features A, B, and C marked. All conductance histograms are constructed from at least 8000 traces without data selection. 100

Figure 6-4. A. Relaxed DFT-calculated junction geometries of a hist molecular junction with two Au18 electrodes pulling or pushing along the Z direction in 0.15 Å steps.

The Au-Au edge distance, highlighted using a pink arrow, represents the distance between the edges of two Au18 electrodes. Selected sample steps are from the FB9 structure to represent junction opening. B. The energy landscapes of the three identified stable geometries for hist in molecular junctions as a function of Au-Au electrode edge distance. The green numbering corresponds to the example steps graphically represented in Figure 6-4A. C. Transmission spectra of three local interaction energy maxima structures of free base hist, FB8 (yellow), FB9 (green), and FB10 (blue). Inset: Relaxed structures of FB8, FB9, and FB10. A top-down views of FB8 and FB9 are provided in Figure 6-5 to better visualize the differences between these two structures. 103

Figure 6-5: DFT calculated structures of A. FB8 and B. FB9, viewed from a different angle to illustrate the varying binding orientations of the ethylamine chain to the gold surface. The numbers on both figures represent the distances of the $N\alpha$ to $N3$ hydrogen bonds within each junction. 103

Figure 6-6. A comparative analysis of transmission spectra between a cleaved hist molecule conducting exclusively via a hydrogen bond and the models FB9 and FB8. Inset: the newly modified structure where the ethylamine chain is detached from the imidazole, and two new hydrogen atoms are attached to the structure to maintain structural integrity. 106

Figure 6-7. Two-dimensional histogram of normalized flicker noise power versus average conductance for A) hist feature B, B) hist feature C, and C) 3MeHist. The grey lines in each figure represent a two-dimensional Gaussian fit for each dataset. 108

LIST OF ABBREVIATIONS

0	Not Solute-solvent interaction
s	Solute-solvent interaction
$^{\circ}\text{C}$	Celsius
ΔE	Energy
1D	One dimension
1MeHist	1-Methylhistamine
1MeIm	1-Methylimidazole
2'-dAdo	2'-deoxyadenosine
2D	Two dimension
2MBI	2-Methylbenzimidazole
2MeIm	2-Methylimidazole
2PhBI	2-Phenylbenzimidazole
2PhIm	2-Phenylimidazole
3MeHist	3-Methylhistamine
4MeIm	4(5)-Methylimidazole
6MePu	6-Methylpurine
Å	Angstrom
Ade	Adenine
AITRANSS	Ab initio transport simulations
AP	Dimmer in antiparallel configuration
ATP	Adenosine triphosphate

Au.....	Gold
Au-N	Gold to nitrogen bond
B3LYP	Becke,3-parameter, Lee–Yang–Parr
BDA	1,4 benzenediamine
BI.....	Benzimidazole
BIm	Benzimidazole
C.....	Carbon
C ₄	1,4-Diaminobutane
C ₆	1,6-Hexanediamine
CH ₃	Methyl group
CN1	Control N1 molecule 5-Azabenzimidazole
CN3	Control N3 molecule 4-Azabenzimidazole
CT	Charge transfer energy
def2-SVP.....	Karlsruhe basis set, Split valence polarization
def2-SVPD	Karlsruhe basis set, Split valence polarization with diffuse function
def2-TZPVD ...	Karlsruhe basis set, Valence triple-zeta polarization with diffuse functions
def2-TZVP	Karlsruhe basis set, Valence triple-zeta polarization
DFT	Density Functional Theory
dFT	Discrete Fourier Transform
DISP	Dispersion
DMF.....	N, N-dimethylformamide
DNA.....	Deoxyribonucleic acid

$E_{Ade,opt}$	Energy of optimized adenine molecule
E_{Ade}	Energy of isolated Ade anion
E_{Au}	Total energy of Au electrode
EB	Ethyl benzoate
E_b	Binding energy
$E_{complex}$	Energy of total complex
E_{dimer}	Energy of dimer configuration
E_f	Fermi level
E_{gold}	Energy of gold electrode
E_{inter}	Intermolecular energy
$E_{junction}$	Total energy of the junction of the fully optimized configuration
ELEC	Permanent electrostatics
E_{mol}	Energy of the molecule
EPIC	Engineering Product Innovation Center
eV	Electron volt
f	Frequency
FB	Free base form of histamine
FHlaims	Fritz Haber Institute ab initio molecular simulations
FRZ	Frozen interaction energy
G	Conductance
G_0	Quantum of Conductance
G1	Monomer

G2.....	Dimer
G3.....	Trimer
G _{avg}	Average conductance
H.....	Hydrogen
HCl.....	Hydrochloric acid
HG.....	High-G region
HG1.....	High conductance peak 1 of Adenine
HG2.....	High conductance peak 2 of Adenine
Hist.....	Histamine
HOMO.....	Highest Occupied Molecular Orbital
Hz.....	Hertz
I.....	Current
Im.....	Imidazole
Im ⁻	Imidazolate
INT.....	Total interaction energy
IUPAC.....	International Union of Pure and Applied Chemistry
kHz.....	Kilohertz
KΩ.....	Kiloohm
LG.....	Low-G region
LUMO.....	Lowest Unoccupied Molecular Orbital
M.....	Molar
M6A.....	N ₆ -methyladenine

mL.....	Milliliter
mm	Millimeter
mM	Millimolar
mV.....	Millivolt
MΩ.....	Megaohm
N	Nitrogen
NaOH	Sodium hydroxide
NH ₂	Amino group
nm	Nanometer
NMR	Nuclear Magnetic Resonance spectroscopy
OPE.....	Oligo-phenylene-ethynylene
opt	Optimization
P	Dimmer in parallel configuration
PAULI.....	Paul repulsion
PBE	Perdew–Burke–Ernzerhof
PBE0	Perdew–Burke–Ernzerhof and Hartree–Fock in a set 3:1 ratio
PC.....	Propylene carbonate
PCM	Polarizable continuum model
pH.....	Potential of hydrogen
pKa.....	Acid dissociation constant
POL.....	Polarization energy
PSD	Power Spectra Density

Pu	Purine
SERS	Surface Enhanced Raman Scattering Spectroscopy
SIESTA.....	Spanish Initiative for Electronic Simulations with Thousands of Atoms
SOL.....	Solvation
STMBJ	Scanning Tunneling Microscope-based Break Junction
T(ϵ).....	Transmission function
TEA.....	Triethylamine
TERS.....	Tip Enhanced Raman Scattering Spectroscopy
T	Transmission
transSIESTA	Spanish Initiative for Electronic Simulations with Thousands of Atoms with non-equilibrium electronic transport transmission calculation package
V.....	Voltage
XRD	X-ray Diffraction analysis
Γ	Gamma factor
ΔE	Energetic alignment
ϵ	Energy
θ	Relative angle between two molecules
μL	Microliter

CHAPTER ONE Introduction

1.1 Motivation

1.1.1 Gold-biomolecule interface

Understanding the fundamental interactions at the gold-biomolecule interface is essential for numerous applications, particularly in biosensing, bioelectronics, and nanotechnologies.¹ The gold-biomolecule interaction can dictate the behavior and performance of devices in these fields, impacting aspects ranging from the sensitivity of biosensors to the dependability of bioelectronic devices.²⁻⁴ Moreover, it can aid in the development of innovative nanostructures and nanodevices with custom properties.⁵⁻⁸ Ultimately, a deeper understanding of the gold-biomolecule interaction can lead to optimized device design and unlock new potential in these fields.

For example, there is interest in incorporating deoxyribonucleic acid (DNA) as an electronic component into circuits due to its relevant properties.^{9,10} These include self-assembly,¹¹ structural stability,¹² predictable base pairing,^{9,12} and the ability to carry and transport charge.¹³⁻¹⁵ However, characterizing the conductance of DNA is challenging due to its complex composition and the multitude of interactions among its components. Direct electrical measurements have yielded conflicting results, adding to the complexity of understanding the nature of the conductance.^{13,16-19} To address this question, it is essential to understand the interactions between the individual components of DNA and gold. Furthermore, it is crucial to explore how the noncovalent interactions within DNA tertiary structure, such as π stacking and hydrogen bonding, contribute to its conductive properties.

1.1.2 Scanning Tunneling Microscope-based Break Junction (STMBJ)

The Scanning Tunneling Microscope-based Break Junction (STMBJ) is a powerful technique that enables the probing of the electronic conductance of organic molecules at the single-molecule level.^{20,21} This method involves repeatedly bringing two metal electrodes into contact and separating them with sub-angstrom precision in the presence of the target molecules. A sub-nanometer gap forms upon breaking the metal contact, allowing a single molecule to bind between the tip and the substrate. This binding event closes the electrical circuit, enabling the direct measurement of the electrical conductance of the molecule. This method provides detailed insights into the electronic properties of the target molecule and its chemical interactions with the gold surface, thereby offering a robust tool for studying metal-molecule interactions.^{22,23}

STMBJ conductance measurements can be used to examine the specific binding conformations of biomolecules on the gold surface at the atomic scale. For example, distinct binding configurations can result in different conductance signals;²⁴ these unique conductance signals can be employed to differentiate between various biomolecules or different states of the same biomolecule.^{25,26} Furthermore, single-molecule conductance signals can be utilized to gain insights into the interactions between biomolecules and metal surfaces under specific conditions. These conditions include the formation and rupture of molecular junctions,^{25,27} surface molecule rearrangements,²⁸ and the response of the molecular interface to external stimuli.^{26,29} Understanding the fundamental mechanisms of interactions is essential since they can significantly influence the functionality of biosensing and bioelectronic devices.

1.1.3 Overview

This chapter begins with an introduction to the Landauer-Büttiker formalism, which provides a theoretical framework for understanding charge transport through one-dimensional molecular wires. We then delve into the anatomy of single molecule junctions and the intricacies of Au-linker chemistry. Subsequently, we introduce various types of noncovalent interactions that can be observed in molecular junctions and highlight areas that were unclear, which we will be investigating in this thesis. Finally, this chapter concludes with an outline of the dissertation, setting the stage for an in-depth exploration of the capabilities of STMBJ in detecting and differentiating gold-biomolecule interactions at the single-molecule level. This research advances our understanding of molecular junctions and paves the way for innovative biosensing technologies.

1.2 Charge transport through a single molecule junction

1.2.1 Gold point contact and Landauer-Büttiker formalism

In bulk materials, current flow is modeled using diffusive transport mechanisms involving electron scattering, leading to finite conductance.³⁰ However, electron transport is no longer diffusive at the nanoscale but rather ballistic.³¹ The Landauer-Büttiker formula provides a theoretical framework that describes electron transport at the nanoscale.^{32,33} It relates the conductance G of the system to the transmission probability of electrons passing through it, as described as follows,

$$G = \frac{2e^2}{h} \sum_N T_N$$

where h is Planck's constant, and e is the elementary charge. The summation is over all available conductance channels and the transmission probability, and T_n describes transmissions through every available channel. For a one-atom-thick gold wire, only one conductance channel with a near-perfect transmission is available, so the transmission over T_n can be approximated to one. Thus, the conductance of a single gold atom contact is given by the equation as follows,

$$G_0 = \frac{2e^2}{h} \cong 77.5\mu S$$

which is the quantum of conductance (G_0).^{34,35} As the gold junction is stretched and the number of gold atoms in the contact decreases, the current drops in integer multiples of G_0 , shown in Figure 1-1. After the 1 G_0 step, a tunneling current can be observed, which no longer follows the stepwise conductance decreases.

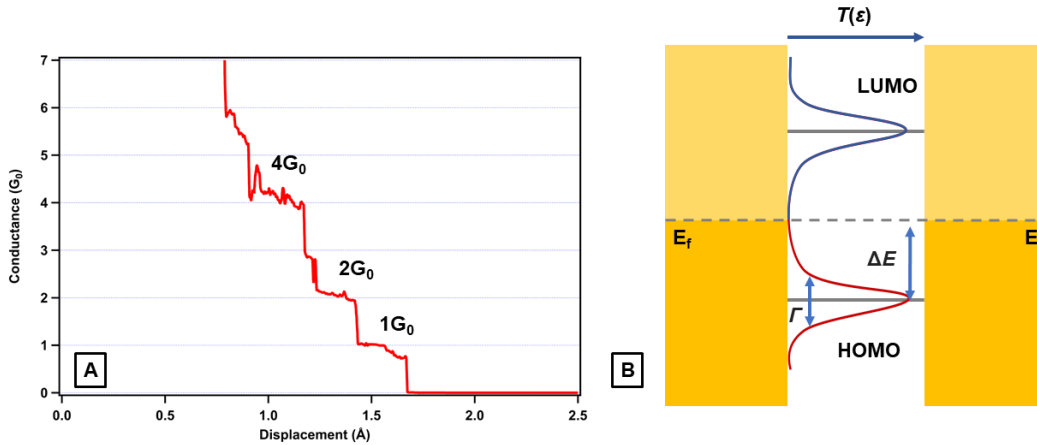


Figure 1-1. A. A representative STMBJ measurement of conductance versus electrode displacement showcasing the experimentally observed conductance steps at integer multiples of G_0 .^{34,35} The final drop in current signifies the rupture of the gold contact and the formation of the inter-electrode gap. B. An illustration of the chemical potential landscape of a molecular junction at zero bias. The transmission function, $T(\epsilon)$, plotted against energy, is represented by the red and blue Lorentzian curves, illustrating a typical transmission function. $T(\epsilon)$ can be significantly influenced by the coupling strength (Γ) between the

electrode and molecule and the energy offset ΔE between the Fermi level (E_f) of the gold electrodes and the conducting orbital. A single level model is used to simplify the molecular orbitals to just the Highest Occupied Molecular Orbital (HOMO) and Lowest Unoccupied Molecular Orbital (LUMO).

1.2.2 Charge transport of a molecular junction

The single-level model is often used to interpret experimental data and understand the transport features of a molecule within a junction.³⁶ This model simplifies the complex electronic structure of a molecule into two energy levels, typically the Highest Occupied Molecular Orbital (HOMO) and Lowest Unoccupied Molecular Orbital (LUMO). A chemical potential diagram, as depicted in Figure 1-1B, visually represents the energy levels of the system. This diagram includes the Fermi level (E_f) of the electrodes and two molecular energy levels, the HOMO and the LUMO. The transmission function, $T(\epsilon)$, represents the probability of an electron with energy ϵ to transmit through the molecule.³⁷ When interpreting transmission spectra such as the one shown in Figure 1-1B, there are several key parameters to pay attention to. First, the transmission at E_f is crucial as it determines the experimentally-observed low-bias conductance in the system. Secondly, this transmission function is significantly influenced by the hybridization overlap of a single molecular orbital with the continuous band of energy levels on the metal electrode, represented by the gamma factor, Γ . Lastly, factors such as the energetic alignment (ΔE) of the HOMO and LUMO relative to the metal E_f also play significant roles in determining transport properties.²²

Additionally, intrinsic molecular characteristics, including the nature of the molecular orbitals, the molecule–metal bond character, and the charged interactions at the metal–molecule interface, all contribute to these parameters.^{22,38} For example, orbitals with

electron density on the metal-binding anchor groups typically result in a broadened transmission resonance. This phenomenon reflects the better coupling of the molecule to the electrodes and the higher transmission probability at the Fermi energy and higher conductance. In contrast, orbitals localizing electron density on the molecular backbone exhibit more narrow resonances and poorer coupling and conductance.

1.3 Chemistry of molecular junctions

1.3.1 The anatomy of a molecular junction

Figure 1-2 illustrates a typical molecular junction consisting of metal electrodes (Au), linker groups (NH_2), and a molecular backbone (benzene). The linker groups serve as anchors, enabling the molecule to bridge between the gold electrodes and close the circuit, allowing charge transport across the backbone from one end of the molecule to the other. The choice of linker groups and substituents attached to the molecule can influence the electronic structure of the molecule and, consequently, the conductance of the junction.^{39,40} Substituents can modify steric hindrance or alter the electron donating/withdrawing effects of the molecule.^{41,42}

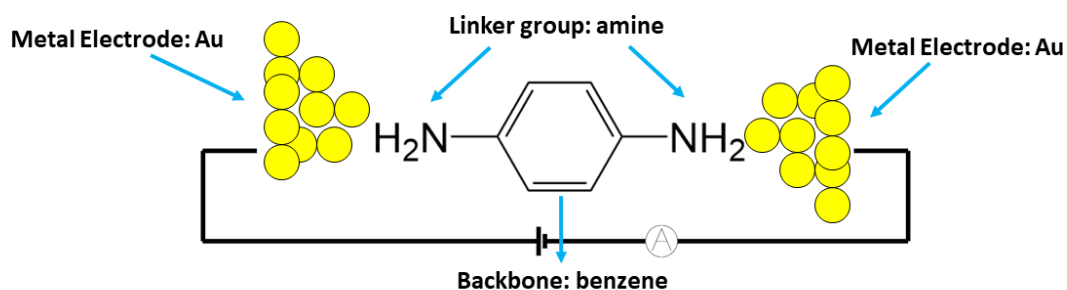


Figure 1-2. Schematic representation of a typical molecular junction using 1,4-diaminobenzene. This example junction consists of two gold metal electrodes, two amine linker groups, and a benzene molecular backbone that allows current flow through.

1.3.2 Linker chemistry

Linker groups play an important role in single-molecule junctions as they can significantly influence the binding configurations of the molecule. These groups typically bind to electrodes through either donor-acceptor bonds or covalent bonds. Covalent bond linkers, such as thiols, can form strong covalent bonds and facilitate strong electronic coupling between the molecule and the gold surface.²⁸ On the other hand, donor-acceptor linkers, such as the amine group, exhibit high selectivity with a preference for undercoordinated Au atoms while having weaker binding energy than covalent bonds.⁴³ This selectivity is advantageous as it narrows the conductance distribution by limiting the variability in the metal-linker contact geometry, leading to more consistent and predictable conductance measurements.⁴⁴

1.3.3 Au–N linkers

Many biomolecules contain amine or imine moieties, which can facilitate the direct binding of biomolecules in molecular junctions without further modification. In single-molecule junctions, electron lone pairs on nitrogen-containing functional groups form Au–N donor-acceptor bonds, which are highly selective and robust, providing a stable connection between the molecule and the electrode.^{22,43,45} Nitrogen-containing heterocyclic rings, such as imine and amine functional groups, are commonly found in many biomolecules. As Figure 1-3 illustrates, both adenine (one of the nucleobases) and histamine (a biogenic amine) contain these moieties. These characteristic positions biomolecule as ideal candidates for investigation in molecular junctions, thereby expanding the scope of single-molecule electronics.

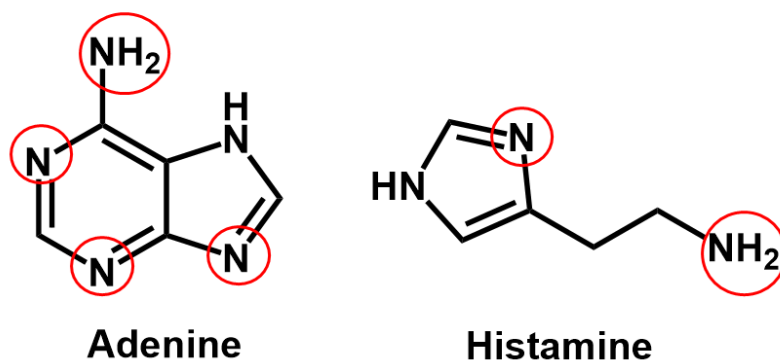


Figure 1-3. Chemical structure of adenine and histamine. Potential binding sites, such as the exocyclic amino group and imine moieties, are highlighted with red circles.

The primary amine linker group, consisting of a nitrogen atom bonded to one alkyl or aryl group and two H atoms, is a popular choice for single-molecule conductance measurements. Specifically, the primary amine linker prefers binding to under-coordinated gold atoms, leading to a consistent conductance signature.^{43,44} This consistency is reflected in the distinct sharp peak in conductance histograms constructed from thousands of conductance traces, providing clear evidence of the interaction of the molecule with the gold surface.

On the other hand, pyridine, an aromatic compound featuring an sp^2 -hybridized nitrogen atom (imine) within a six-membered ring, can also serve as an effective linker group in molecular junctions. The lone pair of electrons on the nitrogen atom resides in the σ plane of the molecule, distinctly orthogonal to the π system of the six-membered ring. Despite this orthogonality, the π system of pyridine can still interact with gold electrodes if the molecule is tilted, which results in a conductance signature that decreases during the elongation of the junction as the molecule changes orientation.^{24,45} Notably, the binding

energy of pyridine (1-1.3 eV per bond)²⁴ to gold is stronger than that of an amine linker (0.7–1.0eV per bond),⁴⁰ making it a robust choice for molecular junction studies.

1.4 Noncovalent interactions in single molecule junction

1.4.1 π - π stacking interactions in single molecule junction

In biological systems, π - π stacking is observed between DNA base pairs. Many researchers propose that the aromatic base pair stacking within the helices can facilitate charge transfer.^{13–15} Drawing inspiration from the unique structure of DNA, researchers are exploring the potential of incorporating these π - π stacked structures to construct highly conductive molecular wires. The STMBJ method serves as an excellent tool for characterizing the conductance of these π -stacked molecules and for understanding charge transport across π -stacked systems.

The traditional approach involves synthesizing pre-designed molecules and introducing them into the junction with linker groups. For example, Schneebeli et al. designed and probed up to four π - π stacked paracyclophanes systems for electrical detection.⁴⁶ Later, Vazquez et al. investigated the conductance superposition law in single-molecule junctions using a similar paracyclophane system and observed a significant increase in conductance due to constructive quantum interference.⁴⁷

However, Wu et al. pioneered the self-assembled approach by probing the conductance through conjugated monothiol-linked oligo-phenylene-ethynylene (OPE) systems.⁴⁸ They found that the conductance was an order of magnitude lower than that of dithiol-linked OPE molecules. Interestingly, this lower conductance was attributed to the formation of a self-assembled π -stacked structure in the junction by two OPE molecules,

as shown in Figure 1-4. Overall, this structure allows charge flow through the spatial overlap of the π orbitals between the two OPE molecules, effectively acting as a conductance bridge. Following this initial investigation, researchers have made efforts to manipulate these self-assembled π - π couplings in OPE systems. Researchers have explored various strategies, including substitution and spatial effects,^{49,50} quantum interference,⁵¹ and environmental controls,⁵² to influence the conductance properties of OPE systems. These findings pave the way for further exploration in molecular electronics and the search for alternative molecules capable of self-produced amplified conductance signals.

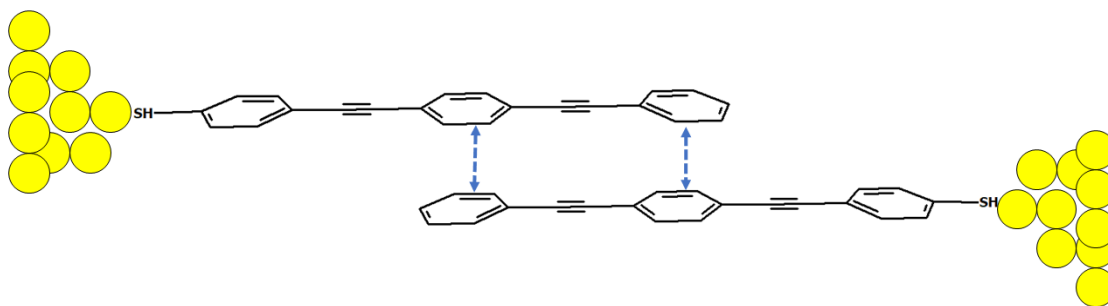


Figure 1-4. A. Illustration of the staggered π - π stacking configuration of a pair of OPE-monothiol molecules, where the aromatic rings are shifted by a ring length. This configuration allows for effective overlap of the π orbitals, facilitating charge transport. (Reproduced from Wu et al., *Nature Nanotechnology*, 3(9), 569-574.)

1.4.2 Hydrogen bonding interactions in single molecule junctions

Hydrogen bonding (H-bonding) plays a significant role in the structure, function, and dynamics of various biological systems. The H-bonds between nucleobases, depicted as dashed lines in Figure 1-5, play an important role in maintaining the double helix structure of DNA and contribute to the stability of the molecule.⁵³ Several research avenues have been identified for utilizing H-bonding in the context of organic and molecular

electronics.⁵⁴⁻⁶² These include exploring the role of H-bonding in transport through biological materials like DNA and studying the supramolecular H-bond-mediated self-assembly of conducting moieties.^{58,61,62}

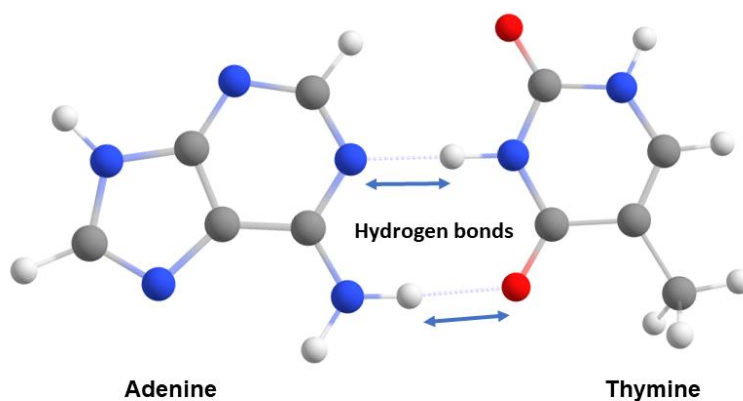


Figure 1-5. Illustration of the adenine-thymine base pair in DNA, showcasing the formation of two H-bonds.

The importance of H-bond-mediated charge transport in chemical and biological systems has led to a wealth of experimental and theoretical investigations to understand its underlying mechanisms. Supramolecular junctions involving multiple intermolecular H-bonds have been extensively studied using the STMBJ method.^{54-60,63,64} These studies have revealed that various factors can influence the conductance of intermolecular H-bond. These include the type of electrodes used in the experiments, the solvent used, and potential quantum interference effects that could decrease or increase the conductance of H-bond-containing complexes.^{54,58} The situation becomes more complex when considering multiple intermolecular H-bonds in a single molecular junction.^{57,62,63,65} Given these highly variable and debatable results, further investigations and theoretical explanations are needed to understand the conductance properties of H-bond systems.

1.5 Thesis Outline

This thesis investigates and differentiates specific interactions occurring at the gold-biomolecule interface using the STMBJ technique. The objective is to demonstrate how single molecule conductance signals can be utilized to identify and determine Au-biomolecule interactions at the atomic level. Furthermore, we also investigate different types of noncovalent interactions in molecular junctions by analyzing their single-molecule conductance signals.

Chapter 2 provides a detailed description of the methodology used in this thesis. It includes an overview of our custom-built STMBJ setup, sample preparation, experimental setup, data processing, statistical analysis methods, theoretical calculation methods, and flicker noise analysis procedures.

Chapter 3 delves into the pH-activated binding mechanism of imidazole in a single molecule junction. This study reveals that imidazole can bridge gold electrodes with a high probability of multiple molecules bound in parallel. Imidazole can also bind in series, with a gold atom connecting two imidazole molecules, forming in-situ molecule-metal-molecule chains.

Building on the findings from Chapter 3, Chapter 4 explores the cooperative binding of benzimidazole in single molecule junctions. This study uncovers that the benzimidazole dimer exhibits higher conductance than imidazole dimers. We utilize Density Functional Theory (DFT) methods to investigate the origin of the conductance enhancement. Theory calculations reveal that parallel stacking of two benzimidazoles between electrodes is the most energetically favorable due to its large π system. Finally,

we demonstrate a new self-assembly approach that leverages intermolecular interactions to achieve molecular junctions with improved electronic properties.

Chapter 5 shows how STMBJ measurements can determine the binding configuration of adenine, one of the nucleobases, on gold. Different conductance signals are assigned to distinct binding configurations by comparing adenine conductance to structurally similar control molecules. Additionally, we demonstrate that single molecule conductance signals can differentiate adenine and its biological derivatives, 2'-deoxyadenosine, and 6-methyladenine, laying the foundation for biosensing using single molecule conductance.

Chapter 6 studies the pH-activated hydrogen bonding conductance features of histamine. By systematically investigating the conductance of histamine and its derivatives, we can assign different conductance features to specific binding sites. DFT-transport models are used to identify the specific alkane configurations in molecular junctions. Finally, flicker noise methods are employed to determine and assign one of the conductance features in which current passes through the intramolecular hydrogen bond of histamine.

CHAPTER TWO Experimental Methods and Data Analysis

2.1 Home-built single molecule tunneling break junction setup

A custom-built single molecule tunneling break junction (STMBJ) is utilized to gather all the data in this thesis to investigate the conductance of single molecule junctions.^{20,26,27} A picture of our setup is shown in Figure 2-1A. The sub-angstrom precision piezoelectric z -axis positioner, NANO-METZ, is sourced from Mad City Labs Inc. The sample rests on a magnetic holder mounted to the piezo, and the tip holder is positioned above using a magnetic attachment. The entire setup is housed inside an acoustically insulated box lined with noise-isolating foam. This box is suspended by spring cords designed to dampen mechanical vibrations from the ceiling.

A constant bias of 500mV or 100mV is applied to the sample stage for all experiments. The circuit diagram of the junction is illustrated in Figure 2-1B. The current passing through the molecular junction is measured and amplified by the Keithley 428 Programmable Current Amplifier at a gain of 6. The amplifier is bypassed to allow for smaller voltage increments and finer step sizes. The conductance (G) of the molecular junction is calculated by dividing the measured current (I) by the applied bias (V). The current measurement and piezo displacement data are collected using a Data Acquisition card (National Instrument PXIe-1071 4-Slot 3U PXI Express Chassis 24-bit) at a rate of 40 kHz. Unless otherwise specified, a $1M\Omega$ or $1K\Omega$ resistor is connected in series with the junction to prevent current saturation for all experiments shown in this thesis.

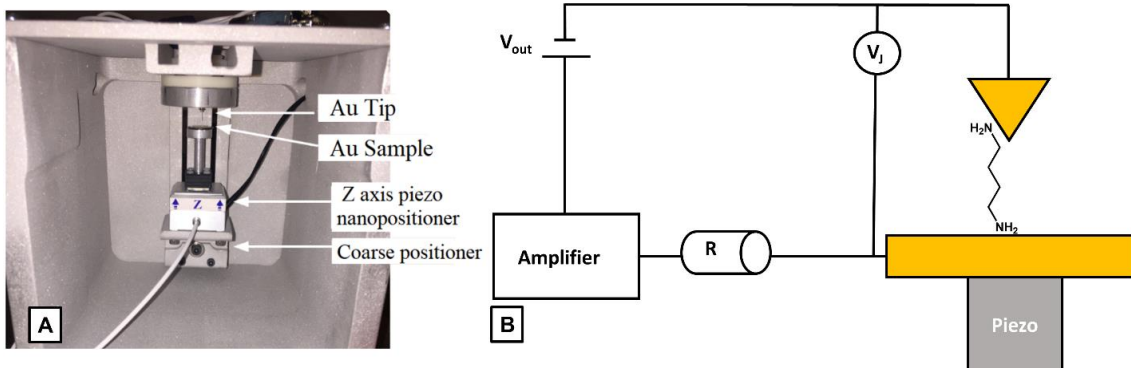


Figure 2-1. A. Image of the custom-built STMBJ setup used in the Kamenetska lab. B. Schematic representation of the circuit diagram of the instrument.

The tip gold electrode is prepared by mechanically cutting a gold wire (0.25mm diameter, 99.999%, Thermo Scientific Chemicals) to form a sharp tip and placing it in a magnetically held gold tip holder. The bottom gold electrode is prepared on Atomic Force Microscope metal specimen discs. These magnetic stainless steel Alloy 430 discs (12mm, Ted Pella) are used as the base substrates for the gold samples. To ensure a smooth surface for gold deposition, the discs are polished using a PlanarMet 300 Planar Grinder from Buehler Inc. at the Boston University Engineering Product Innovation Center (EPIC). We evaporate a layer of gold (99.985%, Thermo Scientific Chemicals) to a thickness of 100-150nm at a rate of $1 \text{ \AA}/\text{second}$ using a thermal evaporator (Edwards Auto 306 Turbo) in high vacuum conditions ($\sim 10^{-7}$ torr).

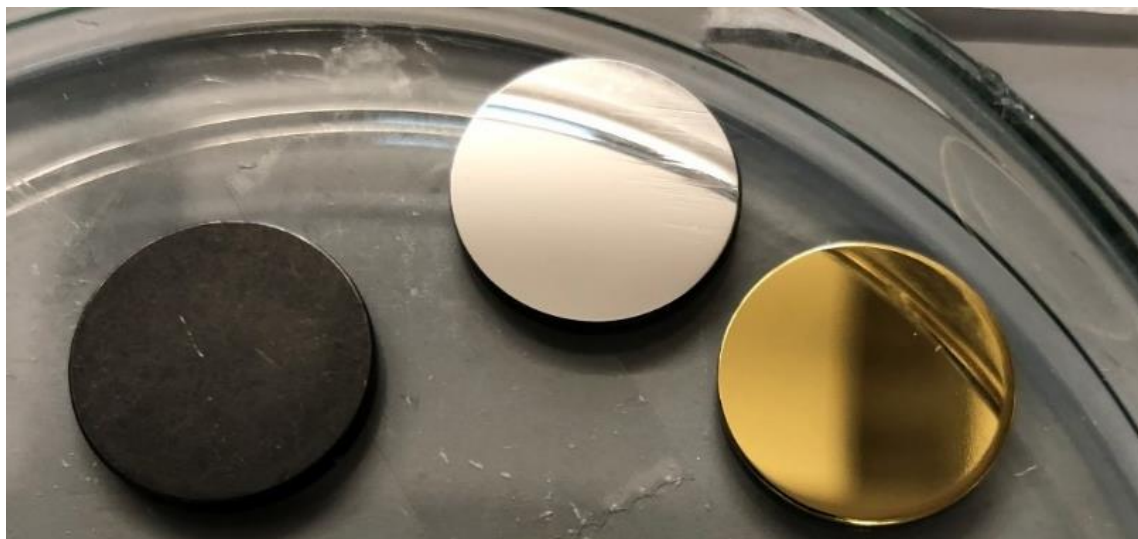


Figure 2-2. Atomic Force Microscope magnetic stainless steel (alloy 430) disc in three processing stages: as purchased (left), after polishing (middle), and following gold evaporation (right).

During the experiments, the piezoelectric nanopositioner repeatedly pushes the gold substrate into the gold tip to reach a conductance of $> 5 G_0$ (where $G_0=2e^2/h$), indicating the formation of gold-gold contact. The nanopositioner is then pulled 5 nm away to break the gold contact at a constant speed of 20nm/s. If the experiment is performed with target molecules deposited on a sample surface, the molecules can bridge and conduct through the junction. This process is repeated thousands of times using an automated protocol. Data are recorded and processed by a custom software procedure in Igor (Wavemetrics). For every experiment detailed in this thesis, we first ensure a clean surface by measuring clean gold for at least 1000 traces. Following this, we deposit the target molecule onto the same gold sample using an established deposition procedure described in the next section. We then measure thousands more traces on the target molecule.

2.2 Molecule deposition procedures

Most target molecules studied in this thesis are deposited out of aqueous solutions with a concentration of 1~5 mM. To adjust the pH of the aqueous solution, sodium hydroxide (NaOH) and hydrochloric acid (HCl) (Sigma Aldrich) are used. The target molecule is first dissolved in water; then, either 0.01M NaOH or 0.01M HCl can be added to achieve the desired pH. The pH of the adjusted solution is measured using Hydrion® Brilliant pH dipsticks from Sigma Aldrich.

To deposit molecules on the gold-coated substrate out of aqueous solutions or polar organic solvents, such as ethanol, triethylamine (TEA), propylene carbonate (PC), ethyl benzoate (EB), *N, N*-dimethylformamide (DMF), pyridine (all purchased from Sigma Aldrich), we utilize the dip coating method. This involves immersing the gold substrate in at least 2 mL of the prepared solution for at least 15 minutes. The sample is then carefully removed, ensuring minimal liquid remains on the gold surface to guarantee an even molecular coating. The solvent can be evaporated by slightly heating the sample inside the Digital Gravity Convection Oven from Quincy Lab to a temperature no greater than 55°C for aqueous solvents and no greater than 80°C for organic solvents. Figure 2-3 compares the histograms of water and clean gold, revealing additional peaks at 0.1 G_0 following water evaporation. Moreover, the evaporation of a pH 12 solution containing dissolved NaOH introduces another conductance feature above $10^{-2} G_0$. For molecules dissolved in non-polar solvents, 5 μ L of the solution containing the molecule of interest is directly deposited onto the gold samples, and the measurement is performed in a liquid environment.

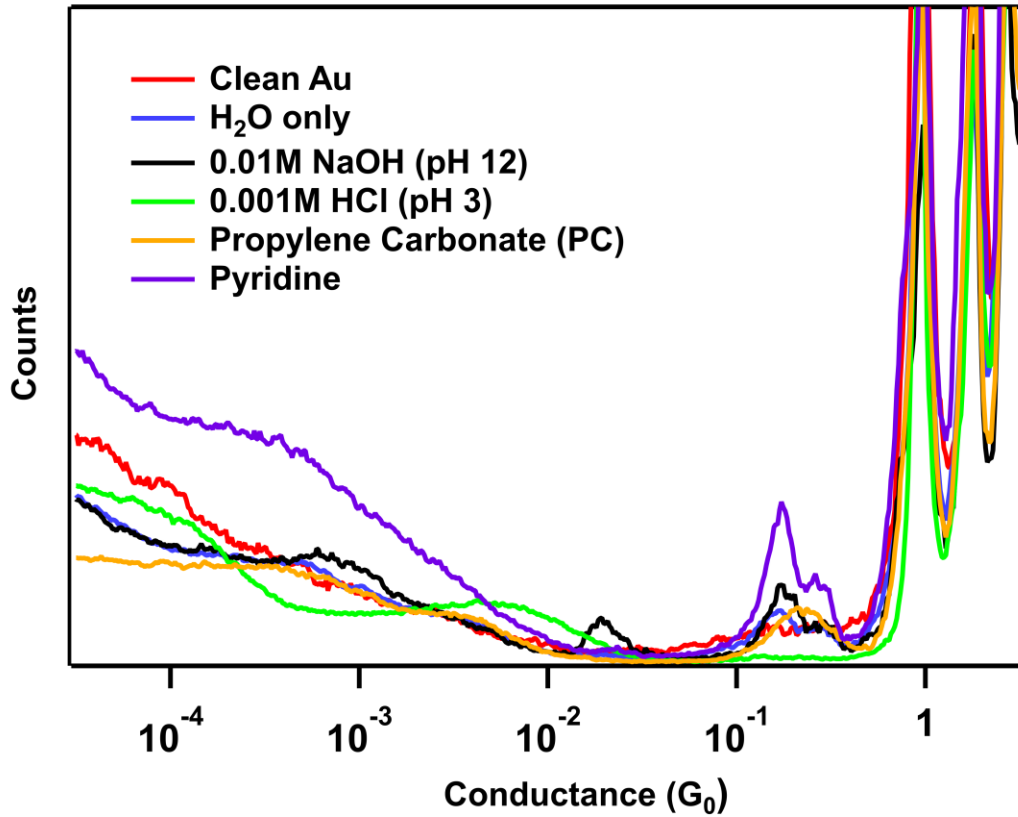


Figure 2-3: Conductance histograms of control measurements using solvents only.

2.3 Data analysis and visualization

We initiate our measurements by bringing two gold electrodes into contact and then retracting them while recording the conductance of the junction and piezo displacements. Sample traces, as depicted in Figure 2-4A, illustrate the conductance evolution during junction displacement. Thousands of traces are measured, displaying conductance plateaus at integer values, which indicate the thinning of the gold wire.^{35,66} Figure 2-4A, presented in a logarithmic scale, illustrates the evolution of conductance during displacement and sudden drops in conductance below 1 G_0 , suggesting a rupture of the gold-gold contact.³⁴

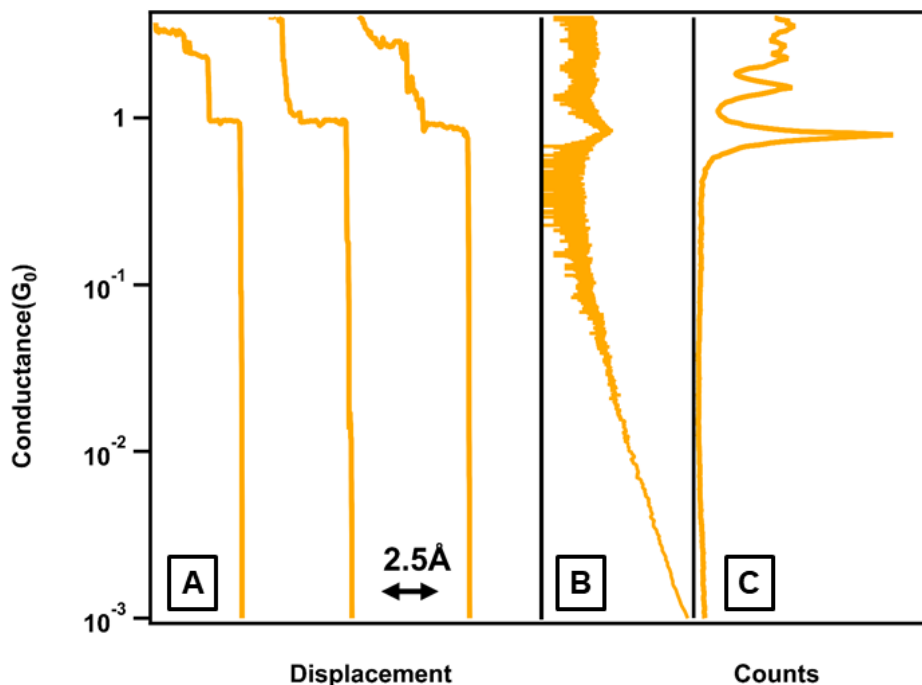


Figure 2-4. A. Single trace samples of gold-gold contact. B. Histogram of clean gold only, linearly binned and displayed on a logarithmic scale for clarity. C. Histogram with data logarithmically binned and displayed on a linear scale.

To determine the most probable conductance of the molecular junction, we generate a one-dimensional conductance histogram by binning conductance traces into a specific bin size and accumulating thousands of individual conductance traces. In the conductance histogram depicted in Figure 2-4B, sharp peaks are observed at $1 G_0$ and $2 G_0$. These peaks indicate the most probable formation of gold wires with one and two gold atoms in the cross-section. Since the molecules studied in this thesis are organic molecules and have higher resistance than a single gold contact, the linear-binned conductance histogram is plotted on a logarithmic scale (as shown in Figure 2-4B) to focus on the conductance regime below $1 G_0$. Another method used to visualize the data is constructing a log-bin

histogram by performing a logarithmic operation on the raw single trace data and then binning all the conductance traces, as shown in Figure 2-4C.

When these experiments are conducted in the presence of molecules on the surface, thousands of such traces are measured, as shown in Figure 2-5A, using 1,4-diaminobutane (C_4) as an example. These traces often display conductance plateaus, attributed to C_4 bridging and conducting through the electrodes. By binning all these traces into a one-dimensional histogram, we observe a reproducible molecular conductance signature appearing as a peak in the histogram at around $10^{-3} G_0$ values following a $1 G_0$ rupture shown in Figure 2-5B.^{21,39,67} This peak indicates the presence of molecules in the molecular junction and their most probable conductance at $\sim 10^{-3} G_0$.

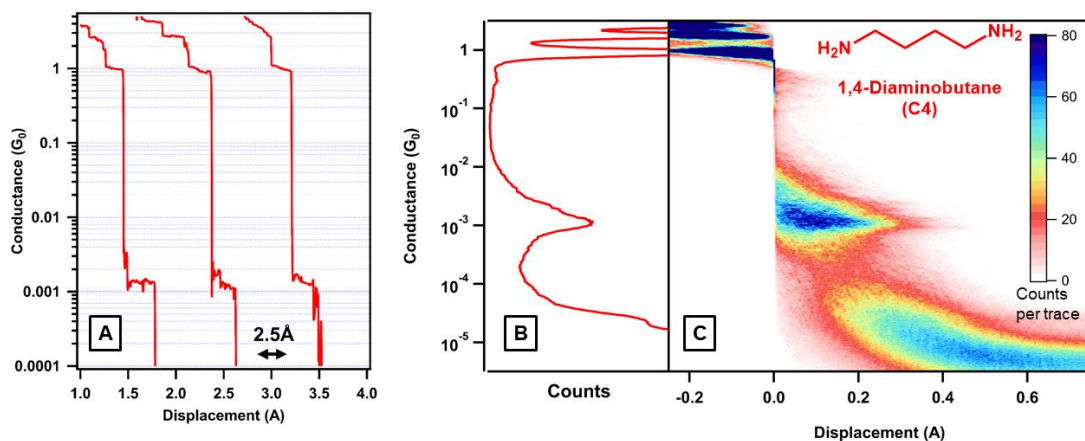


Figure 2-5. A. Sample conductance traces of 1,4-diaminobutane (C_4), offset for clarity. B. One-dimensional histogram of C_4 , with data logarithmically binned. C. Two-dimensional histogram of C_4 as a function of conductance (y-axis) and displacement (x-axis), with the histogram counts represented on the z-axis and by the color bar. Inset: Chemical structure of C_4 .

Since electrode displacement data are also recorded during the experiments, a 2-dimensional (2D) histogram can be constructed, as shown in Figure 2-5C. In this 2D histogram, the y and x-axes denote logarithmically binned conductance and linearly binned

displacement counts, respectively. The color scale corresponds to the number of counts in the corresponding bin. To better visualize the molecular plateau length, the zero-displacement point is defined as the breaking point of the gold-gold contact immediately after observing conductance at $1 G_0$. After the gold-gold rupture signaled at $1 G_0$, a molecular plateau appears around 0.3 nm at the positive region of the displacement scale, shown in Figure 2-5C. A 2D histogram is an excellent tool to characterize the persistence of C_4 molecular junctions.

To determine the most probable conductance, we perform a Gaussian fitting using the equation below,

$$f(x) = Ae^{-\frac{(x-\mu)^2}{2\sigma^2}}$$

where A is the amplitude, μ is the position of the center of the peak, and σ is the standard deviation, which is the width of the curve. By fitting the conductance peaks, we determine μ and σ , which signify the most probable and average conductance and the peak width, respectively. The conductance values in this thesis refer to the conductance peak values from these histograms. The width of the peak can vary due to multiple factors, such as different molecular configurations or changes in gold-molecule contact during junction elongation.²² Some molecules exhibit multiple conductance peaks. For these instances, a double, triple, or quadruple Gaussian, as shown in the equation below, can perform multi-peak fitting.²⁶

$$f(x) = A_1e^{-\frac{(x-\mu_1)^2}{2\sigma_1^2}} + A_2e^{-\frac{(x-\mu_2)^2}{2\sigma_2^2}} + A_3e^{-\frac{(x-\mu_3)^2}{2\sigma_3^2}}$$

2.4 DFT and transmission calculation

We use the Fritz Haber Institute ab initio molecular simulations (FHI-aims) package^{68–70} with the Perdew–Burke–Ernzerhof (PBE) density functional for exchange–correlation⁷¹ to compute the geometries of metal–molecule–metal junctions. Initially, we relax the molecule of interest, binding it to one side of the model Au₁₈ gold electrode and allowing it to relax again. Then we take the relaxed geometry and attach to the other gold electrode, aligning the backplane of the first gold electrode perpendicular to the z -axis.

In our custom procedure, one side of the electrode (all 18 gold atoms) shifts along the z -axis by 0.15 Å per step, with all atoms, except the molecule in the junction and the top two gold layers at the tip (4 gold atoms per electrode), held fixed. We relax the structure at each step until the atomic forces fall below 0.01 eV×Å⁻¹. We record the overall energy of the Au₁₈-molecule-Au₁₈ structure and calculate the total interaction energy. The y -axis in Figure 2-6 represents the total interaction energy of an example molecular junction, which is defined as follows,

$$E_{total\ interaction\ energy} = E_{molecule\ and\ electrodes} - (E_{gas\ phase\ molecule} + E_{gas\ phase\ electrode})$$

Then we can visualize the energy landscape as the total interaction energy during the push-pull manipulation of the geometry and locate the most probable structure for the target molecule.

Given that some alkane-containing molecules can adopt numerous geometries, we systematically search for the most stable binding geometries of the molecule to investigate the energy landscape of the alkane confirmations in the junction.⁶⁷ A sudden energy spike

or drop in the energy landscape plot signifies a transition to another alkane geometry, as shown in Figure 2-6. We can initiate a push or pull from the transition between two alkane structures to identify another energy minimum.⁷²

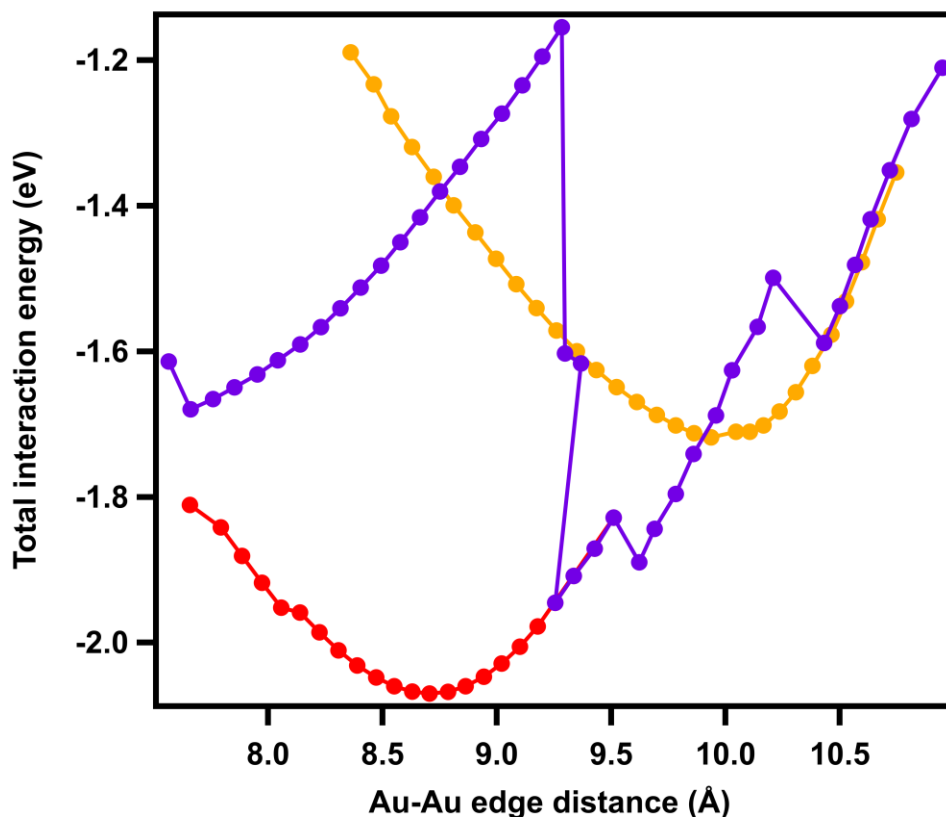


Figure 2-6. This example figure illustrates the total interaction energy landscape of histamine, with abrupt energy changes indicating conformation alterations during the push/pull process. Different color traces represent multiple iterations of the procedure.

Upon locating the structure corresponding to the local total interaction energy minima, we compute the Kohn–Sham states using an optimized all-electron numeric atom-centered tight basis set (akin to a double zeta plus polarization basis set) for the molecule and a loose basis set (similar to a double zeta basis set) for the gold atoms.⁷³ To calculate the energy-dependent electron transmissions across the relaxed junction geometries at zero bias, we utilize the non-equilibrium Green’s function method implemented in the

AITRANSS of the FHIaims package, while maintaining the same theoretical level for transmission calculations.^{68,70,74}

2.5 Flicker noise analysis

Molecular junctions primarily involve two fundamental types of interactions: through-bond and through-space.^{75,76} In through-bond coupling, the molecule is coupled to the electrodes via covalent or dative interactions, maintaining a relatively stable distance between the molecule and the electrodes.²² Consequently, electrons are mostly traveling along the bonds of the molecule, moving from one electrode to the other. On the other hand, through-space coupling involves the molecule being connected to the electrodes via noncovalent interactions, such as π interactions and hydrogen bonding.^{48,77} In this case, the interactions between the molecule and the electrodes are less stable, leading to significant conductance fluctuations. As a result, electrons primarily tunnel through the vacuum space between the molecule and the electrodes.

Adak et al. demonstrated that the noise intrinsic to single molecule junctions follows a power law relationship of $f^{-1.4}$, where f is the frequency, which is a characteristic of flicker noise.^{76,78} They established a method to distinguish between through-space and through-bond transport by analyzing the dependence of junction flicker noise on conductance.⁷⁶ To perform this analysis, we first need to confirm the presence of molecular signals within the junction. We start with our standard experimental protocol described in section 2-1. Using the piezoelectric nanopositioner, we use a modified procedure to incorporate a holding phase. After an extension of 1.5 nm, the pulling is stopped, and the junction is held fixed for 150 ms, as shown in Figure 2-7A. Following this step, the piezo

resumes its extension of an additional 3 nm to ensure the complete breaking of the molecular contact. This altered procedure is repeated across at least 10^4 traces, collecting conductance and displacement data.

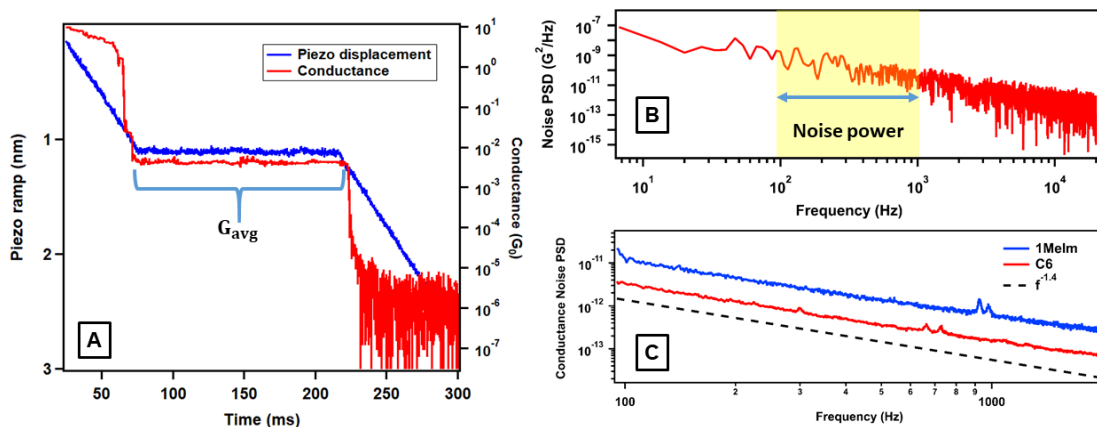


Figure 2-7. A. Sample conductance (red) and displacement (blue) traces for a single flicker noise experiment, with G_{avg} indicating the average conductance during the hold period (blue bracket). **B.** Sample Noise Power Spectral Densities (PSDs) can be obtained by transforming the hold period conductance from the time domain to the frequency domain using the discrete Fourier transform (dFT). The yellow shaded region represents the noise power integrated from 100 Hz to 1000 Hz. **C.** Averaged conductance noise PSDs of 1-methylimidazole (1MeIm) in blue and 1,6-hexanediamine (C_6) in red; the black dashed line indicates the $f^{-1.4}$ dependence.

We focus solely on the conductance observed during the holding phase for data analysis. We select only those traces where conductance signals fall within the histogram peak width of the target molecules. Then we perform a scaled discrete Fourier transform (dFT) on the selected data to convert from the time domain to the frequency domain (Figure 2-7B). To confirm the presence of flicker noise within our molecular junction, we average all frequency domain traces and fit the segment from 100 Hz to 1000 Hz to a power law, as shown in Figure 2-7C. This confirms the $f^{-1.4}$ dependency across all molecular junctions of interest. Two key parameters are required to determine the nature of the interaction within a particular molecular junction: the average conductance (G_{avg}) of the conductance

and the average noise power during the hold period. We construct a Power Spectrum Density (PSD) as follows,

$$P(f) = \frac{|F(f)|^2}{N}$$

where $F(f)$ is the dFT of the conductance during the hold period, and N is the number of data points. The average noise power was computed by integrating each PSD trace between 100 Hz and 1000 Hz.

Adak et al. have also established a method to distinguish the dominant interaction in a junction by examining how the noise power scales with the average conductance.⁷⁶ They have found that the noise power scales with the N -th power of the average conductance, G^N . If the scaling exponent N is larger than 1.4, this suggests that the dominant interaction in the junction is through-space. Conversely, if N is approximately 1, the dominant interaction is through-bond.

To obtain the coefficient N , we apply Pearson's correlation analysis on the (noise power/ G^N) against G_{avg} to derive the coefficient N , using values ranging from 0 to 4 in steps of 0.01. We can locate the exponent N where the correlation between (noise power/ G_{avg}^N) and G_{avg} equals zero, as shown in Figure 2-8A. We experiment with two control molecules, 1,6-hexanediamine (C_6) and 1-methylimidazole (1MeIm), known to bind through bond and space, respectively. We have determined the coefficient to be $N = 0.91$ for C_6 and $N = 1.70$ for 1MeIm, which confirms prior knowledge about their binding and transport in the junction.^{76,79}

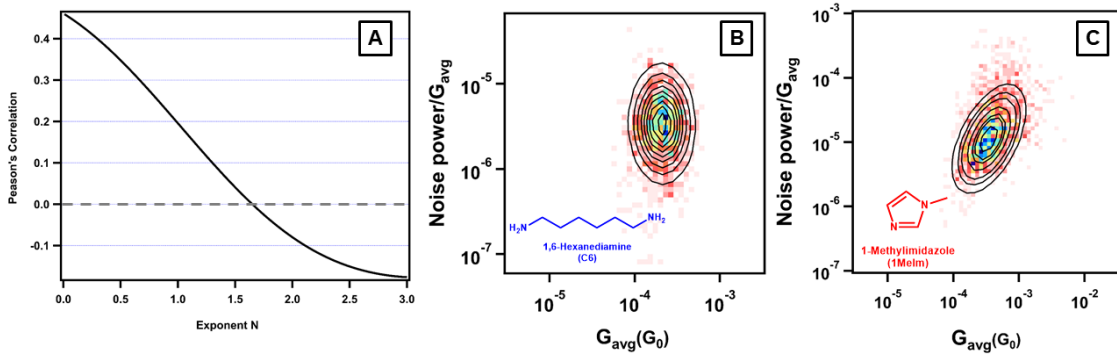


Figure 2-8. A. Correlation of noise power/ G^N with the average junction conductance (G_{avg}) for 1MeIm. The dashed grey line indicates where the correlation equals zero, corresponding to a scaling exponent N of 1.7. B. Two-dimensional histogram of noise power/ G_{avg} against G_{avg} for C_6 , black lines showing the 2D Gaussian fits. Inset: Chemical structure of C_6 . C. Two-dimensional histogram of noise power/ G_{avg} against G_{avg} for 1MeIm, black lines showing the two-dimensional Gaussian fits. Inset: Chemical structure of 1MeIm.

To enhance our visualization of these results, we can create a two-dimensional histogram of the averaged noise power/ G_{avg} versus G_{avg} shown in Figures 2-8B and C. A two-dimensional Gaussian fit is used to identify the contour shapes of the histogram. A leveled circular contour suggests through-space interactions, as shown in Figure 2-8B, while a tilted contour in Figure 2-8C suggests through-space interactions.

CHAPTER THREE pH-Activated Single Molecule Conductance and Binding Mechanism of Imidazole on Gold

3.1 Preface

A version of this chapter has been published in Nano Letters, authored by Xiaoyun Pan, Brent Lawson, Andrea M Rustad, and Maria Kamenetska.²⁶ I conducted the scanning tunneling microscope break junction (STMBJ) measurements and data analysis for this work. I want to express my gratitude to Brent Lawson for performing the Density Functional Theory calculations, Andrea Rustad for her assistance in data collection, and Maria Kamenetska for her guidance throughout the project.

3.2 Introduction

The chemistry required to enable effective and reproducible assembly of and charge transport across metal-molecule-metal junctions is an ongoing area of research.^{40,80–82} Because the chemical link between the metallic and organic components in a circuit determines both the stability of the device and the contact resistance between components, the required chemistry must be robust but also selective. Most existing binding chemistries, such as thiol-Au or amine-Au, present a trade-off between bond strength in the prior and bond selectivity in the latter case.^{43,81,83}

Here we demonstrate electrically robust and persistent, pH-activated metal-molecule-metal junctions formed with imidazole (Im) on gold. Im is an organic cyclic compound whose structure is shown in the inset of Figure 3-1A; it is a key component of biological molecules—purine DNA bases as well as the amino acid histidine.^{84,85} We

measure the conductance of imidazole and its derivatives at room temperature and perform density functional theory (DFT) calculations to identify the new binding mechanism responsible for forming these stable metal-molecule-metal junctions at room temperature. We find that robust junctions are formed with deprotonated molecules, imidazoles (Im^-), which coordinate to the gold electrodes through the nitrogen atoms; the junctions are stabilized by the image-charge interactions with the metal surface without losing binding selectivity. Using this chemistry, we are able to assemble single molecular-metal chains, composed of two Im^- molecules bound in series through a gold atom, while measuring their conductance at room temperature.

3.3 Results and Discussion

We form single molecule-metal junctions with Im and its derivatives using a home-build Scanning Tunneling Microscope break junction (STMBJ).⁸⁶ Our experimental protocol is based on Chapter 2. Briefly, we bring a gold tip repeatedly in and out of contact with a gold-coated metal substrate using a high-resolution piezoelectric positioner. Conductance is measured at a constant bias of 500 mV while the substrate is moved away from the tip at 20 nm/sec. We deposit molecules on the gold substrate by dip coating it in 1 millimolar (mM) solution of the molecules in various solvents. The sample is dried before measurement, as detailed in Chapter 2, so no tip insulation is required here.

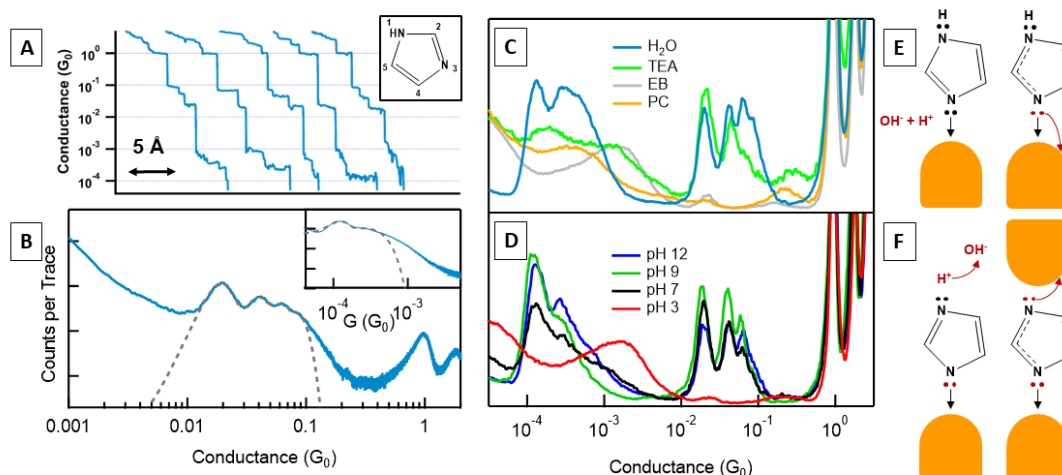


Figure 3-1. A) Sample conductance traces measured in the presence of imidazole dip coated on the gold sample from water. Inset: Chemical structure of imidazole with atomic positions numbered B) Linear binned histograms of Im deposited out of water, showing the high-G region (bin size = 10^{-4}) and the low-G region (inset; bin size = 10^{-6}). The dashed lines represent four and two Gaussian fits to the high-G and low-G regions, respectively. The most likely conductance values corresponding to the centers of these distributions are found to be $1.9 \times 10^{-2} G_0$, $4.0 \times 10^{-2} G_0$, $6.2 \times 10^{-2} G_0$, and $8.1 \times 10^{-2} G_0$; be $1.2 \times 10^{-4} G_0$ and $2.4 \times 10^{-4} G_0$ for low-G. C) 1D log-binned conductance histograms constructed from at least 4000 traces of imidazole dip coated onto gold from various solvents. D) Conductance histograms of Im deposited out of aqueous solutions of varying pH constructed without data selection from at least 5000 traces. E) The proposed mechanism for Im binding Au in basic conditions through the 3N lone pair. F) Proposed mechanism for the Au-catalyzed deprotonation of imidazole in basic conditions and for the formation of Au-Im-Au junctions.

Figure 3-1A shows sample conductance traces collected in the presence of Im deposited using this dip coating method from water (Sigma Aldrich W4502). As usual, we observe plateaus at decreasing integer values of G_0 , indicating the mechanical thinning of gold molecular wires until a single atom with conductance of $1 G_0$ bridges the electrodes prior to rupture. In addition, at least 50% of the traces measured in the presence of Im show multiple plateaus between $10^{-2} G_0$ and $10^{-1} G_0$ (high-G region) and between $10^{-4} G_0$ and $10^{-3} G_0$ (low-G region). To determine statistically significant conductance values, we construct

a 1D conductance histogram out of 6000 traces of Im on gold deposited out of water without any data selection. The resulting histograms are shown in Figure 3-1B using linear binning and in Figure 3-1C using log binning, and reveal several distinct peaks in both the high-G region (main figure, bin size is $10^{-4} G_0$) and in the low-G region (inset, bin size is $10^{-6} G_0$).⁸⁷ Dashed lines in Figure 3-1B show four Gaussian fits to the high-G region and two Gaussian fits to the low-G region; we observe that molecular peaks occur at multiples of $1.9 \times 10^{-2} G_0$ and at multiples of $1.2 \times 10^{-4} G_0$, suggesting that multiple molecular structures can bind in parallel in our junctions to produce distinct molecular conductance signatures over many orders of magnitude. These sharp peaks observed in the histograms confirm that this molecule deposited out of water forms robust metal-molecule-metal junctions on gold with several statistically significant conductance signatures.

Such conductance phenomena have not been observed with neutral amines, pyridines or nitriles, which coordinate to gold through donor-acceptor bonds with nitrogen producing relatively weakly-bound metal-molecule junctions with no more than two molecules binding in the junction in parallel.^{45,88,89} Here, we postulate that the two nitrogen atoms in Im in positions 1 and 3 (Figure 3-1A) provide the anchor points of the molecule to the gold electrodes and that Im is deprotonated in this process in position 1 (inset of Figure 3-1A). To test this hypothesis and determine the binding mechanism of our molecular junctions, we perform break junction measurements on Im as a function of solvent polarity and basicity. The conductance histograms of Im deposited from ethyl benzoate (EB), propylene carbonate (PC), triethylamine (TEA), and water are shown in Figure 3-1C. More solvent-dependent conductance data are included in Figure 3-2, and the

complete list of solvents used in the study and their properties is listed in Table 3-1. We find that metal-molecule junctions with Im form only in relatively basic solvents such as TEA or water. In contrast, no junctions are observed in EB or PC, which is highly polar but acidic compared to Im shown in Table 3-1. These results rule out solvent polarity or water specifically as decisive in enabling molecular junction formation.

Solvent	pK _a	Dipole Moment (D)
Ethyl Benzoate (EB)	-6.5 ⁹⁰	2 ⁹¹
N, N-Dimethylformamide (DMF)	-0.3 ⁹²	3.82 ⁹¹
Propylene Carbonate (PC)	3.92 ⁹³	4.9 ⁹¹
Pyridinium (conjugate acid of pyridine)	5.23 ⁹¹	2.215 ⁹¹
Triethylammonium (conjugate acid of Triethylamine)	10.75 ⁹¹	0.66 ⁹¹
H ₂ O	14 ⁹⁴	1.8546 ⁹¹

Table 3-1. The pK_a values and dipole moments of the solvents used in this study.

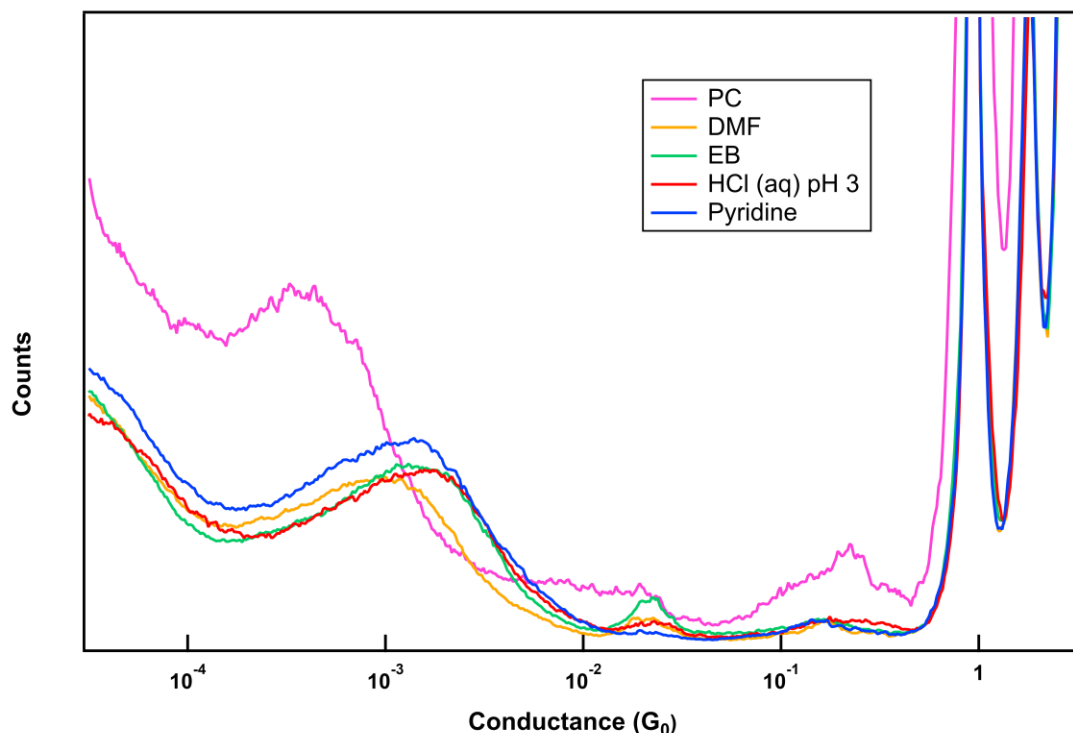


Figure 3-2. Conductance histograms of imidazole dissolved in acidic aqueous solvents and polar aprotic organic solvents were obtained from a minimum of 4000 traces.

We confirm and quantify the dependence of junction formation on environmental basicity by measuring the conductance of Im deposited from aqueous solutions of varying pH. The conductance histograms made from at least 6000 traces measured on Im deposited out of solution with pH 3, 7, 9, and 12 are shown in Figure 3-1D. We observe that at pH value below 7, the conductance features in the high and low-G regions do not occur. Instead, a broad feature around $10^{-3} G_0$ is observed at pH 3 and other acidic solvents (Figures 3-1D and 3-2), which may correspond to π - π stacked molecules physisorbed in the junction.⁷⁹ In contrast, in basic conditions, this broad feature disappears in favor of the sharp peaks discussed above, signaling that at high pH Im^- bridges the tip-sample gap by binding to both electrodes. Interestingly, the cutoff for junction formation occurs at pH 7

and coincides with the pK_a of the N3 position in Im, suggesting that the availability of the lone pair at position 3 to bind is necessary to form molecular junctions.⁴⁵ Based on this evidence, we postulate that the N3 position is one of the binding sites of the molecule to the electrodes, as depicted in Figure 3-1E. In Figure 3-1F, we show that once the lone pair on 3N binds to the gold, the N1 site becomes more acidic and can become deprotonated in basic conditions. We hypothesize, therefore, that the second binding site of Im⁻ in the junction is through the deprotonated N1 nitrogen.

To test the role of this pyrrole nitrogen in position 1 on junction formation, we measure the conductance of a series of imidazole derivatives, with a methyl group substituted for hydrogen at the 1, 2 and 4(5) positions, 1-MeIm, 2-MeIm, 4-MeIm, respectively, as shown in the inset of Figure 3-4A. As expected, 1-MeIm, where the N1 position has been methylated, is distinct from all other molecules in our series and does not bind in the junction in either the high or low-G conductance configurations, regardless of pH. This result conclusively demonstrates that deprotonation at the N1 position is necessary for the formation of single molecule junctions. In contrast, the 2- and 4-MeIm do show conductance features in the high and low-G regimes in basic conditions, indicating that the carbon atoms in the imidazole ring do not participate in binding. Notably, the pH cutoff above which these molecular conductance signatures are present is ~ 7.5 and 8 for 4-MeIm and 2-MeIm, respectively. This value is higher than the cutoff for Im and correlates with higher pK_a of the nitrogen at the N3 position in these molecules, which we measure to be ~ 7.5 and ~ 8 for 4-MeIm and 2-MeIm, respectively, shown in Figure 3-3. This pH dependence of junction formation supports our hypothesis that the donor-acceptor bond

between the N3 lone pair and the electrode drives the deprotonation at the N1 position, where the second molecule-metal bond can form.^{95,96} Our data conclusively identifies the nitrogen atom lone pairs as the anchoring points for Im⁻ in gold junctions. Binding through the π -orbitals is inconsistent with published results and the persistent conductance plateaus observed here.^{51,97}

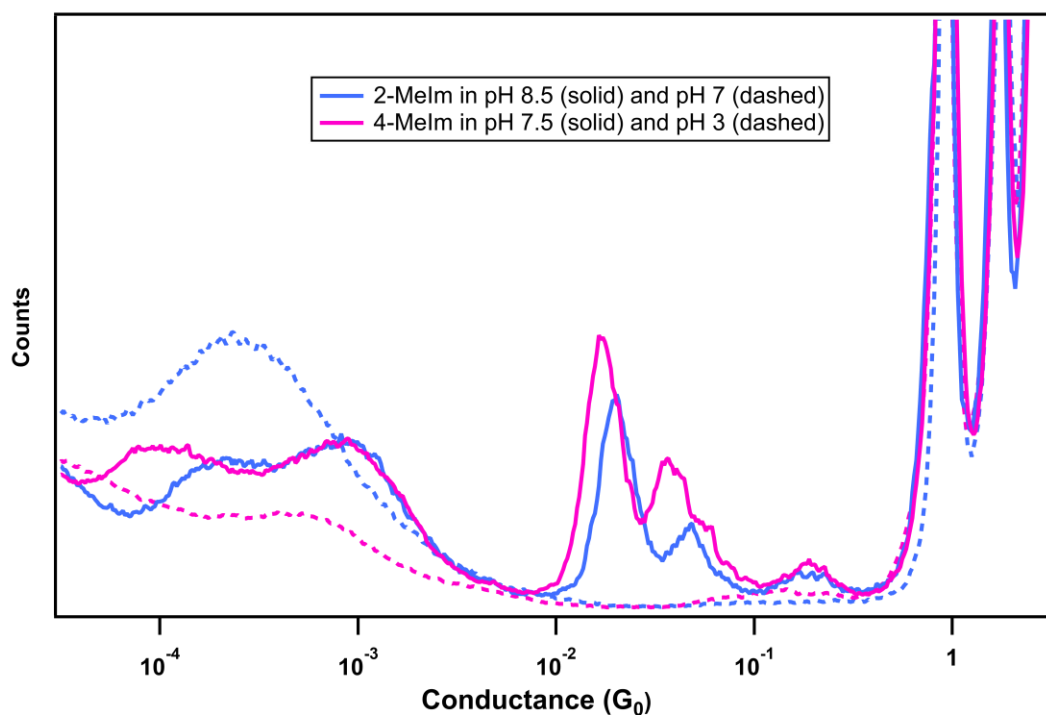


Figure 3-3: Conductance histograms for 2-Methylimidazole and 4-Methylimidazole, constructed from 4000 traces. Measurements were taken at pH levels both above (solid lines) and below (dashed lines) the pK_a values of the molecules.

A comparison of the conductance histograms of the 4- and 2-MeIm with Im reveals that Im is relatively more likely to form peaks at higher multiples of the high-G base value of $1.9 \times 10^{-2} G_0$ than the methylated molecules. It is likely that greater steric repulsion of the bulkier CH₃ groups prevents the formation of molecules bound in parallel. To further

test this hypothesis, we examine how the density of molecules around our junction affects our conductance signatures; we expect configurations requiring more molecules to be less probable at lower concentrations. We perform conductance measurements on Im deposited out of pH 12 aqueous solutions of various concentrations and plot the resulting conductance histograms in Figure 3-4. We observe that at 0.1 mM concentration or lower, only a single peak at $1.9 \times 10^{-2} G_0$ is present in the histogram. We attribute this peak to a junction with a single Im^- molecule and call it the single high-G peak. As the concentration is increased, conductance features that require more than one molecule begin to appear in the histograms. Notably, the double high-G peak at $3.9 \times 10^{-2} G_0$ appears next and at the same concentration of ~ 0.25 mM as the peak at $1.2 \times 10^{-4} G_0$ in the low-G region, suggesting that both junction configurations involve two Im^- molecules. As expected, higher multiples of molecular conductance become prominent at higher concentrations. We note that the double low-G peak at $2.4 \times 10^{-4} G_0$ appears only at the highest concentration of 1 mM. These results strongly suggest that higher multiples of the high-G feature require an increasing number of molecules likely bound in parallel; furthermore, the data also indicate that the single and double low-G plateaus require at least two and four molecules, respectively.

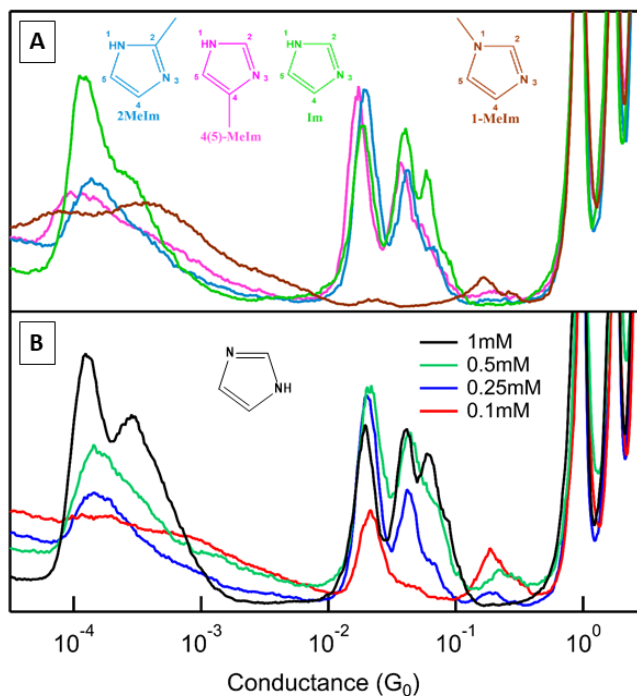


Figure 3-4. A) Conductance histograms of Im, 4-MeIm, and 2-MeIm in pH 9 and 1-MeIm in pH 12 were constructed from at least 5000 traces. Inset: structures of the molecules. B) Conductance histograms of Im constructed from at least 9000 traces each, measured on samples prepared with aqueous solutions at pH 12 containing differing concentrations of imidazole.

To better understand the junction geometry responsible for the two conductance regimes observed (high-G and low-G), we construct a 2D conductance and displacement histogram, as detailed previously, from 10,000 traces of Im on gold from water without data selection, shown in Figure 3-5A.²⁷ The distance axis in this 2D histogram reveals the elongation sustained by the junction in different conductance configurations. We see, for example, that the single high-G feature persists through as much as 3 Angstroms (\AA) of junction elongation.⁴⁵ This is longer than the N-N distance in imidazole itself, which is $\sim 2.2\text{\AA}$, and suggests that structural rearrangement of the electrode must occur during junction stretching to account for the conductance plateau lengths observed. In particular,

this feature is similar in length to the $1 G_0$ plateaus, suggesting that similar plastic deformation may account for the persistence of both conductance features. This phenomenon has only been observed with covalently-bound junctions formed, such as thiol linkers.^{81,98,99} In junctions formed with amine (NH_2) or pyridine-terminated molecules, the Au-N link is weaker than an Au-Au bond and is the first to rupture during elongation so that molecules can change attachment point but not deform the electrode; as a result, amine-terminated molecules shorter than 5 \AA remain bound for 1.5 \AA at the apex of the electrodes.^{27,40,100,101} This contrast in persistence statistics between imidazole and other nitrogen-linked junctions supports our observations above that the Im junctions form through a different chemistry, where the hydrogen is removed to result in Au-Im⁻-Au junctions. We hypothesize that the charge on the molecule leads to more robust binding by polarizing the surface and allows for multiple molecules bound in parallel, as shown in Figure 3-5B.

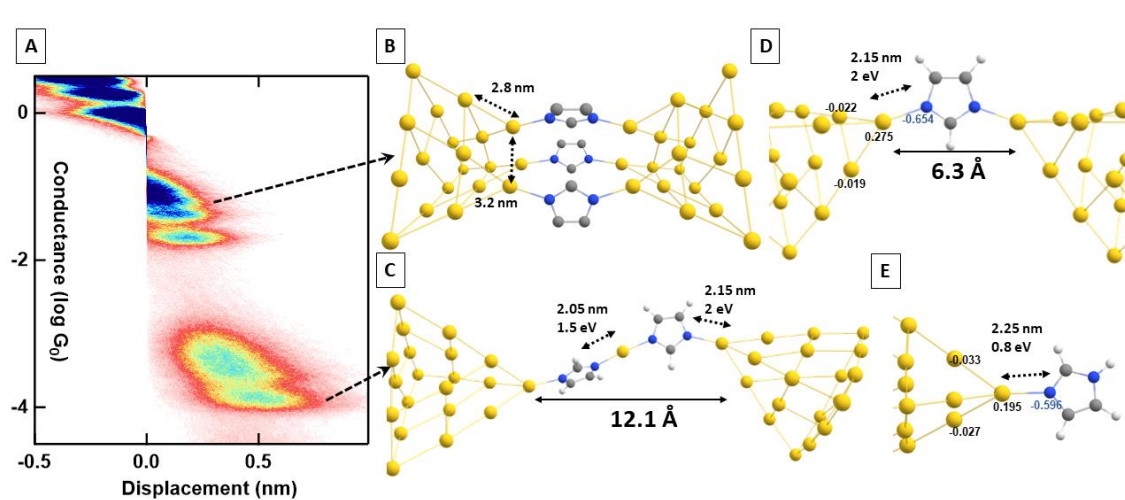


Figure 3-5: A) 2D conductance-displacement histogram constructed from 10000 traces of imidazole dip coated from water. B-E) The calculated structure and binding energy of various

Au-Im configurations: (B) three Im⁻ ions bound in parallel on blunt Au₁₉ pyramids (hydrogen atoms omitted for clarity); (C) the Au-Im⁻-Au complex; (D) the Au-Im⁻-Au chain; (E) the Im-Au complex. The labels on atoms around the Au-N bonds in (D) and (E) indicate the total charge on the atom.

We now turn to the origin of these low-G conductance features. According to Figure 3-5A, these low-G configurations can form starting at ~ 2 Å of stretching and persist until ~ 8 Å of stretching after the $1 G_0$ gold point contact rupture. These distances rule out the possibility that a single imidazole molecule can bridge this gap and indicate that a more extended molecular structure is formed during junction elongation. Drawing from the analysis of the concentration data, it suggests that two molecules participate in the single low-G feature at $1.2 \times 10^{-4} G_0$, and we propose that molecules of Im⁻ bind in series through a single gold atom, as depicted in Figure 3-5C. Evidence of plastic deformation of electrodes upon junction stretching in the 2D histogram suggests that Im⁻-Au bond strength is comparable to the Au-Au bond and can extract gold atoms out of the surface to pull out chains of repeating Im⁻-Au units; we hypothesize that these in situ-formed dimers can account for the low-G conductance plateaus at $\sim 2-8$ Å after G_0 rupture. Other extended configurations based on hydrogen bonding between imidazoles or with water are not consistent with published results or with the data presented here, which show that low-G conductance features can form both in non-aqueous basic conditions as well as in water. Imidazole has previously been found to form chains with silver atoms on the surface.¹⁰² Furthermore, polymer assembly has been observed with other charged linkers in single molecule conductance experiments. We propose that pH-activated and Au-promoted deprotonation of Im can account for this phenomenon.¹⁰³

Brent Lawson performed density functional theory calculations (DFT) in Gaussian to confirm the binding chemistry and possible configurations of single or multiple Im^- on Au and the formation of Im^- -Au chains.^{104,105} We employ the functionals PBE^{106,107} and B3LYP^{108,109} with Def2-SVP and Def2-SVPD¹¹⁰⁻¹¹² as the basis sets and core potentials to calculate and compare the binding energies of Im^- , Im, and a trimer of Im^- to gold electrodes modeled as 20-atom gold pyramids (Au_{20}) or blunt 19-atom gold tips (Au_{19}) shown in Figure 3-5B. We calculate that Im^- on Au can form stable metal-molecule-metal junctions with Au-N bond strength of $\sim 2\text{eV}$, as shown in Figure 3-5D.¹⁰⁰ We note that we did not find a stable bridging configuration of the neutral Im in the junction. Instead, a neutral Im coordinates to one electrode only through the pyridine N3 atom, as shown in Figure 3-5E, with a bond strength of $\sim 0.8\text{ eV}$, consistent with prior results.^{10,45} Interestingly, we see that the orientation of the metal-molecule bonds in the Au- Im^- -Au junction in Figure 3-5D is virtually unchanged compared to the neutral Au-Im structure in Figure 3-5E. The direction of the Au-N bond remains perpendicular to the π system in both cases, but it becomes shorter when the molecule is charged, reflecting a stronger polarization of the metal electrodes in response to the negatively charged molecule, as the total charge labeled on the atoms surrounding the molecule metal bond in Figure 3-5D and E.¹¹³⁻¹¹⁵ We emphasize that the 2eV binding energy per Au-N bond calculated above for Im^- in the junction is comparable to the binding energy of an Au-Au bond.^{99,101,116} Given the similarity in bond strength, the junction may break at an Au-Au link, leaving an Im^- Au complex which can then form metal-molecule chains in situ, as depicted in Figure 3-5C. Our calculations predict a binding energy of at least 1.5eV for Au-N bonds in the extended structure. This

relative stability can account for the plateaus observed in the low-G regime. We note that the broader histograms of the low-G configurations may be due to this slightly lower binding energy and an increased number of binding configurations. For example, one of the possible geometry could be the gold-molecule chain attached higher up to the gold pyramid with extra electronic coupling occurring through the π -orbital.⁴⁵ Nevertheless, as in the single Au-Im⁻-Au junction, DFT calculations indicate that the specificity of the Au-N bond is retained, and the interaction is strengthened by the electrostatic effect, leading to robust and reproducible conductance plateaus observed in the low-G region.

As mentioned earlier, we also calculate the binding energy of a trimer of Im⁻ ions bound on a blunted electrode shown in Figure 3-5B. We observe that despite the negative charge on the molecules, such junctions with multiple Im⁻ molecules are stable, with each Au-N bond contributing ~ 1.1 eV to the total binding energy. Based on our calculation, the Im-trimer dipoles arrange head-to-tail to partially offset the electrostatic repulsion. Thus, the binding energy per bond is less than the single Im⁻ junctions in Figure 3-5D, but still more robust than the pyridine-linked junctions and may explain why the higher-G peaks in the 2D histogram in 3A can sustain less elongation. Importantly, our calculation shows that the binding of several molecules in parallel disrupts the electrode, as can be seen by the increased distance between terminal Au atoms in Figure 3-5B. We hypothesize that this effect promotes the extrusion of Au atoms upon Im⁻ junction elongation and strengthens our argument that chains of Im⁻-Au units bound in series correspond to the low-G conductance signatures.

3.4 Conclusion

In conclusion, we discover a pH-dependent mechanism for forming robust and selective single molecule-metal junctions with well-defined electrical properties. Experimental measurements and DFT calculations indicate Im⁻-Au linked junctions retain the selectivity of donor-acceptor bonds that result in reproducible conductance signatures but are stabilized by the electrostatic effect at the metal surface which results in a binding strength comparable to covalent links. These metal-molecule structures can sustain extended junction elongation through plastic deformation of the Au electrodes and the pulling-out of two repeating Im⁻-Au units to bridge the junction at room temperature. We emphasize that the selectivity and robustness of this new linker motif allow us to assemble these new metal-molecule structures in situ and to characterize their conductance simultaneously. This work is the first demonstration of pH-controlled, in-situ chain assembly, and it dovetails with a recent report of polymer formation in a break junction measurement with isocyano linkers.¹⁰³ These experiments point to a new paradigm of reproducible single-molecule junctions based on charged moieties that can be controlled electrochemically. Our results also open the door to performing robust electrical characterization of single biological molecules bound directly through two natively occurring imidazole moieties or synthetic systems that take advantage of the selective yet tight binding chemistry.

CHAPTER FOUR Cooperative Self-Assembly of Dimer Junctions Driven by π -Stacking Leads to Conductance Enhancement

4.1 Preface

The work presented in this chapter has been submitted for publication during the writing of this thesis. I am the primary author of this work, responsible for the experimental design, data collection, analysis, and interpretation. My co-author, Enrique Montes, has significantly contributed to the computational work of this chapter. Wudmir Y. Rojas and Brent Lawson have conducted initial theoretical investigations. This research project has been co-supervised by Hector Vazquez and Maria Kamenetska, whose guidance and insights have been invaluable. Enrique Montes, Wudmir Y Rojas and Hector Vazquez are from The Institute of Physics, Czech Academy of Sciences. The feedback and insights received during the review process have been implemented in refining this chapter.

4.2 Introduction

Creating conductive and tunable single molecule devices remains the long-term challenge of molecular electronics.^{22,117,118} Efforts to engineer the electronic structure of molecular junctions have focused on leveraging synthetic control to create molecules with desired functionality.^{22,119–121} Typically, molecules with pre-designed components are synthesized and then introduced into the junction, where they can bridge two electrodes through a pair of substituent linker groups.⁴

An alternative approach is to design molecular components which can rearrange and self-assemble into novel molecular structures in the junction.^{26,48,122} For example, imidazole (Im), a conjugated five-member heterocycle, can become deprotonated to

imidazolate in the junction environment and then bridge gold electrodes to form Im-gold bridges.^{25,26,123,124} Other work shows that intermolecular interactions can be harnessed to create new junction structures.^{50,125,126} For example, researchers have synthetically manipulated π - π coupling between oligo-phenylene-ethynylene (OPE) molecules to achieve junctions with through-space transport,⁴⁹ quantum interference,⁵⁰ and environmental controls.⁵² Additionally, other conjugated molecules containing multiple π - π stacked units were observed to demonstrate a significant increase in conductance due to constructive quantum interference.^{51,127}

Here, we demonstrate that intermolecular van der Waals interactions like π - π stacking can drive cooperative binding of several molecules between metal electrodes and promote the formation of molecular dimer junctions with enhanced conductance per molecular unit. We show that benzimidazole (BI), a larger heterocycle containing an Im fused to benzene, assembles to bridge two gold electrodes upon deprotonation, just like the Im reported previously. Unlike Im, BI creates junction structures with multiple conductance peaks, which are not integer multiples of a monomer junction, but display a higher conductance per molecule. Density Functional Theory (DFT) calculations show that van der Waals intermolecular interactions between the aromatic BI molecules stabilize the π - π stacked BI dimers over other molecular arrangements in the junction and that intermolecular binding energy is ~ 20 times $k_B T$. In contrast, the Im dimer binding energy is much less sensitive to the relative orientation between the molecules. Transport calculations show that energetically preferred BI dimer junctions are stabilized by intermolecular interactions in a junction conformation with higher conductances per

molecule than monomer junctions. We demonstrate how we can tune this cooperativity effect and overall junction conductance through synthetic substitution of Im derivatives by designing a phenyl-substituted Im with increased intermolecular interactions that assemble into more transparent dimer junctions than BI or Im. This work demonstrates a new self-assembly approach that leverages intermolecular interactions to achieve molecular junctions with improved electronic properties.

4.3 Additional theoretical calculation methods

4.3.1 Calculations of junction geometry and transmission properties

The geometry of BI and Im junctions was calculated using SIESTA.¹²⁸ Unit cells comprised the molecule, trimer Au tip motifs, and six Au(111) layers, each containing 25 Au atoms. Molecular atoms were described using a double-zeta polarized basis set, while a single-zeta polarized basis was used for Au atoms. Reciprocal space was sampled using a $2 \times 2 \times 1$ Monkhorst pack grid, while a real space grid was defined with an equivalent cutoff energy of 250 Ry. Van der Waals dispersion forces were included using the non-local vdW-DF functional of Dion et al. in the implementation of Román-Perez and Soler.^{129,130}

The position of all molecular and tip atoms was allowed to relax until the Hellmann-Feynman forces acting on these atoms were smaller than $0.02 \text{ eV}/\text{Å}$. Zero-bias transmission calculations were performed within the non-equilibrium Green's function method using TranSIESTA.¹³¹ Extra Au layers were added to converged geometries to compute spectra at optimized geometries. The electronic structure and transmission spectra were calculated using $5 \times 5 \times 1$ and $15 \times 15 \times 1$ Monkhorst-Pack grids, respectively.

The energy profile of molecular dimers was calculated as a function of the relative angle θ between two molecules. When $\theta = 0$, two molecules are completely parallel to each other; when $\theta = 90$, two molecules are perpendicular to each other. The θ was computed as follows: to preserve the relative angle θ , the position of C and N atoms in each molecule was restricted. Their relative positions were constrained such that each molecular backbone could rigidly translate but not rotate, thus preserving the value of θ along the scan. Each molecule in the dimer could move independently of each other. H and Au atoms were allowed to move with no restrictions. For every θ , molecular and tip atom coordinates were optimized this way until forces on each atom were lower than 0.02 eV/Å.

4.3.2 Binding energy at the junction

The binding energy of BI and Im monomers and dimers at the interface was calculated as follows,

$$E_b = E_{\text{Junction}} - (E_{\text{mol}} + E_{\text{Au}})$$

where E_{Junction} is the total energy of the junction in a fully optimized configuration, E_{mol} is the energy of the molecule obtained by cleaving the Au-N bonds in a spin-unrestricted calculation, and E_{Au} is the total energy of the Au tips and electrode layers. The geometry of all structures was fully optimized as described in the previous section, and no constraints were applied. Corrections to basis set superposition errors were included.

4.3.3 Gas-phase intermolecular energy calculation

The gas-phase intermolecular energy was calculated for all dimers. The protonated, neutral form of each molecule was considered here. The basis set and force cutoff described

above were used, and calculations were performed at the Gamma point. The intermolecular energy was computed as follows,

$$E_{\text{inter}} = E_{\text{dimer}} - (E_1 + E_2)$$

where E_{dimer} is the energy of the dimer in the gas phase when the geometry is fully optimized, and E_i is the energy of each fully relaxed isolated molecule. Both parallel (P) and antiparallel (AP) configurations were considered.

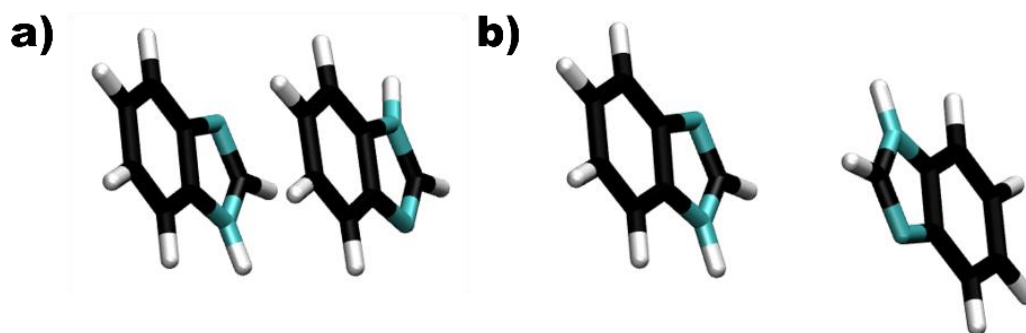


Figure 4-1. Geometry of the gas-phase BI dimer in the a) parallel and b) antiparallel configuration

4.4 Results and Discussion

We perform Scanning Tunneling Microscope Break Junction (STMBJ) measurements using a home-built setup as previously described.^{20,21,67} Briefly, we bring two gold electrodes into contact and then record a conductance trace while the electrodes are retracted. The resulting traces show the evolution of conductance during junction displacement and rupture. Thousands of such traces are measured in the presence of molecules of interest dried on the surface and display conductance plateaus which can be attributed to molecules bridging the electrodes. To deposit, all molecules are dissolved in water (Sigma Aldrich #W4502) or ethanol (Sigma Aldrich #E7023), depending on

solubility, to a concentration of $\sim 1\text{mM}$. Sodium hydroxide (Sigma Aldrich, #901915) is used for adjusting the pH to 12; the basicity of the solution is verified with pH strips (Sigma Aldrich, Hydrion® pH 6.5 - 13.0). Prior to conductance measurements, the gold-coated substrate is submerged into the prepared solution for at least 15 minutes, oven-dried at 55°C , and cooled to room temperature. Sample traces are shown in Figure 4-2a. 2D histograms constructed out of at least 5000 such traces collected in the presence of BI and Im without data selection are shown in Figure 4-3a and b, respectively.²⁷ To construct 2D histograms, we assign the $1G_0$ rupture event, corresponding to the breaking of the single gold atom chain, to be the origin along the displacement axis in all traces and bin the logarithm of conductance and displacement of each data point in the trace to create 2D heat maps. Reproducible molecular conductance signatures appear as plateaus in the histogram at lower conductance values following $1G_0$ rupture and correspond to molecules bridging gold electrodes. By binning the conductance only, we obtain 1D histograms, shown in Figure 4-3c, where molecular signatures appear as distinct conductance peaks.

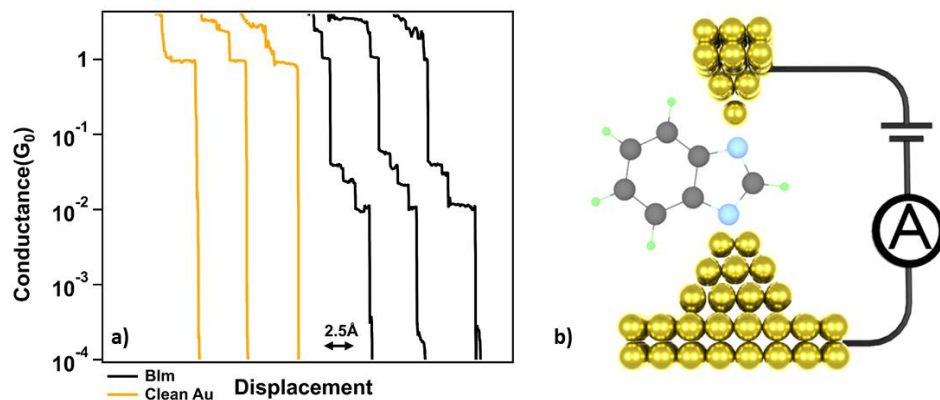


Figure 4-2. a) Sample conductance traces showcasing a clean gold (Au) junction (depicted in yellow) and an Au-BI-Au junction (shown in black). b) A schematic representation of a molecular junction featuring BI and two gold electrodes. A bias is applied across the junction, and the resulting current is measured.

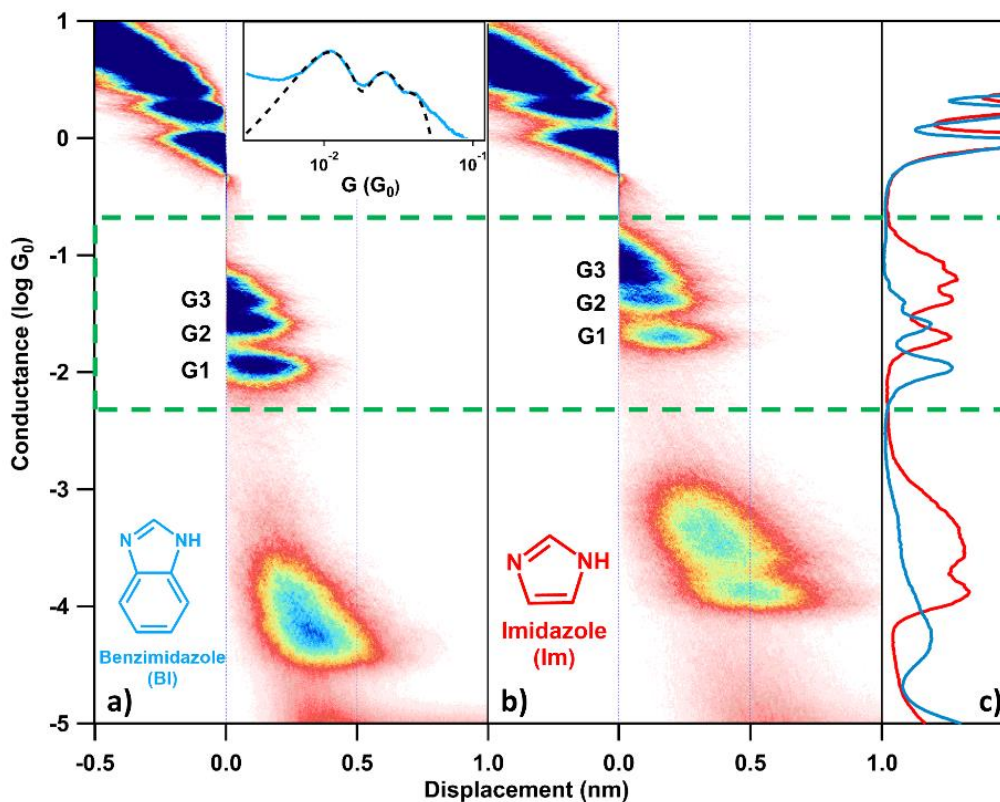


Figure 4-3. a) 2D histogram of benzimidazole; inset: chemical structure of benzimidazole. b) 2D histogram of imidazole; inset: chemical structure of imidazole. c) 1D histogram of benzimidazole (blue) and imidazole (red). The green dashed box contains the conductance region of interest in this work.

We note that the conductance signatures observed for BI are similar to those of Im, published previously.^{26,123} In earlier work, the low conductance peaks (LG) have been attributed to in situ assembly of extended structures in the junction.^{26,123} In this work, we focus on the high conductance region (HG) boxed in green in Figure 4-3a-c. Several distinct features labeled as G1-3 are present both in the Im and BI histograms in the HG region. We observe that the length of these features in the 2D histograms (Figures 4-3a-b) is very similar for both molecules and strongly suggests identical binding geometries are responsible for the formation of these molecular junctions with BI and Im.

In addition, we observe that BI only forms junctions in neutral to basic conditions, as has also been previously reported for Im.^{25,26,132} This result indicates that deprotonation of the BI at the nitrogen linkers is required for junction formation. The similarity of pH-dependent conductance signatures for BI and Im establishes that the same binding mechanism is responsible for the HG peaks of both molecules. We conclude that BI bridges the gold electrodes by binding through the nitrogen lone pairs of deprotonated molecules, as has been previously found for Im. The HG conductance signals from Im and BI are attributed to monomer (G1), dimer (G2), and trimer (G3) junction formations.

We fit the 1D histograms with a sum of three Gaussian fits to obtain G1-3 conductance values for BI. Results from four experiments are averaged and summarized in Table 4-1. Im fitting results using a similar protocol have been published previously and are reproduced in Table 4-1. We note that the standard error is less than 1%, and the day-to-day variation in G1-3 peak positions is less than 3%. Interestingly, we observe that the monomer peak (G1) conductance is lower for BI than for Im; we measure $1.1 \times 10^{-2} G_0$ and $2.0 \times 10^{-2} G_0$ for BI and Im, respectively. G2 peaks of Im junctions occur at multiples of the Im G1 conductance value, which is expected for molecules binding in parallel to create two uncoupled conductance channels. This phenomenon is reflected in the G2/G1 conductance ratio for Im junctions, which is ~ 2 in Table 4.1. Notably, in BI junctions, comparing the conductance of G1 and G2 peaks, we observe a ratio of G2/G1 equal to 2.3. These results indicate that the conductance of 2 molecules of BI bound in parallel in the junction is more than double the conductance of a single BI monomer by a significant margin. We note that this result is different from previous work, both in early model

approaches,^{133,134} or atomistic calculations and experiments,⁴⁷ which reported increased conductance in double-backbone molecules. While in those cases, the origin was the spectral properties of two molecular structures coupled to the electrodes through *the same* linkers, here, as we show below, the increased per-molecule conductance is due to more transparent geometries induced by the dimer assembly.

	G1 ($10^{-2}G_0$)	G2 ($10^{-2}G_0$)	G2/G1		G1 ($10^{-2}G_0$)	G2 ($10^{-2}G_0$)	G2/G1
Im	1.96	4.08	2.08	BI	1.14	2.62	2.30
2MeIm	1.97	4.36	2.21	2MeBI	1.31	2.94	2.35
2PhIm	2.07	4.94	2.38	2PhBI	1.30	2.79	2.26

Table 4-1. List of measured conductance histogram peak values and their ratios for six molecules studied. Each entry in Table 4-1 is an average of at least 4 experiments conducted on different days with a minimum of 5000 traces collected per experiment. The uncertainty, as measured by standard error, is less than 1%.

To understand these conductance trends and the source of conductance enhancement in dimer junctions, we turn to DFT atomistic calculations. We use the SIESTA¹²⁸ and TRANSIESTA¹³⁵ packages, including van der Waals interactions in a self-consistent description¹³⁶ to calculate the structure and conductance of BI and Im junctions. We build neutral junctions where BI and Im molecules form chemical bonds to the electrodes through Au trimer structures on the (111) surfaces. Each molecule in the simulations establishes a strong Au-N bond to each electrode. The calculated binding energy of individual molecules at the junction is -2.71 eV (BI) and -2.40 eV (Im), shown in Table 4-2. These values are about double and ~30% larger than amine and pyridine-linked molecules, respectively, and are supported experimentally by the relatively longer

molecular features observed in 2D histograms in Figures 4-3a and 4-3b than would be expected for similar length amine alkanes, for example.^{72,137} This result is consistent with the deprotonation of N atoms in BI and Im, where the charge on the molecule reinforces the binding to gold through image-charge interactions, as has been previously shown.^{26,103,124}

Molecular structure	E_b (eV)	Molecular structure	E_b (eV)
BI monomer	-2.71	BI dimer	-5.19
Im monomer	-2.40	Im dimer	-4.74

Table 4-2. Calculated binding energy of BI and Im molecular junctions.

We first investigate the energetics of BI and Im dimers at the junction. Since van der Waals distances between conjugated molecules are comparable to the Au-Au nearest-neighbor separation (~ 3.0 Å), we build junctions where two molecules are bonded to the same tip structures.¹³⁸ For this reason, we use trimer motifs in the structure and electron transport simulations. Figure 4-4a illustrates the unit cell used in the energy profiles, consisting of both molecules bonded to trimer structures and three Au(111) layers. To study the structure of the dimers, we scan the relative angle between both molecules. We constrain the position of all C and N atoms in each molecule such that these atoms can move rigidly but cannot rotate around an axis.¹³⁹ This way, the relative angle between both molecular backbones is fixed. H atoms, as well as Au tip atoms, are allowed to move unconstrained.

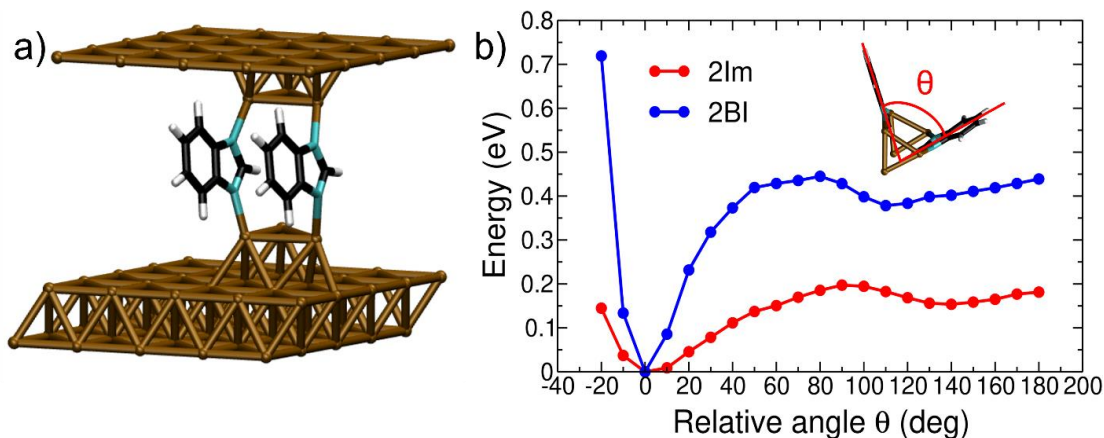


Figure 4-4. a) Unit cell used in the simulations to probe the angular dependence of the total energy in Im and BI junctions with two molecules. B) Total energy (relative to the minimum value of each species) as a function of the relative angle between both molecules, calculated for two Im (red) and two BI (blue) molecules adsorbed on the same tip structures. The inset illustrates the relative angle θ from a top view of the molecules and tip structures.

We prepare junction geometries with a given value of the relative angle θ and relax the junction by allowing each molecular backbone to rigidly move while maintaining the value of θ . Figure 4-4b shows the relative total energy of the junction as a function of θ for BI and Im dimers. Zero energy represents the most stable configuration for each species. In both cases, the most energetically favorable conformation is found when the molecules in the dimer adopt a parallel orientation ($\theta = 0$ deg). There, both conjugated backbones are parallel and π stacking is maximized.¹⁴⁰ At negative values of θ , the molecules are close to each other, and the repulsion of electron clouds dominates. In the positive range, as θ increases, attractive intermolecular interaction is reduced as the conjugated systems are rotated away from coplanarity, and the energy increases. Fig. 4-5 shows that van der Waals dispersion interactions are largely responsible for this intermolecular attraction in BI dimers. Both systems exhibit a second local minimum at large values of θ . For BI dimers,

this happens at $\theta = 110$ deg, and around ~ 0.4 eV less favorable than the parallel arrangement. For Im dimers, these values are $\theta = 140$ deg and ~ 0.15 eV.

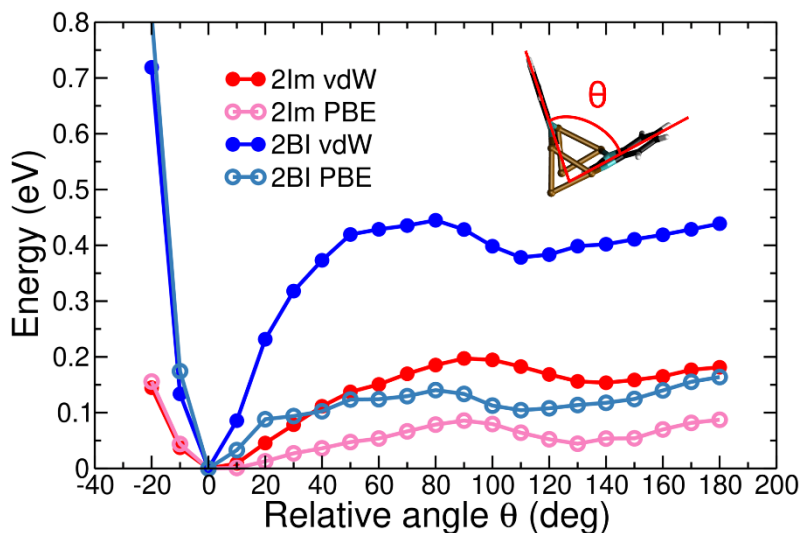


Figure 4-5: Energy scan of BI and Im dimers, as a function of θ , with and without vdW contributions.

A fully relaxed geometry optimization, with no constraints, of the antiparallel orientation finds that BI and Im dimers at the junction also exhibit a local minimum in this configuration, but in both cases, this is less favorable than the parallel arrangement by 0.26 and 0.05 eV, respectively. These relative differences at the junction are consistent with the values found for gas-phase dimers, as shown in Table 4-3.

	P, E_{inter} (eV)	P, $E_{\text{substituted BI/EBI}}$	AP, E_{inter} (eV)	AP, $E_{\text{substituted BI/EBI}}$
BI	-0.60	1	-0.23	1
PhBI	-1.07	1.78	-0.75	3.26
MeBI	-0.68	1.13	-0.65	2.82

	P, E_{inter} (eV)	$E_{\text{substituted Im}}/E_{\text{Im}}$	AP, E_{inter} (eV)	$E_{\text{substituted Im}}/E_{\text{Im}}$
Im	-0.33	1	-0.23	1
PhIm	-0.74	2.24	-0.72	3.13
MeIm	-0.42	1.27	-0.37	1.61

Table 4-3. Calculated intermolecular energies for all gas-phase dimers in the parallel (P) and antiparallel (AP) configurations; intermolecular energy ratios of substituted BI/Im dimer over BI/Im dimers.

To summarize the initial Im and BI packing studies, calculations indicate that in BI dimers, the most likely configuration at the junction is overwhelmingly one where the molecules are arranged in parallel. In contrast, in Im dimers, the energy profile is less sensitive to the relative angle between Im molecules. We conclude that Im dimer junctions are significantly more likely to explore geometries with large relative angles than BI. Although the structures investigated here are simplifications of the actual geometries in the experiment, we expect the findings of Figure 4-4 to be general and applicable.

Having established the most likely relative orientations of Im and BI dimers, we now turn to electron transport simulations. We first discuss the conducting properties of individual Im and BI molecules. We determined the most energetically favorable orientation of single Im and BI molecules at the junction without any constraints and performed electron transport calculations on optimized geometries. Figure 4-6a compares the calculated transmission spectra of Im and BI junctions. Both spectra exhibit sharp features approximately 0.5 eV below the Fermi level, which corresponds to π molecular resonances. Im has a single narrow peak at -0.6 eV, while in BI monomer junctions, two

features are present at -0.6 eV and at -0.4 eV. The real-space representation of the most transmitting orbital at -0.4 energy, shown in Figure 4-6b, reveals that it derives from a π state delocalized over the imidazole and benzene rings. However, at the Fermi energy, the most transmitting orbital have in-plane σ symmetry in both Im and BI junctions. This relationship is evidenced by their real-space representation calculated at the Fermi energy for BI (Figure 4-6c) and Im (Figure 4-6d), which exhibit a very similar nodal pattern to each other. In both molecules, this σ resonance peaks at -1.5 eV, but its coupling at the Fermi energy is lower in BI than in Im. The calculated conductance values of Im and BI are $6.4 \times 10^{-2} G_0$ and $4.2 \times 10^{-2} G_0$ respectively, in reasonably good agreement with the experimentally determined values for the G1 peak listed in Table 4-1.^{120,141,142} In the positive region of the spectrum where $E-E_f > 0$ eV (inset in Fig. 4-5a), multiple transmission peaks are visible close to 3.5 eV (BI) and 4.6 eV (Im) and do not contribute to transport.

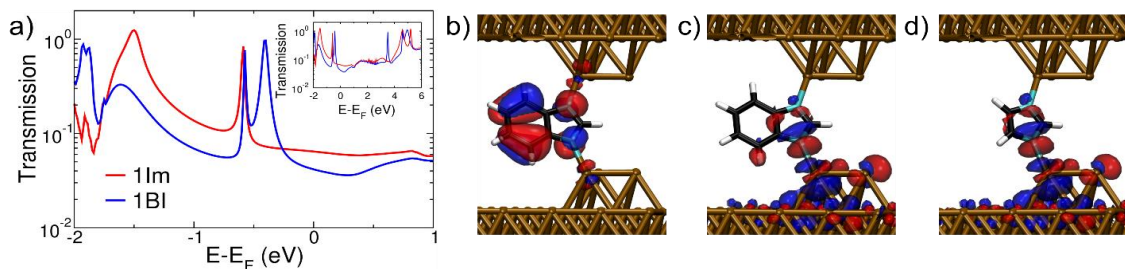


Figure 4-6. a) Transmission spectra of individual Im and BI molecular junctions. Real-space representation of the most conducting transmission eigenchannel at the center of the Brillouin zone for b) BI at -0.4 eV, c) BI at the Fermi energy, and d) Im at the Fermi energy.

Next, we calculate the conducting properties of Im and BI dimers (2Im and 2BI) to investigate the experimentally determined G2 values. We build junctions with molecular dimers and optimize the interface geometry, where no restrictions are imposed on the

geometry of the molecules. Figure 4-7a shows the computed transmission spectra of 2BI and 2Im in their lowest-energy configurations, where both BI and Im molecules are in a parallel orientation. As in the spectra of single BI and Im junctions, sharp resonances appear near the Fermi level in the $E-E_F < 0$ eV part of the spectrum. Their energy and width are different from those of Fig. 4-5a. This is caused by the enhanced interaction resulting from the small intermolecular distances. In Im dimers, the π resonance closest to the Fermi level is at -0.6 eV. In contrast, for BI dimer minimum energy geometry, the π resonance is found at -0.4 eV and is significantly broader, indicative of stronger electronic coupling, yet it does not determine zero-bias conductance.

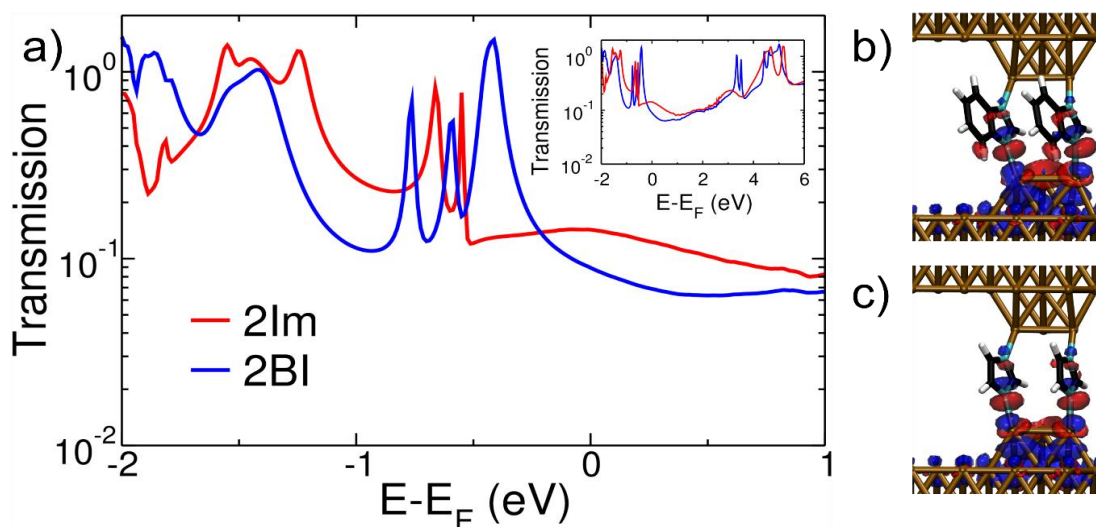


Figure 4-7. a) Transmission spectra of Im and BI dimers. Real-space representation of the most conducting transmission eigenchannel for b) BI dimers at the Fermi energy and c) Im dimers at the Fermi energy.

The most conducting orbitals at the Fermi level, calculated at the center of the Brillouin zone, are shown in Figures 4-7b (BI dimer) and 4-7c (Im dimer). In the geometry that each molecule adopts in the dimer assembly or alone at the junction, the molecular orbital nodal pattern is the same, indicating that the same σ states are responsible for low-

bias transport in all junctions. The calculated conductance values of 2Im and 2BI in their parallel configuration are $14.3 \times 10^{-2} G_0$ and $9.1 \times 10^{-2} G_0$, respectively, which yield G2/G1 ratios of 2.2 for both species when considering the parallel arrangement of molecules in the dimers. This ratio is close to the experimentally determined value of 2.3 for BI but is higher than the one for Im, 2.08. However, we found previously that non-parallel configurations were energetically accessible for Im and inaccessible in BI at room temperature. Therefore, we computed the conductance of the Im dimer for other values of θ compatible with an increase in energy of $\sim 2k_B T$ from the minimum, which all yield lower conductance values: $12.5 \times 10^{-2} G_0$ ($\theta = -10$ deg), $12.3 \times 10^{-2} G_0$ ($\theta = 10$ deg), and $12.3 \times 10^{-2} G_0$ ($\theta = 20$ deg). These geometries all result in G2/G1 ratios of ~ 1.9 . We conclude that when considering accessible conformations for Im dimers, the averaged G2/G1 ratio will be lower than that at $\theta = 0$ deg and closer to the measured value of $1.96 \times 10^{-2} G_0$ and $4.08 \times 10^{-2} G_0$. In BI dimers, on the other hand, the parallel orientation is strongly favored over other relative angles, and the conductivity and transmission calculation results of the parallel geometry are, therefore, representative.

To investigate the electronic structure origin of the increased conductance of the dimers, we compute the transmission of each molecule individually in the geometry that it adopts in the dimer. Starting from the structure of the dimer junction in the parallel conformation, we remove the coordinates of one molecule without changing the coordinates of the remaining atoms in the junction and compute the transmission. We determine that the calculated conductance values of the two BI (Im) molecules, frozen at the geometry adopted in the dimer, are $4.6 \times 10^{-2} G_0$ ($7.5 \times 10^{-2} G_0$) and $4.5 \times 10^{-2} G_0$ ($7.3 \times 10^{-2} G_0$), approximately 10% higher than the value obtained when the geometry of a single BI (Im) molecule is optimized, as shown in Table 4-4. When comparing isolated monomers and dimer assembly geometries for both BI and Im, we observed no significant changes in intramolecular parameters. However, the molecule's orientation relative to the tip, which differs in the dimer configurations, impacts the conductance. We investigate conductance of BI and Im monomers as a function of the torsional angle α between an Au-Au bond in the tip and the molecular plane (Figure 4-8), noting a clear correlation with monomer conductance. Upon comparing conductance values at α for monomer (-45° and -35° for BI and Im, respectively) and dimer configurations (approximately 5° for both), we find this difference largely accounts for the observed $\sim 10\%$ increase between monomer and dimer assemblies. The presence of π stacking thus restricts each molecule of the dimer to a conformation that is different and more conductive than the conformation it adopts when there is only one molecule in the junction.

	G_1 ($10^{-2}G_0$)	G_{2P} ($10^{-2}G_0$)	G_{2P}/G_1	G_{2AP} ($10^{-2}G_0$)	G_{2AP}/G_1
Im	6.4	14.3	2.22	14.9	2.31
		(7.3)		(7.3)	
		(7.1)		(7.5)	
BI	4.2	9.1	2.19	8.9	2.12
		(4.6)		(4.6)	
		(4.5)		(4.3)	

Table 4-4: Calculated conductance of BI and Im molecular junctions. For the dimers, conductance values of each of the individual molecules are given in parentheses.

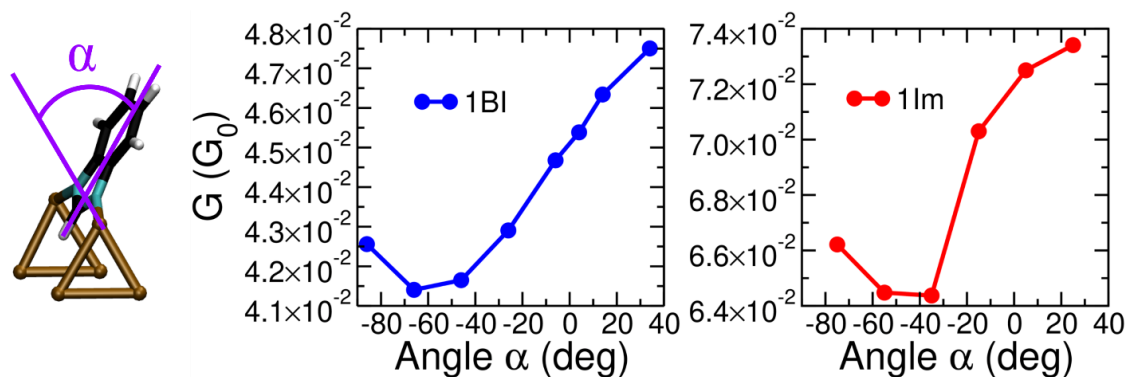


Figure 4-8. Torsional angle α between tip and molecule, and calculated conductance scans of BI and Im monomers as a function of α .

Guided by these insights into conductance enhancement mechanisms, we chose molecules that can self-assemble into dimer junctions with increased cooperativity due to intermolecular coupling as in BI but which retains the high monomer conductance of Im. To do this, we retain the Im core but substitute it with aliphatic or bulky aromatic moieties, increasing the surface area for intermolecular interactions. The histograms and structures of these Im derivatives, 2-phenylimidazole (2PhIm), 2-methylimidazole (2MeIm), are

shown in Figures 4-9a and 4-9. For comparison, we also measure the conductance of analogous BI derivatives, 2-phenylbenzimidazole (2PhBI), 2-methylbenzimidazole (2MeBI), shown in Figure 4-9b.

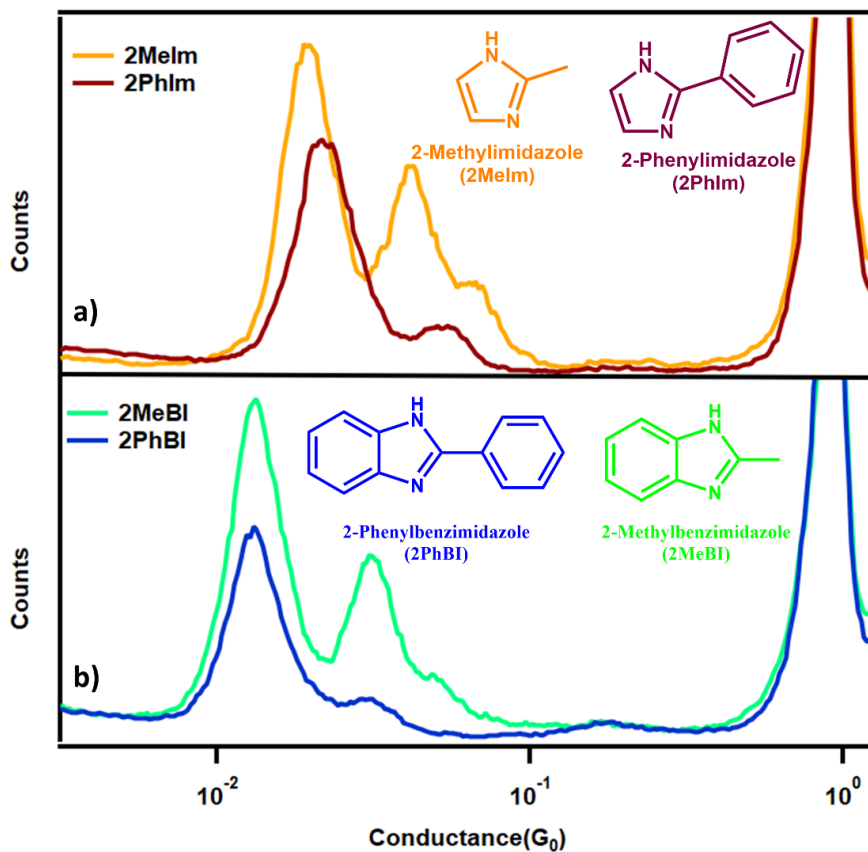


Figure 4-9. (a) Conductance histograms of 2-methylimidazole (2MeIm) and 2-phenylimidazole (2PhIm). Inset: Chemical structures of 2MeIm and 2PhIm. b) Conductance histograms of 2-phenylbenzimidazole (2PhBI) and 2-methylbenzimidazole (2MeBI). Inset: Chemical structures of 2PhBI and 2MeBI. Both conductance histograms are cut off at $10^{-3} G_0$ to focus on the HG region only.

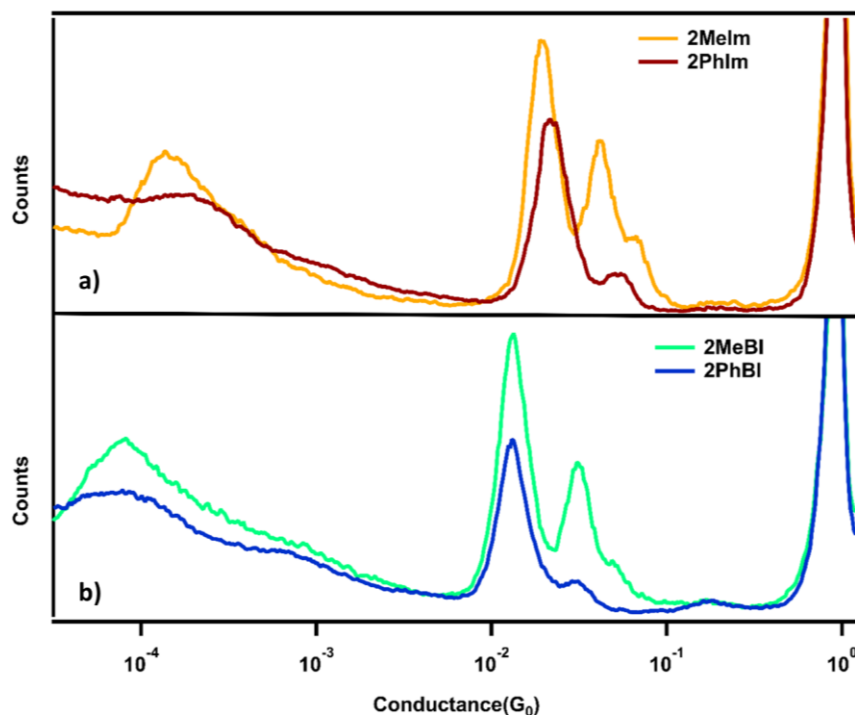


Figure 4-10. Full conductance histograms of a) 2-methylimidazole (2MeIm) and 2-phenylimidazole (2PhIm); b) 2-phenylbenzimidazole (2PhBI) and 2-methylbenzimidazole (2MeBI). All four molecules show low conductance features at $10^{-4} G_0$.

For all four molecules, the HG features of BI and Im are preserved, indicating successful junction formation through the nitrogen atoms as before. The steric bulk of the substituents decreases the amplitude of G2 in all molecules but does not abrogate the formation of dimers in the junction. The fits to the conductance of all BI derivatives are listed in the right column of Table 4-1. We observe that the G1 and G2 peak positions of 2PhBI and 2MeBI are nearly identical, and G2/G1 ratio for these molecules remains ~ 2.3 as in the BI result. We conclude that substituents do not significantly alter the ability of BI to π - π stack in the junction.

The conductance histograms and the fitted values in Figure 4-9 and Table 4-1 for Im substituted molecules reflect a different pattern. The 2MeIm and 2PhIm display a

G2/G1 ratio of 2.21 and 2.38, respectively, which is higher than Im, suggesting increased intermolecular stacking interaction in both substituted molecules. For 2MeIm, we note that the electron-donating nature of the methyl group increases the electron density on the π system of the Im core to promote van der Waals interactions and parallel binding in the junction. Notably, the measured dimer conductance enhancement in 2PhIm is greater than in 2MeIm and approaches the level in BI at G2/G1 \sim 2.3. For 2PhIm, we propose that the bulky phenyl substituent introduces an extensive π system to the Im core. This addition potentially facilitates the formation of the Im dimer in a parallel configuration, which, in turn, leads to a significant increase in dimer conductance.

To confirm this hypothesis, we perform calculations of 2PhIm dimers as a function of the relative angle (Figure 4-11) show that the computed energy profile is not as steep as in BI dimers, as the phenyl group can rotate relative to the imidazole units but is steeper than in Im dimers. The calculated G2/G1 ratio of 2PhIm dimers is 2.12. Though not as strong as in BI, substituting an aryl ligand in the 2 position, as in 2PhIm, enhances the cooperative binding of stacked molecules and increases the conductance of dimer junctions as in BI.

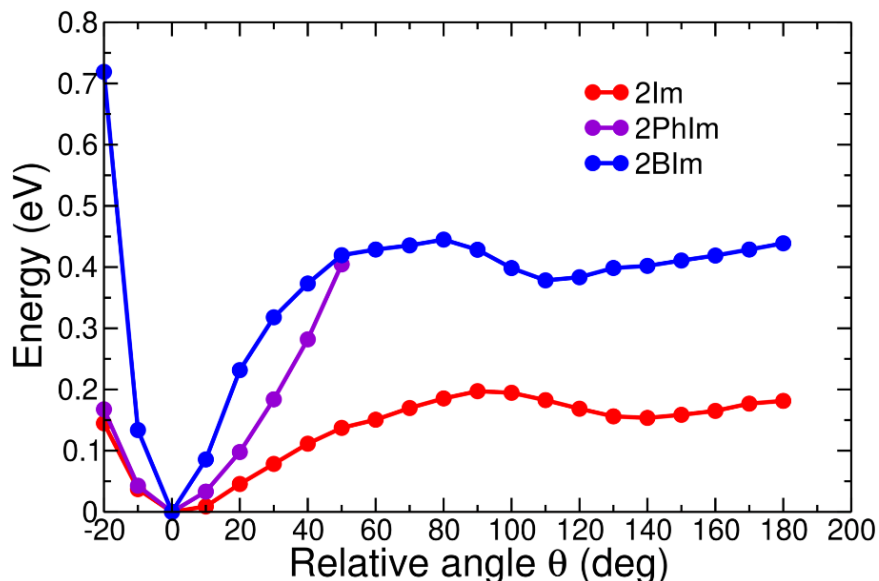


Figure 4-11: Energy profile of 2PhIm, calculated as in Figure 4-4, as a function of the relative angle between both Im units. 2Im and 2BI are reproduced from Figure 4-4 for comparison.

While the G_2/G_1 ratio is similar in 2PhIm and BI, the absolute conductance of the 2PhIm dimer is $4.94 \times 10^{-2} G_0$ compared to $2.64 \times 10^{-2} G_0$ for BI. We have succeeded in engineering a self-assembled molecular junction with nearly double the transmission of BI by leveraging a higher monomer conductance of the Im core and increased intermolecular coupling through aryl substitution, which promotes dimers with higher conductance per molecule unit.

4.5 Conclusion

To conclude, we demonstrate that π -stacked BI molecules bridge gold electrodes in parallel, resulting in multimer junctions with higher conductance per molecule than monomer BI junctions. We perform detailed theoretical studies to explore the origin of the enhanced conductance effect. Our calculations show that in parallel-stacked BI dimers, the intermolecular binding energy is greater than $20 k_B T$. In comparison, Im dimers have

higher conformational freedom to access a greater relative range of stacking angles between molecules. The preferential binding of BI molecules with aligned backbones leads to a conformation that is distinct from and more conductive than the conformation adopted by a single molecule in the junction and results in conductance enhancement in dimer junctions. We demonstrate the potential of harnessing cooperative binding for molecular electronics by choosing Im derivatives that have higher monomer conductance and promote π - π coupling to achieve further conductance enhancement in dimer junctions. This work identifies the potential for π - π driven self-assembly of more transparent molecular circuits and points to new ways of engineering molecular devices by tuning intermolecular interactions.

CHAPTER FIVE Atomically Precise Binding Conformations of Adenine and Its Variants on Gold Using Single Molecule Conductance Signatures

5.1 Preface

A version of this chapter has been published in the Journal of Chemical Physics, authored by Xiaoyun Pan, Cheng Qian, Amber Chow, Lu Wang, and Maria Kamenetska.²⁵ For this work, I carried out the scanning tunneling microscope-based break junction measurements and data analysis. I would like to express my gratitude to Cheng Qian and Lu Wang from Rutgers University for performing the computational work, Amber Chow for her assistance in data collection, and Maria Kamenetska for her guidance throughout the project.

5.2 Introduction

Detecting the binding conformation of biologically functional molecules, such as nucleobases, on noble metal surfaces is important for biosensor development, biotic-abiotic interface engineering, and electronic measurements of biomolecular conductivity.¹⁴³ Of the nucleobases, adenine in particular, has demonstrated the strongest binding affinity for gold.^{144,145} Developing an understanding of gold-adenine chemistry, such as molecule-surface interactions and reactivity, has the potential to advance the development of biosensors that effectively detect and distinguish biologically relevant adenine derivatives. Numerous studies on the adsorption orientation of adenine on noble metal surfaces have been performed in the last several decades. These include surface¹⁴⁶⁻¹⁴⁹ and tip-enhanced^{150,151} Raman scattering methods (SERS and TERS, respectively), and other surface-enhanced vibrational spectroscopic techniques.^{147,152,153} In addition, density

functional theory (DFT)^{146,148,154,155} has been widely used to simulate the surface interaction and determine the most probable absorption orientations of adenine on gold or silver surfaces. Collectively, these studies have established that the interaction of adenine with the gold surface occurs primarily through the lone pairs on the nitrogen atoms within the molecule. However, the presence of five potentially nucleophilic nitrogen atoms within adenine that can potentially compete for the binding to gold have made the determination of the most likely configuration of adenine on gold challenging.¹⁵⁶

Here, we tackle the long-standing question of the most likely binding orientation of adenine to gold using a combination of single adenine-gold junction conductance measurements and DFT calculations of the junction structures and transport. We also demonstrate how single molecule conductance measurements can be used to distinguish the binding of adenine from its biologically relevant variants, 6-methyladenine (M6A) and 2'-deoxyadenosine (2'-dAdo). In single molecule conductance measurements, donor-acceptor binding of the nitrogen lone pairs to the gold electrodes results in metal-molecule-metal junctions whose conductance can serve as a signature of molecule-metal binding geometry. Lone pairs on amine²¹, pyridine⁴⁵, and imidazole²⁶ molecular moieties have been shown to form stable and selective donor-acceptor bonds to undercoordinated gold atoms on metal electrodes. Single molecule conductance measurements of molecules containing two such linker atoms result in molecular junctions whose conductance signatures are exquisitely sensitive to the binding chemistry and orientation, allowing for a conductance-based mapping of binding geometry with atomic sensitivity to interface structure.²²

Adenine (Ade) is one of the purine nucleobases, containing two fused nitrogen-containing heterocycles. The five-membered imidazole ring consists of a pyridine and a pyrrole nitrogen, N7 and N9 respectively, which can tautomerize into either of the N7H and N9H forms shown in Figure 5-1.¹⁵⁷ The six-membered pyrimidine ring contains two pyridine-like nitrogen atoms, N1 and N3, and an exocyclic amino functional group with the nitrogen atom 6-NH₂. Within the DNA double helix, the pyrrole-like N9 is bound to the deoxyribose moiety, which then links to the phosphodiester backbone. The Watson-Crick pairing between adenine and thymine within the double helix occurs through the hydrogen bond between N1 (adenine) and N3 (thymine) and the 6-NH₂ and O of the pyrimidine rings. The molecule is entirely planar, which makes it compatible with the rung-on-a-ladder structure in the DNA.⁵³ The isosurface plots of the frontier orbital electron density in Figure 5-2 show that the electron rich areas on the molecule correspond to the π system as well as the nitrogen lone pairs. These features enable the base-pairing and the π - π stacking within the DNA structures.

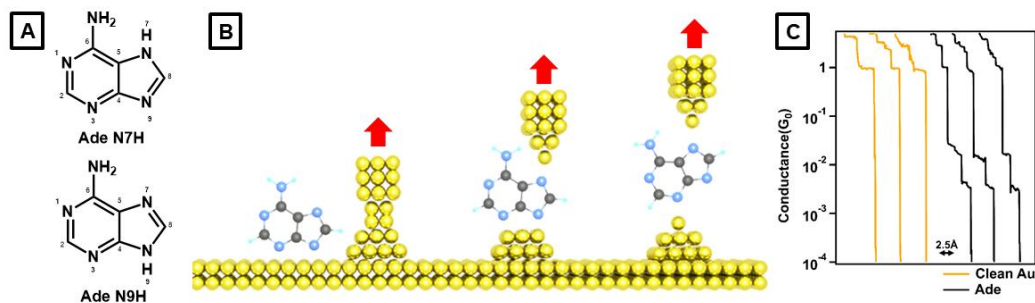
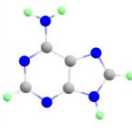
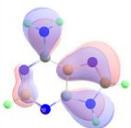
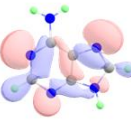
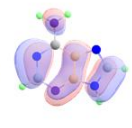
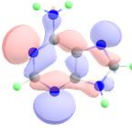
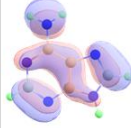
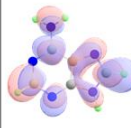
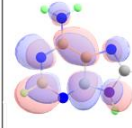
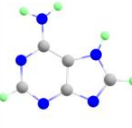
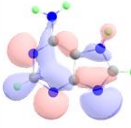

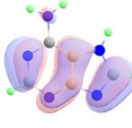
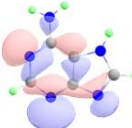

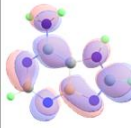
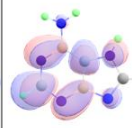


Figure 5-1. (A) Chemical structures of the two dominant adenine (Ade) tautomers with the non-H atoms numbered. (B) A cartoon of junction evolution while the two electrodes are pulled apart in the presence of Ade. (C) Sample conductance traces of clean gold (Au) junction (yellow) and Au-Ade-Au junction (black).

Ade N9H	HOMO-4	HOMO-3	HOMO-2	HOMO-1	HOMO	LUMO	LUMO+1
							
	-8.26eV	-7.92eV	-7.47eV	-7.01eV	-6.24 eV	-0.83eV	-0.07eV

Ade N7H	HOMO-4	HOMO-3	HOMO-2	HOMO-1	HOMO	LUMO	LUMO+1
							
	-8.34eV	-7.81eV	-7.37eV	-6.95eV	-6.45eV	-1.00eV	-0.16eV

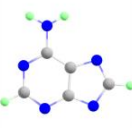
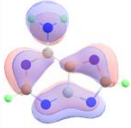
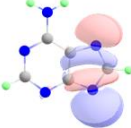
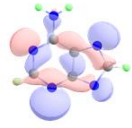
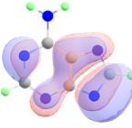


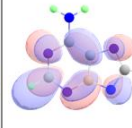
Ade anion	HOMO-4	HOMO-3	HOMO-2	HOMO-1	HOMO	LUMO	LUMO+1
							
	-3.33eV	-2.73eV	-2.45eV	-2.24eV	-1.53eV	3.73eV	4.38eV

Figure 5-2. DFT-calculated frontier molecular orbitals and their corresponding energies for the isolated N7H, N9H, and anionic forms of the Ade molecule in the gas phase.

Here, we use the Scanning Tunneling Microscope-based Break Junction (STMBJ) technique to measure the conductance of single Ade and Ade-derivative molecules on gold. By recording and analyzing statistically significant datasets of single molecule conductance measurements, we identify reproducible conductance signatures corresponding to distinct binding configurations of this molecule on metal electrodes.^{27,86} We compare conductance features of Ade and other structurally similar molecules that lack

one or more of the candidate binding sites of Ade. Through this systematic comparison, we assign individual molecular features to specific metal-molecule binding configurations. Our results indicate that Ade binds with gold electrodes through N7, N3, and N9, but not through N1 or 6-NH₂. We identify N9, for the first time, as a strong binding site in slightly basic conditions when the molecule becomes deprotonated. DFT calculations of the junction structures and charge transport support these conclusions and identify the importance of charge transfer in the binding strength of different conformations. More broadly, our combined experimental and theoretical approach provides a detailed picture of the most prevalent Ade-gold binding conformations and how they depend on the solvent environment and electrode geometry. We also demonstrate that conductance signatures unambiguously distinguish Ade from its biologically relevant derivatives, 6-methyladenine and 2'-deoxyadenosine, in single molecule junctions. These results establish single molecule conductance measurements as a powerful new tool for characterizing the atomic structure of metal-organic interfaces and for biosensing applications.

5.3 Additional calculation methods and polarizable continuum model

DFT calculations are performed to evaluate the interactions between Ade and the gold electrode. Since Ade is deprotonated under basic conditions, shown in Figure 5-3, we use the Ade anion with a deprotonated N9 atom in the calculations to account for the pH effect observed in the experiments. An Au₂₀ pyramid with or without an adatom on the tip is used to represent the gold electrode in the sharp or blunt configuration, respectively. The electronic structures of the systems are described using the PBE0 density functional¹⁵⁸, the D3 dispersion correction¹⁵⁹, and the 6-311G(d,p) basis set for Ade and the LanL2DZ basis

set for the Au atoms. All the calculations are performed using the conductor-like polarizable continuum model (PCM) with a dielectric constant of 78.4 to mimic the aqueous environment. Here we do not treat the water molecules explicitly due to the high computational costs associated with accurately describing the fluctuating solvation structures around the Ade anion using quantum chemistry methods, which is beyond the scope of the current work. Despite its lack of molecular details, we expect the PCM model to capture the solvation environment in the experimental measurements and give qualitatively correct predictions for the binding geometries and affinities.

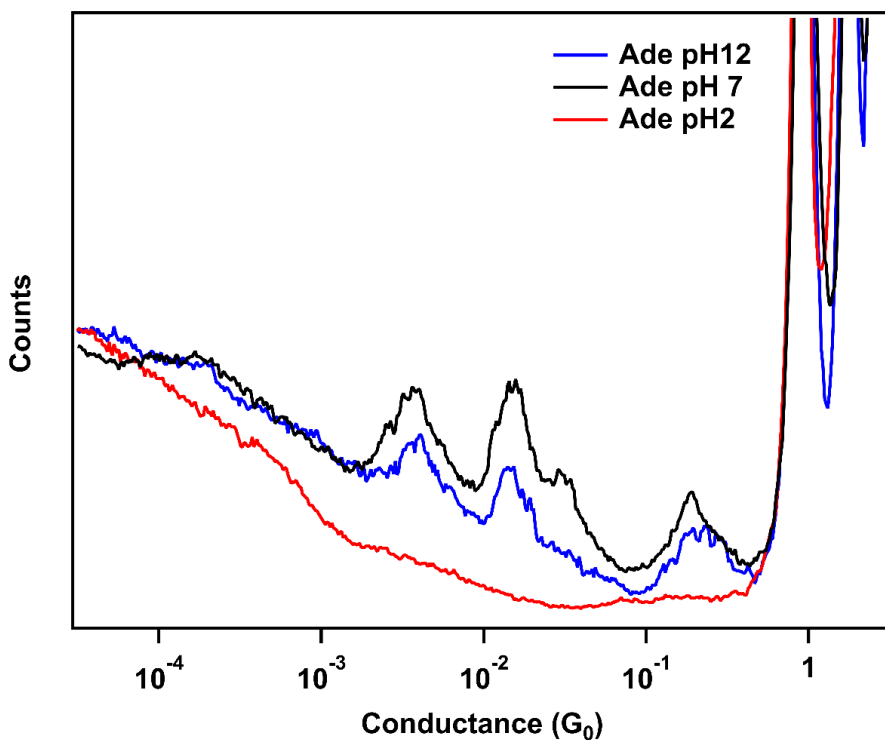


Figure 5-3: Conductance histograms of Ade measured at different pH levels: pH 2, pH 7, and pH 12.

We first compute the binding energies between Ade and the sharp or blunt gold tip using the Gaussian 16 program.¹⁶⁰ We optimize the structures of the sharp and blunt Au₂₀

pyramids in the aqueous environment and fix the positions of the gold atoms in the following analysis of the Ade-gold complexes. To construct the initial structures of the complexes, we place the Ade anion close to the Au₂₀ pyramid in the sharp or blunt configuration, with a distance of 2.5 Å between the N1, N3, N7 or N9 atom and the tip of the pyramid. After optimizing the geometry of each Ade-gold complex, we obtain the binding energy as $\Delta E_{INT}^{(s)} = E_{complex} - (E_{Ade} + E_{gold})$ where E_{Ade} and E_{gold} are the energies of the isolated Ade anion and Au₂₀ pyramid, respectively. Note that E_{Ade} is calculated from the geometry in the optimized Ade-gold complex so that $\Delta E_{INT}^{(s)}$ can be used in the energy decomposition analysis. To assess the validity of this approach, we repeat the calculations by optimizing the structure of the isolated Ade and find that the differences in the resulting binding energies are within 0.7 kcal/mol (Table 5-1). To ensure that the calculations reach the optimal complex geometries, we vary the initial structures by keeping the corresponding N-Au distance at 2.5 Å and rotating the Ade anions by 30°, 45° and 60°. In addition, we vary the initial positions of Ade around the blunt Au₂₀ pyramid by placing its N1, N3, N7 and N9 atoms at a distance of 2.5 Å away from 1, 2 or 3 Au atoms on the top surface of the pyramid. We then repeat the optimization processes and the reported $\Delta E_{INT}^{(s)}$ values are from the most stable Ade-gold complexes. We also carry out the same calculations in vacuum with counterpoise corrections¹⁶¹, and find that the relevant basis set superposition errors in the binding energy calculations are 3.3-3.9 kcal/mol. We then perform energy decomposition analysis on the optimized Ade-gold complexes using the ALMO-EDA(sol_v) method¹⁶² as implemented in the Q-Chem 5.3 software.¹⁶³

From DFT calculations, we obtain the binding energies between the Ade anion and the blunt Au₂₀ pyramid at different binding sites. $\Delta E_{INT}^{(s)}$ and ΔE_{INT}^{vacuum} are computed as the energy difference between the optimized Ade-gold complexes and the isolated fragments in the aqueous environment (using the PCM model) and in vacuum, respectively.

$$\Delta E_{INT} = E_{complex} - (E_{Ade} + E_{gold})$$

Here the structure of the blunt Au₂₀ pyramid is optimized in the corresponding solvation or vacuum condition and fixed in the Ade-gold complexes. For each binding site, E_{Ade} is calculated from the Ade structure in the complex to allow the decomposition of the total interaction energy in the following analysis. To validate this approach, we also compute the binding energy after optimizing the isolated Ade structure in the aqueous environment,

$$\Delta E_{INT,optAde}^{(s)} = E_{complex} - (E_{Ade,opt} + E_{gold})$$

As shown in Table 5-1, it is crucial to include the solvation environment in the binding energy calculations as $\Delta E_{INT}^{(s)}$ and ΔE_{INT}^{vacuum} differ by over 24 kcal/mol. It is also reasonable to calculate the binding energies without optimizing the isolated Ade structure considering that the differences between $\Delta E_{INT}^{(s)}$ and $\Delta E_{INT,optAde}^{(s)}$ are smaller than 0.7 kcal/mol in all cases.

Binding site	$\Delta E_{INT}^{(s)}$ (kcal/mol)	$\Delta E_{INT,optAde}^{(s)}$ (kcal/mol)	ΔE_{INT}^{vacuum} (kcal/mol)
N1	-26.7	-26.6	-56.4
N3	-40.7	-40.0	-67.1

N7	-30.6	-30.1	-55.2
N9	-40.7	-40.0	-74.8

Table 5-1. Binding energies between Ade and the blunt Au₂₀ pyramid in aqueous environment and in vacuum as obtained from DFT calculations.

5.4 Results and Discussion

A conductance histogram made without data selection from at least 6000 consecutively measured traces in the presence of Ade is shown in Figure 5-4B (green). We observe several clear peaks in this unfiltered histogram data that arise from several bridging configurations of Ade on gold. We hypothesize that the multiple amine and imine moieties on the molecule, specifically N1, N3, N7, N9 and the exocyclic amine 6-NH₂, allow for multiple distinct bridging configurations in the junction. The binding of several molecules in the junction in parallel can also lead to additional conductance peaks in the histogram.²⁶

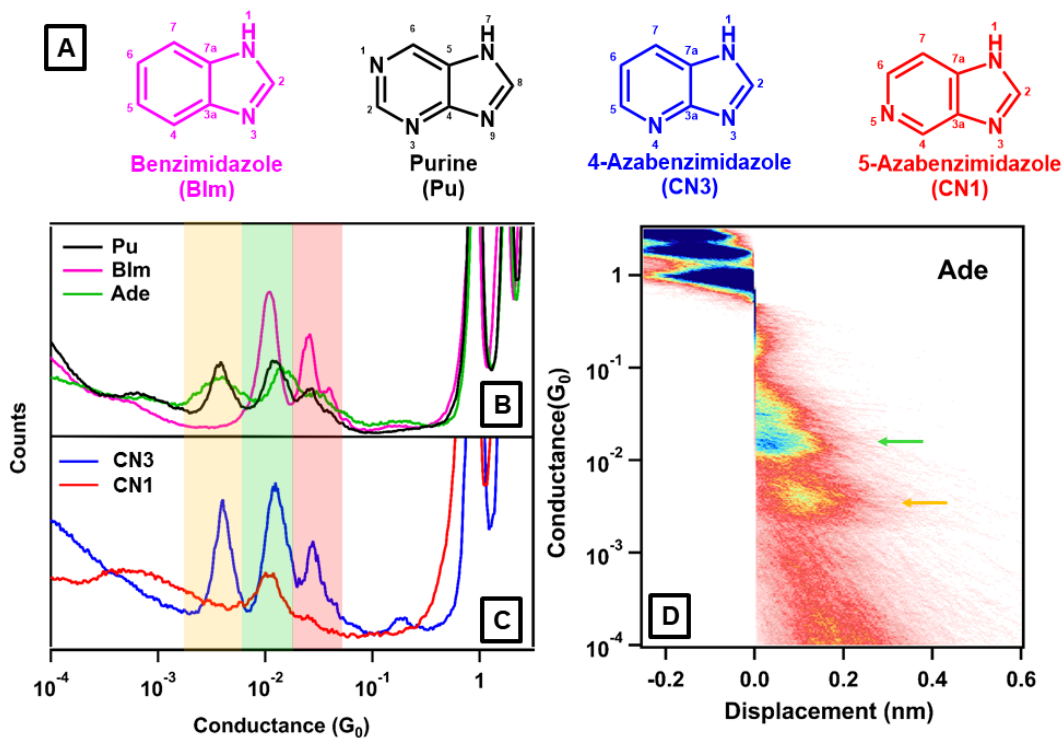


Figure 5-4. (A) Chemical structure of benzimidazole (BIm), purine (Pu), 4-azabenzimidazole (CN3) and 5-azabenzimidazole (CN1) with atomic positions numbered. (B) Conductance histograms of Ade, BIm, and Pu were binned from at least 6000 traces without any data selection. All molecules were measured using the dip-coating method from water as detailed in the SI. We identify at least two distinct conductance features labeled LG (yellow shading) and HG (green and red shading) in all or a subset of the molecules. (C) Conductance histograms of CN3 and CN1 compiled from at least 6000 traces without any data selection measured using the dip-coating method in pH 12. (D) Two-dimensional conductance-displacement histogram constructed from 7000 traces of Ade dip-coated from water with no data selection.

To disentangle the adsorption configurations corresponding to the distinct conductance signatures, we select molecules that are structurally similar to Ade but lack one or more of its candidate binding sites, and probe their conductance. As shown in Figure 5-4A, all the molecules are derivatives of benzimidazole (BIm, pink), which contains a fused system of imidazole and a six-membered benzene ring with no nitrogen lone pairs for binding to gold. Similar to Ade, in purine (Pu, black) the six-membered ring is a pyrimidine that contains two nitrogens. The 4- and 5-azabenzimidazole (CN3 and CN1, blue and red respectively) contain only one of the pyrimidine nitrogens at the 4 and 5 positions, respectively, which are analogous to the N1 and N3 atoms in Ade. As we vary the presence of the nitrogen binding sites by tuning the structure of the molecules, we compare the reproducible conductance features appearing in corresponding histograms.

	LG($10^{-2}G_0$)	HG1($10^{-2}G_0$)	HG2($10^{-2}G_0$)
BIm		1.13	2.62
Pu	0.36	1.16	2.48
Ade	0.34	1.31	2.84

CN3	0.40	1.25	2.74
CN1		0.98	

Table 5-2. The most probable conductance values of all molecules as obtained by fitting the linear conductance histogram with Gaussian fits. The standard errors of the Gaussian fitted values for all molecules are less than 1%.

We aim to distinguish the role of the imidazole, the pyrimidine ring, and the exocyclic amine on the binding of Ade to gold. First, we compare the conductance histograms of BIm, Pu, and Ade in Figure 5-4B. We observe that all three molecules display a conductance peak near $1 \times 10^{-2} G_0$. We label this peak as HG1 and determined the most likely HG1 conductance value by fitting a Gaussian to the linear histograms for each molecule as shown in Figure 5-5A. The resulting HG1 values are listed in Table 5-2. We compare the HG1 peak to the most likely conductance of imidazole, which is a common component of all the molecules in the sample and has a value of $1.9 \times 10^{-2} G_0$.²⁶ Imidazole bridges the tip-sample junction only in basic conditions when both nitrogens can be deprotonated and bind to gold.^{26,124}

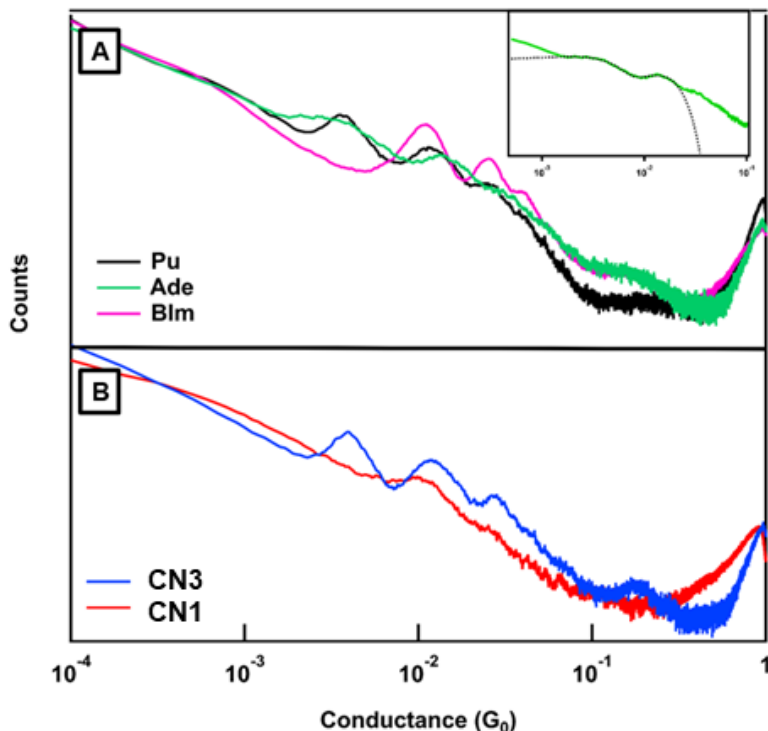


Figure 5-5. Linear binned (bin size = 10^{-4}) histograms of (A) Pu (black), Ade (green), BIm (pink), (B) CN3 (blue), and CN1 (red). Inset: Ade linear histogram (green) with two Gaussian fits (black dashed line) representing the HG1 and LG peaks.

We hypothesize that the observed conductance features of BIm are due to binding through imidazole nitrogen atoms and will occur at pH conditions above the pKa of BIm. We perform single molecule conductance measurements on BIm in a range of pH conditions and plot the resulting conductance histograms in Figures 5-6. We observe that the molecular signature intensities of BIm are significantly reduced in acidic environments, consistent with binding through imidazole. These experimental results allow us to assign the HG conductance features of BIm and, by analogy, to the other molecules in our sample including Ade, to a configuration where the molecule bridges the tip-sample gap through the imidazole moiety nitrogen atoms N7 and N9. Slight shifts in the HG1 conductance

values listed in Table 5-2 are consistent with the effect of substituents and chemical structure variations on orbital energies as previously documented in the literature.^{42,84,121}

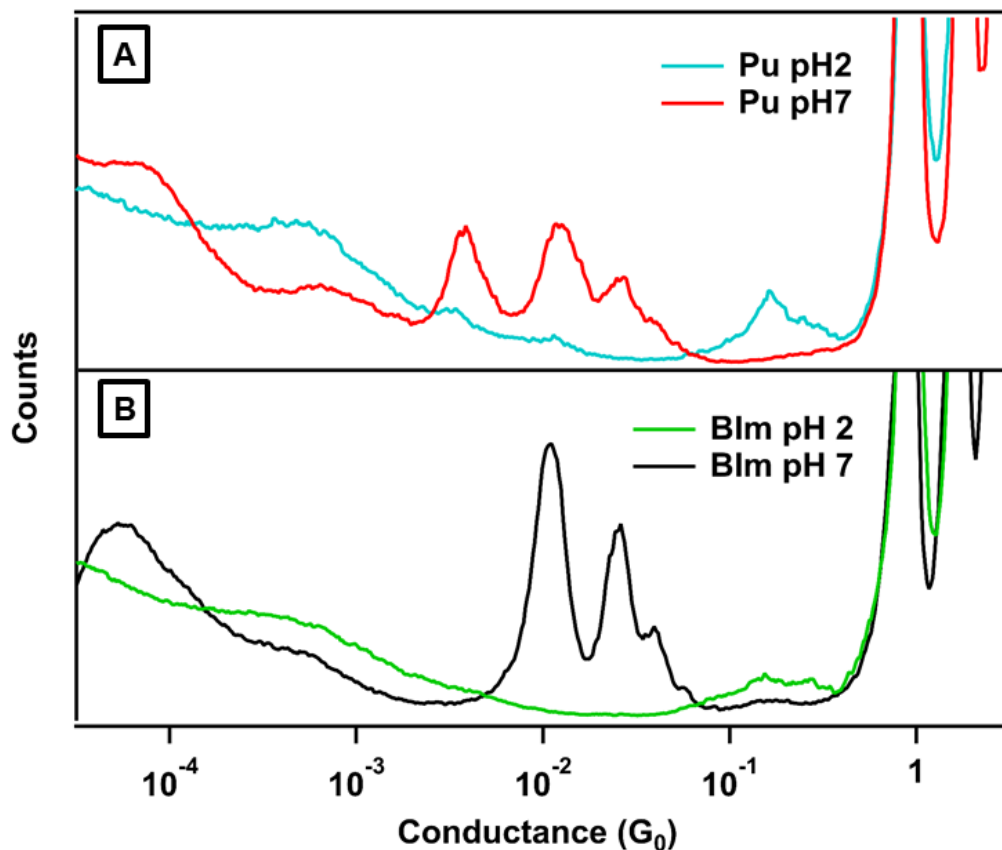


Figure 5-6. Conductance histograms of (A) Pu and (B) BIm measured at pH 2 and pH7.

All three molecules plotted in Figure 5-4B also show peaks at values of conductance higher than HG1 (green shading), which we term HG2 (red shading). The results of Gaussian fits to HG2 are listed in Table 5-2 and occur near an integer multiple of the main HG1 feature. As with imidazole, multiple molecules can bridge the junction in parallel to result in these secondary conductance features²⁶. We also note that BIm and Pu both display a higher junction yield as indicated by the higher amplitudes of HG signal than Ade. This result indicates that Ade bridges a smaller fraction of the junctions in the

HG configuration than the BIm and Pu variants, possibly because of the steric interference of the amine or the reduced charged density at the binding sites due to the electron withdrawing effects of the other pyridine-like nitrogens in Ade.^{21,84,164}

In addition to the HG peaks discussed above, Pu and Ade display a lower conductance signature, at $3.6 \times 10^{-3} G_0$, which we term the LG peak (yellow shading). We investigate the role of the exocyclic amine 6-NH₂ in Ade binding in the LG configuration. We note that Ade and Pu differ only in the presence or absence, respectively, of 6-NH₂. However, the conductance histograms of the two molecules share all the same conductance features. These results suggest that neither the HG nor the LG features observed in Ade are attributable to 6-NH₂ binding. To verify this result, we measure the conductance of 6-methylpurine (6MePu) where the exocyclic amine group is replaced by a methyl group. The resulting conductance histogram in Figure 5-7 shows the same number and position of conductance features, confirming that 6-NH₂ does not serve as an anchor point for Ade on gold electrodes. We conclude that the pyrimidine nitrogens N1 and/or N3, instead of the 6-NH₂ amine, must participate in binding to result in the LG configuration.

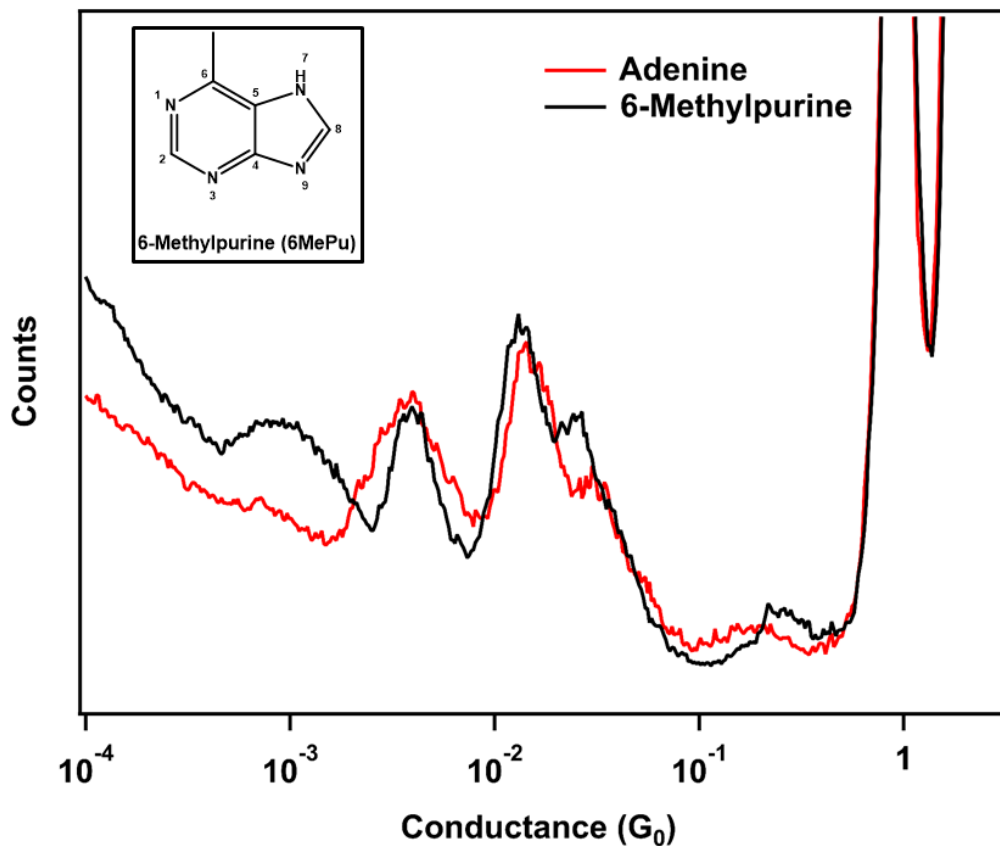


Figure 5-7. Conductance histograms of Ade and 6MePu. Inset: chemical structure of 6MePu.

The lack of amine binding in the junction is surprising in light of the established view in the literature that amine-linked molecules can affectively bridge metal-molecule junctions through a donor-acceptor bond between the electron lone-pair on the amine and an undercoordinated gold atom on the electrode.²² We probe the difference in the electronic structure between the 6-NH₂ atom in Ade and the amine linkers in 1,4 benzenediamine (BDA).^{89,116,165} We compare the DFT-calculated gas phase structure of Ade and BDA in Figure 5-8. The exocyclic N-C bond lengths of Ade and BDA are 1.35 Å and 1.40 Å respectively. Importantly, the dihedral angle between the two H-atoms on the amine, which is defined as the angle between the two C-N-H half planes, is 180° in Ade and 129°

in BDA. These differences suggest that the 6-NH₂ atom in Ade has sp^2 character, whereas it is predominantly sp^3 -hybridized in BDA. The planar configuration of 6-NH₂ in Ade results in a delocalized nitrogen lone pair which is unavailable for binding to gold.

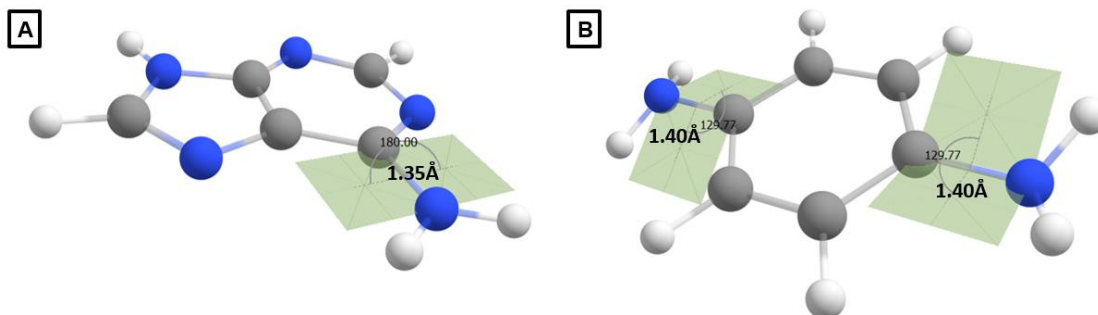


Figure 5-8. Definition of C-N-H-H dihedral angles and the exocyclic C-N bond lengths of (A) Ade and (B) 1,4 benzenediamine (BDA).

To distinguish which of the two sites, N1 or N3, on the pyrimidine results in the LG conductance configuration, we collect thousands of conductance traces in the presence of two Pu derivatives CN3 and CN1. The corresponding conductance histograms are shown in Figure 5-4C. Both molecules display HG conductance features, consistent with the shared imidazole moiety between all the molecules in the sample. However, CN3, but not CN1, binds in the LG conductance configuration. In addition, CN3 has higher HG1 and HG2 conductance signals than CN1, suggesting that the N3 nitrogen participates in anchoring the molecule in the HG configuration as well. We can conclude that the N3 site, rather than the N1 site, in Ade is necessary for the LG conductance signature and is directly involved in the molecule-gold binding.

To summarize our results so far, we list all the molecules in our sample and the most likely conductance values obtained from Gaussian fits to the linear histograms in

Table 5-2. Our results indicate that Ade has well-defined bridging geometries in the metal-molecule-metal junction and it binds on gold through the imidazole moieties, N7 and N9, and through pyrimidine N3. We cannot discount the possibility of simultaneous binding to all three sites.

To probe these junction geometries in more detail, we track how molecular conductance signatures evolve during junction stretching. Two-dimensional (2D) conductance histograms allow us to retain both the conductance and displacement information and correlate conductance to molecular binding configurations in the junction.²⁷ A 2D histogram for Ade, Figure 5-4D, indicates that the LG plateaus occur at longer elongation compared to the HG features. The HG features, on average, begin immediately following G_0 rupture and last for $\sim 1.5 \text{ \AA}$. The LG conductance plateaus appear after an additional $\sim 0.5 \text{ \AA}$ of stretching following gold point contact rupture and persist for $\sim 2 \text{ \AA}$ on average. We note that the N7-N9 and N7-N3 distances in Ade are 2.2 \AA and 3.6 \AA , respectively, as calculated by DFT methods. These results indicate that at shorter tip-sample distances, the conductance path across the molecular circuit occurs through the more proximal N7-N9 sites. The binding through the imidazole N7 and N9 atoms is stronger than a typical donor-acceptor bond due to the deprotonation of the imidazole moiety and added electrostatic interactions^{26,124} As the junction is stretched and the tip-sample distance widens, a reorganization of the molecule in the junction occurs to yield a binding configuration with a conducting pathway that includes N3, as illustrated in Figure 5-1B.

Complementary to the single-molecule conductance measurements, we carry out DFT calculations to investigate the electronic structures of the molecular junctions and the charge transfer process that affects the junction formation and conductance characteristics. Here we use the Au₂₀ pyramid structures both with and without an adatom on the tip to approximate the sharp and blunt electrodes, respectively. We find it essential to perform the calculations in an aqueous environment, which we represent using the PCM model, as it stabilizes the charged species in the molecular junctions and reduces the binding energies between the Ade anion and the gold electrode by over 24 kcal/mol as compared to those in vacuum (Table 5-1). Since it is generally accepted in the field that the blunt tips containing two or more apex atoms predominate in break junction single molecule measurements, especially in room temperature conditions when reorganization and flattening of the tips typically occurs immediately following rupture of the 1 G₀ contact,^{24,34,113,166–168} we will mainly discuss the calculation results using the blunt gold electrode in the following.

The optimal binding geometries of deprotonated Ade on the electrode are shown in Figure 5-9A-D, and the binding affinity of the different nitrogen sites follows the trend of N3 ≈ N9 > N7 > N1. In all cases, one or more nitrogen atoms in Ade adsorb on the electrode with a distance of 2.2 Å from the closest Au atoms. Interestingly, the blunt tip configuration provides a large contact surface for the binding and the constrained purine ring structure allows the N3 and N9 atoms to interact simultaneously with the gold electrode, leading to nearly identical optimal structures for the binding of Ade through the N3 and N9 sites and the strongest binding energies of -40.7 kcal/mol (Figure 5-9B and D). With a blunt tip, both N3 and N9 can interact with the top layer simultaneously, leading to

identical resulting structures. These energies are followed by those for the N7 site with an interaction energy of -30.6 kcal/mol between Ade and the Au₂₀ pyramid. Consistent with the experimental observations, binding through the N1 site is energetically least favorable, possibly because the exocyclic amino group in Ade hinders its contact with the gold electrode. We observe similar trend in the binding of Ade on the sharp Au₂₀ pyramid, as shown in Figure 5-10 and Table 5-3. However, the differences between the binding energies are much smaller than those in the blunt cases because only one of the N1, N3, N7 and N9 atoms of Ade can bind to the tip of the gold electrode in each configuration.

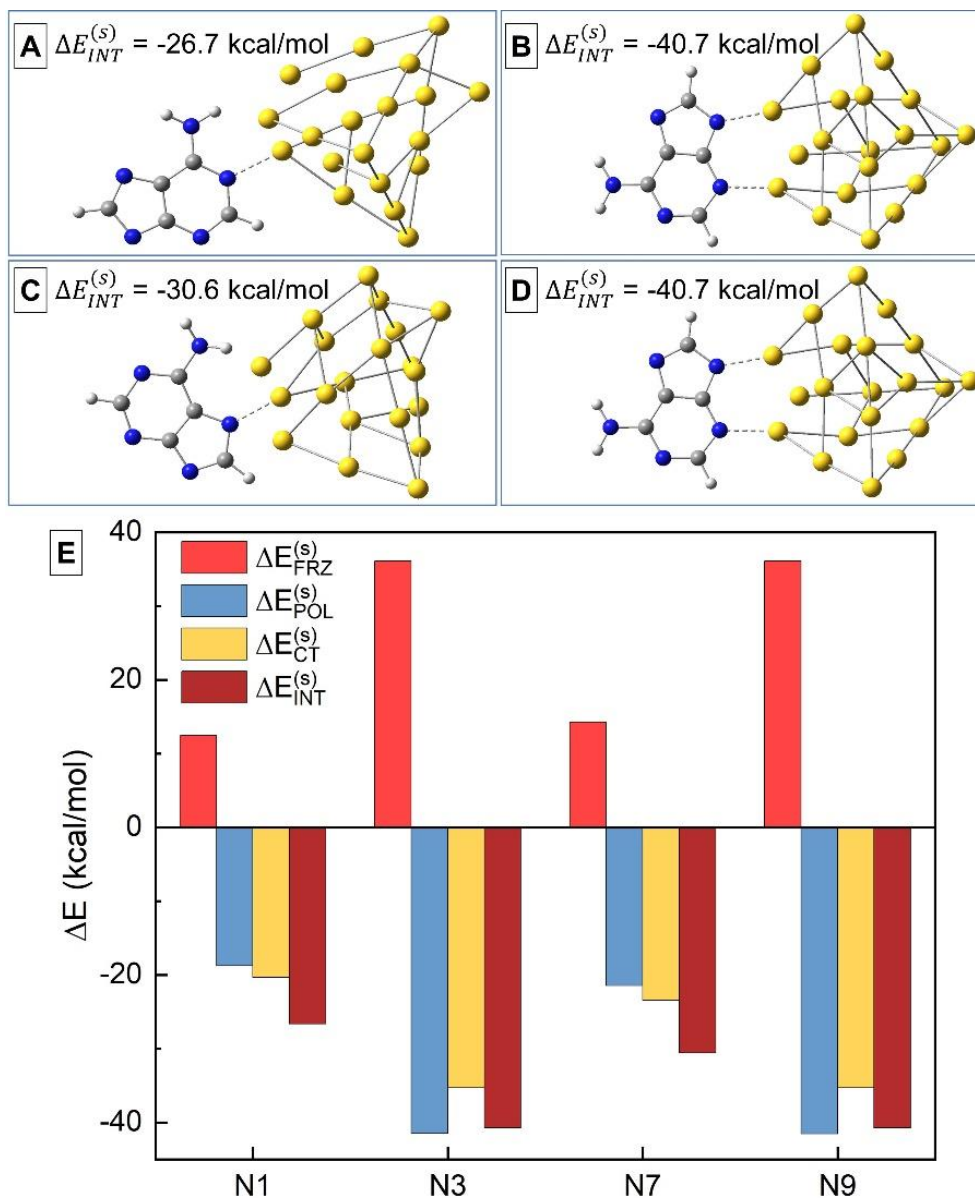


Figure 5-9. Optimized geometries for the binding of Ade on the blunt Au₂₀ pyramid at the (A) N1, (B) N3, (C) N7 and (D) N9 sites. Yellow, gray, blue and white represent the Au, C, N and H atoms, respectively. The dotted lines represent the interactions between the Au atoms and the closest N atoms on Ade. The total interaction energy $\Delta E_{INT}^{(s)}$ is also included for each binding configuration. (E) Decomposition of $\Delta E_{INT}^{(s)}$ into the frozen interaction energy ($\Delta E_{FRZ}^{(s)}$), polarization energy ($\Delta E_{POL}^{(s)}$) and charge transfer energy ($\Delta E_{CT}^{(s)}$).

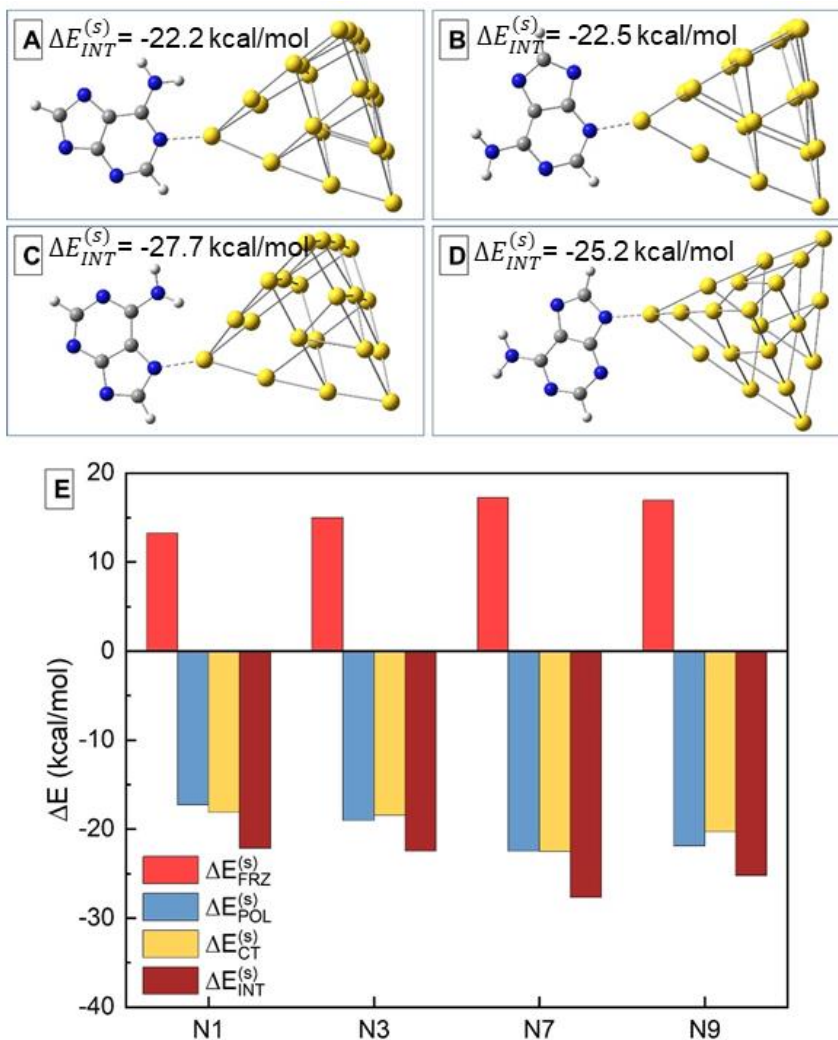


Figure 5-10. Optimized geometries for the binding of Ade on the sharp Au₂₀ pyramid at the (A) N1, (B) N3, (C) N7 and (D) N9 sites. Yellow, gray, blue and white represent the Au, C, N and H atoms, respectively. The dotted lines represent the interactions between the Au atoms and the closest N atoms in Ade. (E) Decomposition of the interaction energies between the Ade anion and the sharp Au₂₀ pyramid at different binding sites. For each binding site on Ade, the total interaction energy ($\Delta E_{INT}^{(s)}$) is partitioned into the frozen interaction energy ($\Delta E_{FRZ}^{(s)}$), polarization energy ($\Delta E_{POL}^{(s)}$) and charge transfer energy ($\Delta E_{CT}^{(s)}$).

Ade-blunt Au ₂₀ pyramid					Ade sharp Au ₂₀ pyramid			
Binding site	N1	N3	N7	N9	N1	N3	N7	N9
$\Delta E_{PAULI}^{(0)}$ (kcal/mol)	119.9	234.3	136.6	234.4	112.5	115.7	141.2	130.7
$\Delta E_{ELEC}^{(0)}$ (kcal/mol)	-96.9	-193.4	-108.5	-193.5	-93.9	-101.8	-119.7	-116.1
$\Delta E_{DISP}^{(0)}$ (kcal/mol)	-17.2	-23.4	-22.9	-23.4	-13.7	-11.7	-15.5	-12.1
ΔE_{SOL} (kcal/mol)	6.7	18.6	9.0	18.6	8.3	12.8	11.3	14.5
$\Delta E_{POL}^{(s)}$ (kcal/mol)	-18.8	-41.5	-21.4	-41.5	-17.3	-19.0	-22.5	-21.9
$\Delta E_{CT}^{(s)}$ (kcal/mol)	-20.4	-35.3	-23.4	-35.3	-18.1	-18.5	-22.5	-20.3
$\Delta E_{INT}^{(s)}$ (kcal/mol)	-26.7	-40.7	-30.6	-40.7	-22.2	-22.5	-27.7	-25.2

Table 5-3. Decomposition of the binding energies between Ade and the blunt and sharp Au₂₀ pyramid.

To uncover the origin of the observed trend that $N3 \approx N9 > N7 > N1$ in the binding affinities, we use the blunt Au₂₀ pyramid as an example and perform energy decomposition analysis for its interactions with Ade using the ALMO-EDA(solv) method.¹⁶² The total

interaction energy, $\Delta E_{INT}^{(s)}$, is partitioned into the frozen interaction, polarization and charge transfer energies,

$$\Delta E_{INT}^{(s)} = \Delta E_{FRZ}^{(s)} + \Delta E_{POL}^{(s)} + \Delta E_{CT}^{(s)}$$

The superscript (s) indicates that all the energies are calculated in a solution environment using the PCM model. The frozen interaction energy, $\Delta E_{FRZ}^{(s)}$, can be further partitioned into the Pauli repulsion (PAULI), permanent electrostatics (ELEC) and dispersion (DISP) contributions in vacuum and a solvation term (SOL),

$$\Delta E_{FRZ}^{(s)} = \Delta E_{PAULI}^{(0)} + \Delta E_{ELEC}^{(0)} + \Delta E_{DISP}^{(0)} + \Delta E_{SOL}.$$

The superscript (0) denotes the properties of the solute without the solute-solvent interactions, (although the orbitals are optimized with the solvation environment). The decomposition results for the Ade-gold complexes are listed in Table 5-3.

The frozen interaction energy, $\Delta E_{FRZ}^{(s)}$, describes the energy difference between the Ade-gold complex and the isolated Ade and Au₂₀ pyramid without relaxing their orbitals. It can be further partitioned into the Pauli repulsion, permanent electrostatics and dispersion contributions in vacuum and a solvation term.¹⁶² The effect of orbital relaxation is incorporated in the polarization and charge transfer contributions, $\Delta E_{POL}^{(s)}$ and $\Delta E_{CT}^{(s)}$. As shown in Figure 5-9E, the frozen interaction weakens the binding of Ade on the gold electrode, while polarization and charge transfer act to stabilize the bound complex. From Table 5-3, the positive $\Delta E_{FRZ}^{(s)}$ terms mainly come from the large Pauli repulsion (> 119 kcal/mol) between Ade and its nearby Au atoms in the pyramid, with a small contribution from the solute-solvent interactions that smear out the net charge on the Ade anion.

The attractive electrostatic and dispersion interactions cancel about 90% of these unfavorable interactions, leading to a $\Delta E_{FRZ}^{(s)}$ of ~ 14 kcal/mol for the N1 and N7 sites and 36 kcal/mol for the dual binding through the N3 and N9 sites. As the gold electrode approaches the Ade anion, their molecular orbitals overlap and charge reorganization occurs. Accordingly, the $\Delta E_{POL}^{(s)}$ and $\Delta E_{CT}^{(s)}$ terms are negative and are the main sources of stabilization in the binding process (Figure 5-9E). Among all the nitrogen sites, only the N3 and N9 atoms of Ade can interact simultaneously with the Au₂₀ pyramid, providing the most stable Ade-gold complex structures. Compared to N7, the N1 site gives the $\Delta E_{POL}^{(s)}$ and $\Delta E_{CT}^{(s)}$ components that are 2.6 and 3.0 kcal/mol higher in energy, respectively, making the binding through the N1 atom least favorable among all the nitrogen sites. Similar properties are observed for the sharp Au₂₀ pyramid (Figures 5-10 and Table 5-3). Therefore, the binding of Ade on the gold electrode results from a series of competing interactions, in which electrostatics, polarization and the purely quantum mechanical charge transfer and dispersion interactions play the major roles in determining the observed preference for the binding of different N atoms.

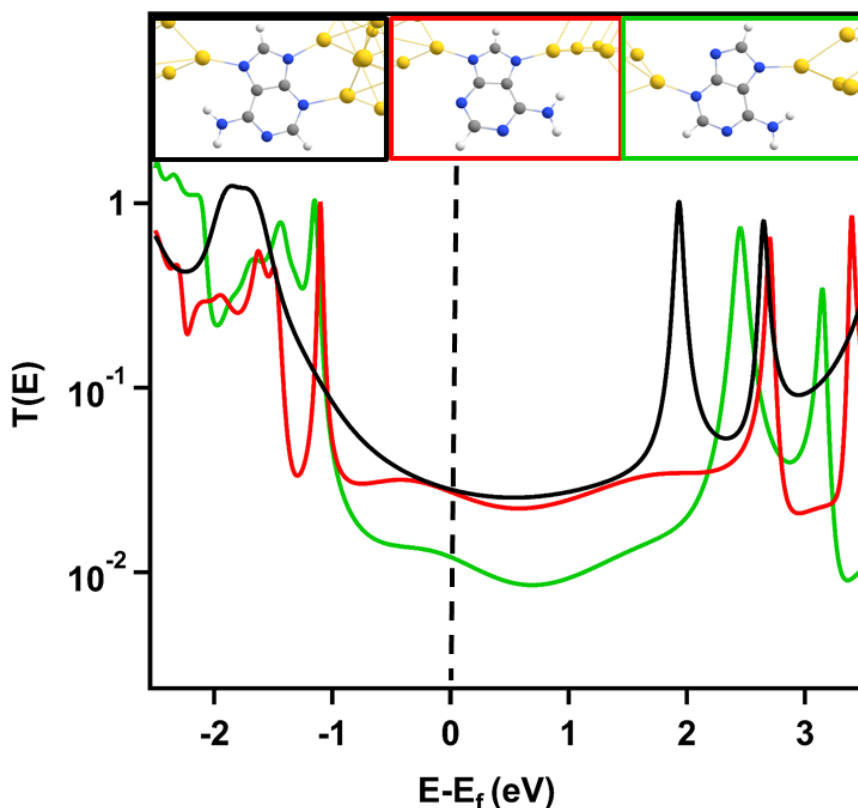


Figure 5-11. Relaxed structures of proposed binding geometries of N3/N7/N9 (black), N7/N9(red), and N3/N7(green) to Au18 pyramids and their corresponding transmission spectra.

We compare the conductance expected for Ade junctions arranged in three of the lowest energy binding configurations discussed above. Figure 5-11 (top inset) shows converged junction geometries where Ade bridges the gold pyramids through N7 on one side and either N9 (N7/N9, red), N3 (N3/N7, green) or both (N3/N7/N9, black) on the other. The calculated transmission curves plotted in Figure 5-11 for these junction configurations represent energy-dependent electron transport across the junction^{68,74}. We compare the calculated transmission values at the Fermi energy (0 on the energy x-axis) to our low-bias conductance measurements reported above as is standard practice in the

literature.^{44,120,169–171} We observe that the binding through N7/N9 and N3/N7/N9 results in very similar predicted conductances, which we cannot distinguish in our experiment. Since the N7/N9 geometry is bound less strongly than N3/N7/N9, we can assume the latter is more likely to occur in Ade during the HG configuration. The more stable anchoring through the three nitrogen atoms can also account for the higher probability of forming HG1 and HG2 junctions with CN3 than with CN1. However, the N3/N7 junction in Ade has a significantly lower conductance since the imidazole bridge through N9 is ruptured. The DFT-predicted conductance values for these two configurations are $2.8 \times 10^{-2} G_0$ and $1.2 \times 10^{-2} G_0$, which are several times higher than the measured results for the HG1 and LG peaks respectively. The degree of DFT overestimation of conductance we observe here is consistent with established trends in the literature.^{147,149} The Au-Au distance in the imidazole-bridging junctions N7/N9 and N3/N7/N9 is $\sim 6.2 \text{ \AA}$, which is 1 \AA shorter than in the N7/N3 junction. We conclude that the computationally identified, most favorable Ade binding configurations are consistent with the conductance and elongation experimental measurements presented here.

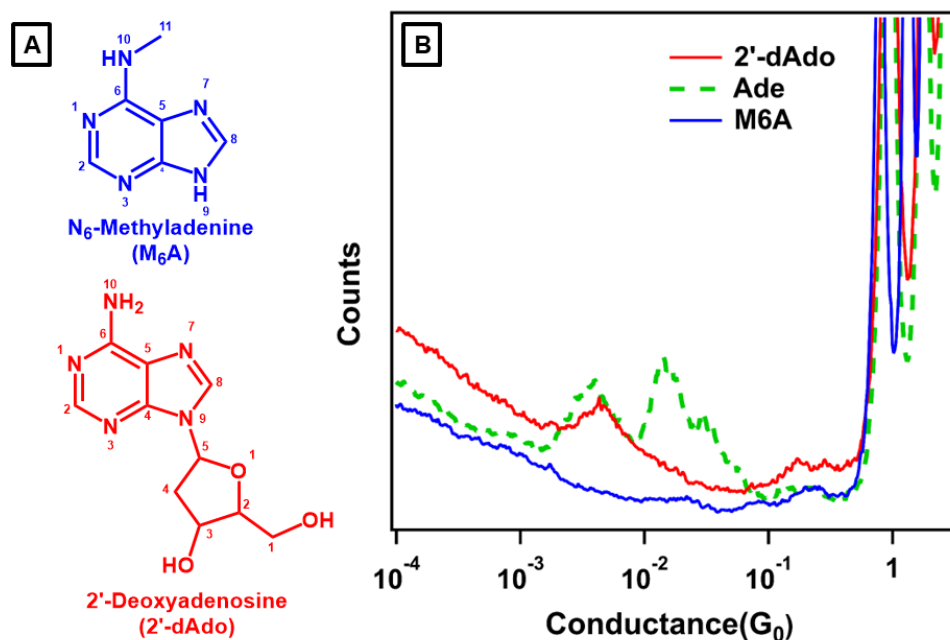


Figure 5-12. (A) Chemical structure of *N*₆-methyladenine (M6A) and 2'-deoxyadenosine (2'-dAdo) with the non-H atoms numbered. (B) Conductance histograms generated from at least 6000 traces collected in the presence of M6A (blue), 2'-dAdo (red), Ade (green, dashed line) deposited in neutral aqueous conditions.

Our results indicate that introducing changes to the structure of Ade through substituents that occlude sites N3, N7 or N9 will produce distinct changes in the conductance signatures. We propose that this sensitivity to molecular structure can be leveraged for biosensing applications to distinguish and detect the presence of Ade variants. To test this, we measure the conductance of M6A and 2'-dAdo, which are two biologically relevant Ade variants. M6A is a ubiquitous epigenetic modification and 2'-dAdo is a component of DNA and ATP with medicinal uses.¹⁷² The structures of both molecules are shown in Figure 5-12A. Based on how Ade binds to Au, we hypothesize that in M6A, the steric hindrance from the methyl group at 6-NH₂ group block the junction formation from the N7 site. As N7 is key to anchoring Ade to one of the electrodes in the

junction, we expect no conductance signatures in the presence of M6A. In 2'-dAdo, the N9 site is substituted so that imidazolate formation and binding is reduced, leaving only the N7/N3 binding pathway characterized by the LG conductance signature. The 1D conductance histograms constructed from at least 6000 traces measured in the presence of the variant molecules are plotted in Figure 5-12B. Consistent with our expectations, the M6A does not show any conductance signatures, whereas the 2'-dAdo displays a low amplitude peak at the LG position, suggesting that it binds in a small fraction of junctions through N3/N7. The conductance spectra of the three molecules in Figure 5-12B are clearly distinct. While more work is needed to fully characterize the binding of these and other adenine derivatives, our results serve as a proof of principle for using conductance signatures for sensing binding orientations and distinguishing biomolecules.

5.5 Conclusion

In conclusion, our combined single molecule conductance and DFT computation study offers new evidence for the binding configurations of Ade on gold and establishes single molecule conductance measurements as a useful tool for biomolecule detection. We find that Ade-Au binding is robust at pH above the pKa of N7 when the imidazole moiety on Ade is deprotonated. In these conditions, our experimental measurements reveal two distinct single molecule conductance regimes, high (HG) and low (LG). Through systematic comparison of conductance signatures of Ade and its derivatives, we can unambiguously assign these conductance signals to specific binding conformations. We determine that deprotonated Ade reproducibly coordinates with gold through N3, N7, and N9; not 6-NH₂ or N1. The exocyclic amine in Ade does not bind reproducibly to gold due

to the sp^2 character of the 6-NH₂ atom and the delocalized nature of the 6-NH₂ lone pair which discourages donor-acceptor bonding to gold. DFT calculations show that binding through N7, N9 and N3 are more favorable than N1 and it is possible to form multiple contacts when Ade interacts with the blunt tip configuration, which further stabilizes the molecular junction. The stabilizing contributions to the interaction energy from polarization and charge transfer, which occur upon binding of the deprotonated Ade to a reorganized gold electrode, are the smallest for the N1 pyridine site than for N3, N9 and N7. Calculated conductances through junctions bound through the most stable N3/N7/N9 and N3/N7 geometries are consistent with experimental measurements of the two conductance regimes. Our results provide new insights into the interaction of adenine with gold, which has been a subject of intense study and controversy. Additionally, we demonstrate how STMBJ can be used to study the interaction of biological molecules with noble metals and to detect variations in biomolecular structures by analyzing the conductance signals of single molecule-metal junctions. This work provides a blueprint for conductance-based sensing of biologically relevant molecules.

CHAPTER SIX Single Molecule Conductance Signature of Intramolecular Hydrogen Bonding in a Histamine Bound on Gold

6.1 Preface

The work presented in this chapter is based on a manuscript in progress, authored by Xiaoyun Pan, Katherine Matthews (Haverford College), Brent Lawson, and Maria Kamenetska. I was responsible for designing the experiments, performing theoretical calculations, visualizing the data, and drafting the initial manuscript. Katherine and I conducted the experiments and analyzed the data. Brent Lawson provided invaluable assistance in setting up the flicker noise analysis. I adapted the code from Brent Lawson for the theoretical calculations. The project was supervised by Masha Kamenetska, who also provided editorial assistance for the manuscript.

6.2 Introduction

Hydrogen bonding (H-bonding) is a fundamental interaction that plays a crucial role in the stability and function of biological molecules. In particular, it is widely recognized for promoting the formation of secondary and tertiary structures of biological macromolecules, such as DNA and amino acids.^{173,174} Intramolecular H-bonding can promote folded conformations and affect the electronic structure of molecules and chemical reactivity^{175,176}. For example, histamine (hist), a biogenic amine with a structure derived from the amino acid histidine, is believed to form intramolecular H-bonds under physiological conditions.^{177–179}

Hist plays a crucial role in numerous vital bodily functions, including immune response^{180,181} and neuro-signaling.^{182–184} Its structure, shown in Figure 6-1, consists of a

heterocyclic five-membered imidazole ring with an attached ethylamine side group. Hist can exist in two tautomeric forms, π and τ , where the hydrogen atom coordinates either N1 or N3, respectively, shown in Figure 6-1A. This unique structure can adopt multiple configurations in a pH-dependent manner^{175,179,185,186}, existing as a free base at high pH or a monocation at physiological pH, as shown in Figure 6-1B. Additionally, the ethylamine chain has significant degrees of freedom to freely twist and rotate¹⁷⁵, allowing hist to exist in several anti and gauche conformations. Upon twisting of the alkane chain, the imidazole moiety can interact with the amine through H-bonding.

Techniques such as Surface Enhanced Raman Spectroscopy (SERS)^{177,178}, Infrared (IR) Spectroscopy^{177,185}, Nuclear Magnetic Resonance (NMR) Spectroscopy^{187,188}, X-ray Diffraction analysis (XRD)^{189–192}, and Density Function Theory (DFT) calculations^{186,193–195} have been used to differentiate the various conformations of hist in solid state, solution, and gas phase circumstances. But in solution at room temperature, H-bonding is transient so that multiple conformations co-exist and can be challenging to differentiate using ensemble measurements.^{178,179}

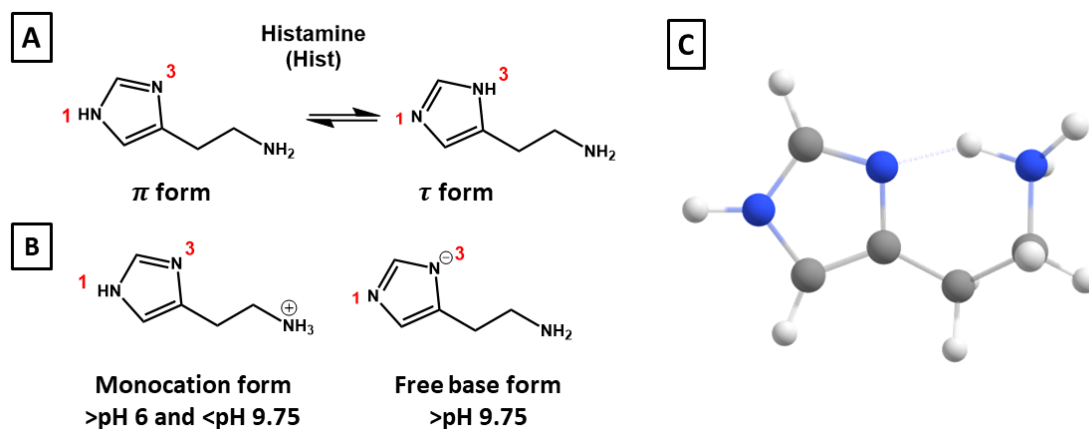


Figure 6-1. A. Chemical structures of histamine (hist) and its tautomeric forms; in the π (left) and τ (right) forms, the proton is at the N1 and N3 position, respectively. B. Monocation form of hist mostly exists at pH between 6 and 9.75; the free base form of hist mostly exists above pH 9.75. C. The most probable structure of monocationic hist in the gas phase, as predicted by DFT calculations (FHIaims, light basis set). A positive charge is added to the overall system to account for positively charged ammonium group.

We and others have shown that single molecule conductance measurements can be used to determine the binding conformation of biological molecules, such as adenine, on gold surfaces.²⁵ Adenine, like hist, contains the five-membered heterocyclic imidazole ring containing two nitrogen atoms. We found that the imidazole ring can bridge between two gold electrodes in basic conditions.²⁶ Separately, single molecule conductance measurements have also been performed through intermolecular H-bonding of biogenic molecules.^{54-59,196} In these studies, two molecules bridge the junction through an intermolecular donor-acceptor or H-bond interaction, and the conductance signature of the combined construct serves as a fingerprint of the H-bonded configuration^{55,57-59}

In this study, we utilize the Scanning Tunneling Microscope Break Junction (STMBJ) technique to detect and measure, for the first time, conductance through an intramolecular H-bond in a single hist molecule. We first investigate the conductance of hist under different pH and find that hist displays three conductance features but only under basic conditions. Next, we identify these features, labeled A, B, and C, as corresponding to distinct binding configurations and molecular conformations. We determine that feature A results from the molecule bridging the junction through the imidazole ring, while features B and C are signatures of the hist molecule spanning the gold electrodes through an imidazole linker on one side and the amine on the other. Using DFT calculation and flicker noise analysis, we unambiguously assign the higher conductance feature B to a H-

bonded hist conformation and feature C to a fully extended molecule where transport occurs through space and bond, respectively. This discovery is significant as we show we can identify an intramolecular H-bonded structure within a single molecule junction. Our results indicate that flicker noise analysis, which has previously been used for intermolecular π -bonded structures in the junction, can also identify H-bonded confirmations. By identifying an intramolecular H-bonded structure of the hist molecule we show that electron transport through H-bond is more efficient than through the alkane linker.

6.3 Results and Discussion

We use a home-built STMBJ setup as previously described in chapter 2.^{21,26,197} All molecules are dissolved in water to a concentration of ~ 5 mM, and the solution pH is adjusted as needed. As detailed in the supplemental information and prior work, we deposit molecules onto the gold-coated substrate using the dip-coating method onto the gold-coated substrate.^{25,26} A gold tip is repeatedly brought in and out of contact with the gold molecule-coated substrate to record molecular conductance. At each cycle, the molecule of interest can bridge the inter-electrode gap. We measure current across the junction under a constant bias, recording thousands of conductance versus displacement traces during junction elongation. Sample traces recorded in the presence of hist are shown in Figure 6-2. Conductance plateaus in the traces indicate the formation of stable junction conformations, which persist throughout junction pulling. Plateaus at integer multiples of $1 G_0$, the quantum of conductance, characterize junctions bridged by gold chains with integer multiples of gold atoms in the cross-section.³⁴ In contrast, plateaus at lower

conductance values can be attributed to molecule-bridged junctions.¹⁹⁷ All traces measured in the presence of a molecule are compiled into a conductance histogram without data selection. Conductance plateaus that occur regularly in single traces are peaks in conductance histograms and represent average conductance signatures of particular metal-molecule junction configurations.

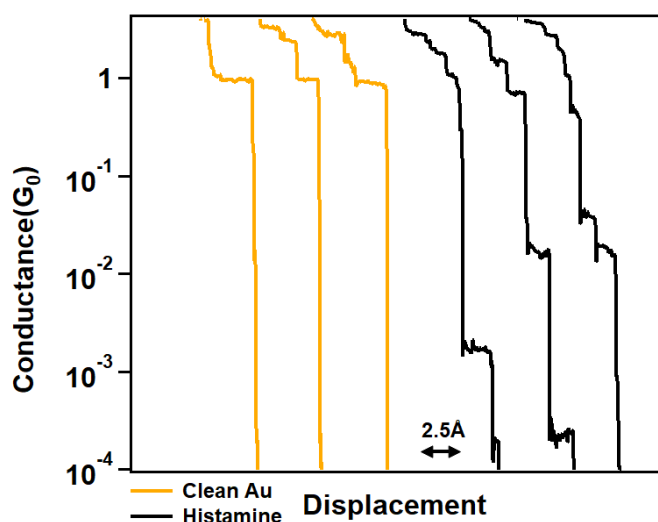


Figure 6-2. Sample conductance traces for clean Au only (yellow) and in the presence of the hist molecule (black).

We measure the conductance of hist at various pH conditions to probe the available conformations of the molecule on gold. Hist has two pKa values of 6.04 and 9.75,⁹¹ corresponding to the protonation of N3/N1 of imidazole and the amino side group, respectively. We have previously shown that imidazole can bridge the junction electrodes through N3 and N1 sites when deposited out of solution with a pH above the N3/N1 pKa, typically around neutral pH.²⁶ However, in hist, the amino side group is protonated at pH below 9.75, and the hist molecule is a monocation, as shown in Figure 6-1A. We conclude that between pH 6 and 9.75, the N3 lone pair can interact with the positively charged

ammonium, as shown in Figure 6-1C blocking the N3 binding sites from binding with the gold surface and preventing junction formation. At pH above 10, the molecule is anionic, and the amine and the imidazole nitrogen lone pairs may bind to the surface as shown in Figure 1C.

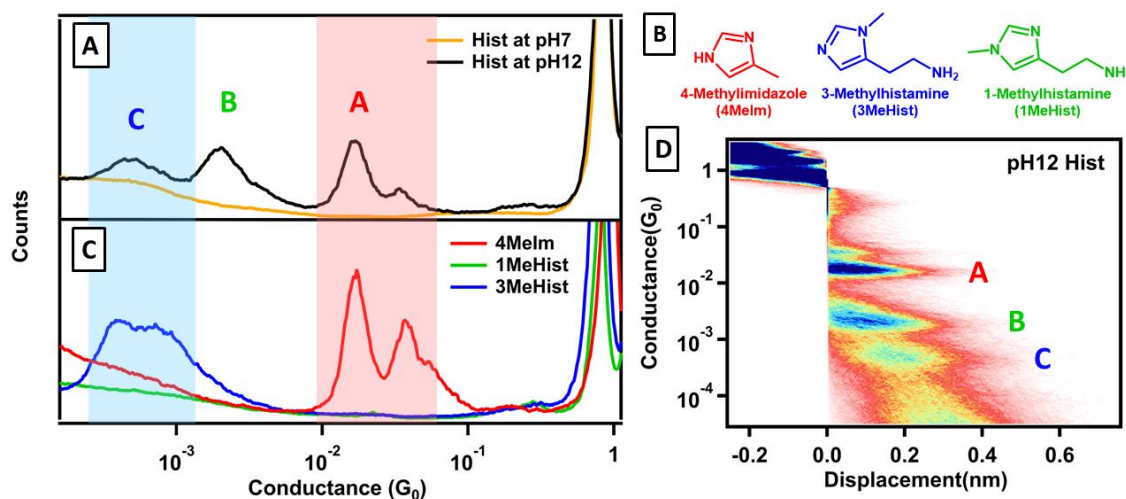


Figure 6-3. A. Conductance histograms of hist at pH 7 (yellow) and pH 12 (black). Conductance features of hist are labeled as A, B, and C, from highest to lowest conductance, respectively. B. Chemical structures of 4-Methylimidazole (4MeIm) in red, 3-Methylhistamine (3MeHist) in blue, and 1-Methylhistamine (1MeHist) in green. C. Conductance histograms of 4MeIm (red), 3MeHist (blue), and 1MeHist in pH 12 (green). Red and blue shaded regions represent conductance overlap of control molecules and hist. D. Two-dimensional histogram of hist at pH 12, with the features A, B, and C marked. All conductance histograms are constructed from at least 8000 traces without data selection.

The conductance histograms of at least 8000 consecutive conductance traces collected in the presence of hist in various pH conditions are shown in Figure 6-3A. Under neutral and acidic (not shown) conditions, we observe no conductance signals. This observation is consistent with the features of hist shown in Figure 6-1A for pH below pH 10 as discussed above. When the pH of the environment becomes sufficiently basic to deprotonate the ammonium side group above pH 10, distinct conductance peaks appear. We label the three unique molecular features of hist as A, B, and C, from highest to lowest

conductance, respectively, as shown in Figure 6-3A. We fit the 1D histogram to obtain the conductance values for these features, which are $1.6 \times 10^{-2} G_0$ for feature A, $1.7 \times 10^{-3} G_0$ for feature B, and $3 \times 10^{-4} G_0$ for feature C.

To assign these conductance features of hist in basic conditions to specific binding configurations, we perform measurements on control molecules, 4-Methylimidazole (4MeIm), 3-Methylhistamine (3MeHist), and 1-Methylhistamine (1MeHist), whose structures are shown in Figure 6-3B. Each molecule is missing one or two of the binding sites of hist, allowing us to identify signatures of particular binding geometries. We first measured 4MeIm, which contains only imidazole ring binding sites, and its conductance histogram is shown in Figure 6-3C in red. We observe that the feature A of hist, is identical to that of 4MeIm. Additionally, the higher conductance features observed at $3.2 \times 10^{-2} G_0$ is double the conductance of A, consistent with two hist conducting in parallel through the imidazole rings in the junction as was previously established.^{26,57,124} We conclude that feature A corresponds to configurations where both N1 and N3 of the imidazole ring are directly bridging with the gold electrodes, as reported previously.²⁶

Two additional features, B and C, do not align with the conductance signals of 4MeIm. A 2D histogram of 8000 traces plotted in Figure 6-3D shows conductance as a function of displacement. It reveals that hist features B and C are characterized by more extended conductance plateaus, suggesting that a longer molecular structure is bound in the junction to give rise to B and C conductance regimes. The amino side group is known to anchor molecules in junctions,^{21,39} so we hypothesize that both features B and C arise

from binding configurations that involve the amine anchoring the molecule to one of the electrodes.

We consider the possibility that the π and τ tautomeric forms of hist bind to one electrode with the NH₂ amine group and to the other electrode through either N3 or N1 to result in features B and C, respectively. We perform control measurements on 3MeIm and 1MeIm to mimic these π and τ tautomeric forms of hist, respectively. The conductance histograms are shown in Figure 6-3C. The green trace is 1MeHist and does not display any conductance features. This result allows us to rule out N3 as the anchor site for hist. In contrast, 3MeHist, plotted in blue, exhibits a broad conductance peak in the same conductance regime $\sim 3 \times 10^{-4} G_0$ as feature C of hist. We conclude that hist bridges the junction through N1 (Figure 6-1A) and the amine side group in two distinct molecular configurations, resulting in conductance regimes B and C. In the 2D histogram in Figure 6-3D, we observe that B plateaus are on average shorter than C plateaus. We also note that while C corresponds to a configuration that is accessible to both hist and 3MeHist, B is a configuration that is accessible to hist only. These observations suggest that features B and C correspond to a compacted gauche and an extended anti configuration of hist, respectively.¹⁷⁹ The amine side chain can interact with the lone pair on the N3 position in the *cis* configuration through an H-bond.

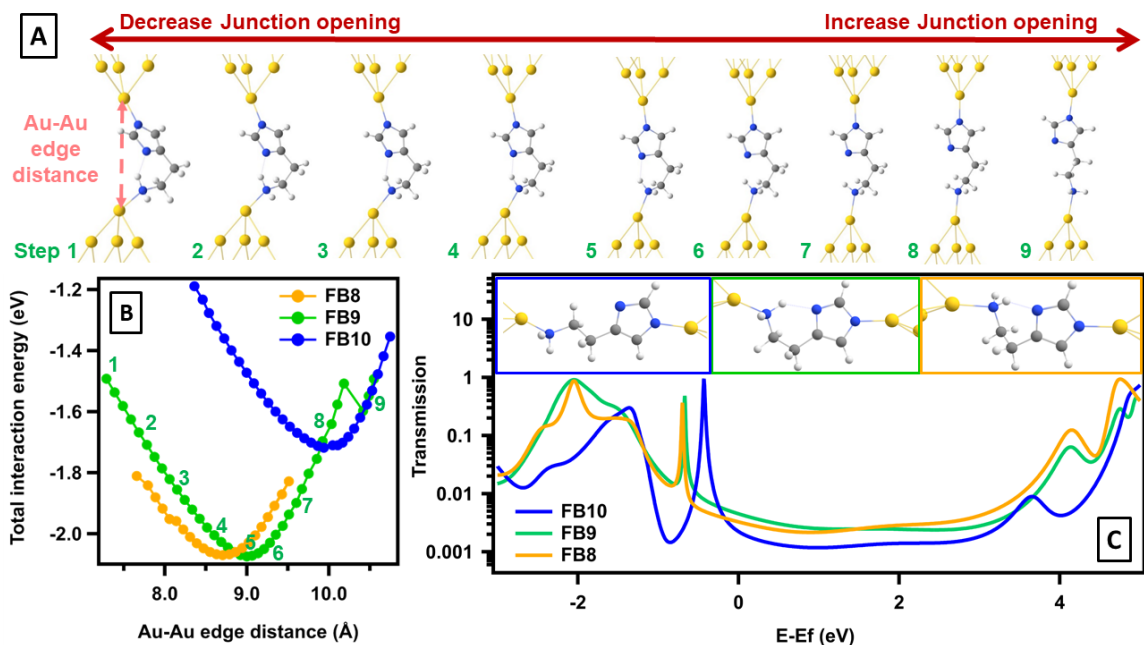


Figure 6-4. A. Relaxed DFT-calculated junction geometries of a hist molecular junction with two Au18 electrodes pulling or pushing along the Z direction in 0.15 Å steps. The Au-Au edge distance, highlighted using a pink arrow, represents the distance between the edges of two Au18 electrodes. Selected sample steps are from the FB9 structure to represent junction opening. B. The energy landscapes of the three identified stable geometries for hist in molecular junctions as a function of Au-Au electrode edge distance. The green numbering corresponds to the example steps graphically represented in Figure 6-4A. C. Transmission spectra of three local interaction energy maxima structures of free base hist, FB8 (yellow), FB9 (green), and FB10 (blue). Inset: Relaxed structures of FB8, FB9, and FB10. A top-down views of FB8 and FB9 are provided in Figure 6-5 to better visualize the differences between these two structures.

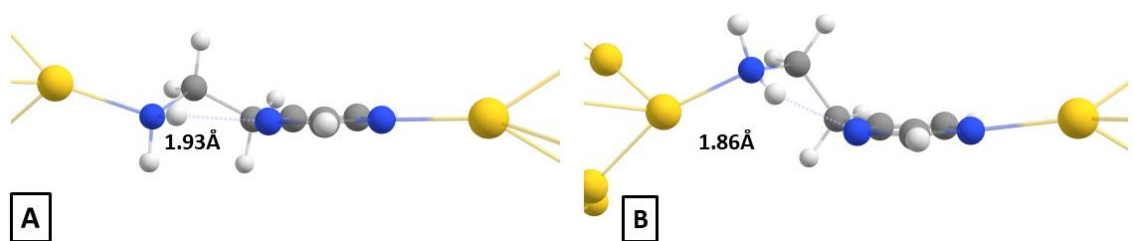


Figure 6-5: DFT calculated structures of A. FB8 and B. FB9, viewed from a different angle to illustrate the varying binding orientations of the ethylamine chain to the gold surface. The numbers on both figures represent the distances of the N α to N3 hydrogen bonds within each junction.

We carry out DFT-based transmission calculations to confirm this hypothesis using the FHIaims package with AITRANSS.^{68–70,74,198} We systematically search for the most stable binding geometries of the free base form of hist. This approach involves investigating the energy landscape of the ethylamine side chain conformations in the junction. First, we relax the gas-phase molecule and bind it through the experimentally determined N1 and amine lone pairs to the apex atoms of two gold pyramids containing 18 atoms (Au18) each.⁷² Using this starting geometry, we displace the electrodes relative to each other in steps of 0.15 Å, as shown in Figure 6-4A, to mimic junction opening and closing. We record the overall energy of the Au18-molecule-Au18 structure and calculate the total interaction energy, plotted in Figure 6-4B, as:

$$E_{total\ interaction\ energy} = E_{molecule\ and\ electrodes} - (E_{gas\ molecule} + E_{gas\ electrode})$$

To be consistent with experimental data shown in the 2D histogram in Figure 6-3D, we only consider junctions where the Au-Au distances are larger than 7 Å, which accounts for the snap-back distance and the junction displacement lengths of ~3 and ~4 Å for peaks B and C, respectively.

This systematic process identifies three stable junction conformations characterized by the interaction energy wells shown in Figure 6-4B.⁷² By fitting these potential energy surfaces, we identify the three local energy minima at gold-gold edge distances of ~8.7Å, ~9Å, and ~10Å. The corresponding geometries, FB8, FB9, and FB10, are shown in orange, green, and blue, respectively, in the top inset of Figure 6-4C. FB10 (not shown in 6-4A) corresponds to a fully extended trans conformation of the side chain. In contrast, the FB8 and FB9 geometries correspond to the shorter gauche molecular conformations with the

side chain curved towards the imidazole ring. Notably, we observe the formation of an intramolecular H-bond in both geometries, with the hydrogen in the amine group acting as a donor to the N3 lone pair hydrogen acceptor. The distance between the N3 and the H on the amine is 1.9Å in both structures, consistent with typical moderate strength H-bond lengths. The calculated energy difference between FB8 and FB9 is 0.0045 eV, far below thermal energy, so we consider these structures to be degenerate. On the other hand, the total interaction energy of FB10 is 0.35eV lower than that of FB9; this energy difference is comparable to moderate H-bonding strength, which ranges from 0.17eV to 0.6eV. This calculation suggests that the intramolecular H-bonded structures are significantly more stable than the extended trans structure in molecular junctions.

We then calculate the transmission spectra corresponding to each local energy minima,^{68,74} and show them in Figure 6-4C. FB10 has a calculated conductance at the Fermi energy of $2.2 \times 10^{-3} G_0$. FB8 and FB9 exhibit a higher calculated conductance at Fermi of $3.3 \times 10^{-3} G_0$ and $4.5 \times 10^{-3} G_0$, respectively. We note that DFT calculated conductance is consistently higher than experimental results, as reported by previous studies, and these predicted trends are consistent.^{44,120} Here, the DFT calculated conductance of FB8/9 and FB10 geometries are higher than the measured features B and C, respectively, but the trends match. In addition, DFT predicts that the lower conducting geometry FB10 is about $\sim 1\text{Å}$ longer than the higher conducting geometries FB8 and FB9. This difference is consistent with the comparison between experimentally observed features C and B, as shown in the 2D histogram in Figure 6-3D. Guided by this comparison,

we assign features C and B to the fully extended trans geometry and the shorter gauche H-bonded configurations, respectively.

Notably, the calculated conductance values for FB8 and FB9 are higher than for FB10. This result is unexpected, given the presence of gauche defects in FB8 and FB9. Previous studies have shown that this type of gauche defects can significantly reduce conductance through the alkane chain.^{199,200} However, here, the conductance of feature B is higher compared to an alkane of similar length, 1,4-butanediamine.^{27,67} This surprising result leads us to hypothesize that the conductance of feature B is primarily facilitated by the intramolecular H-bond instead of the ethylamine side chain.

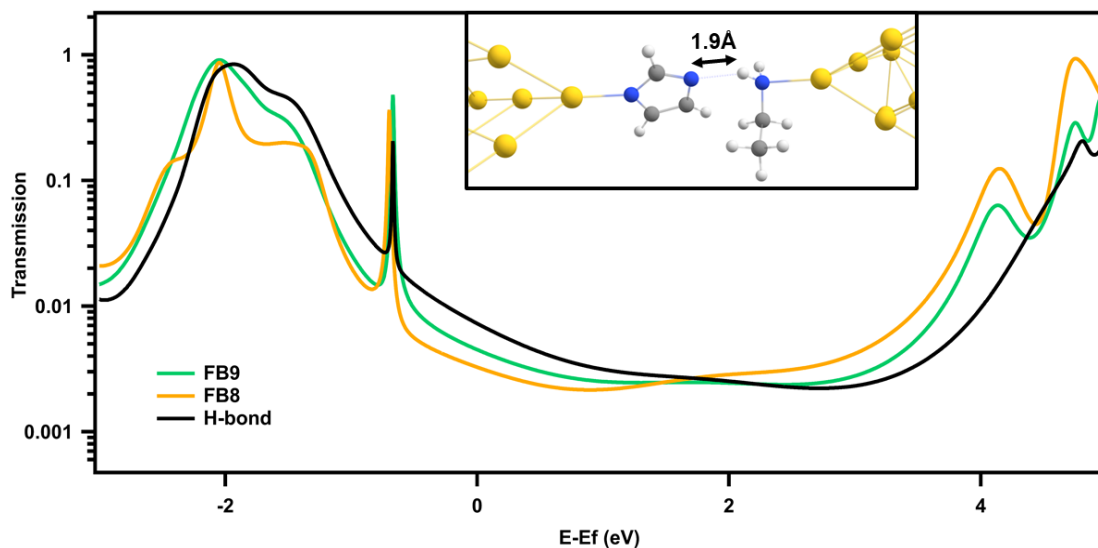


Figure 6-6. A comparative analysis of transmission spectra between a cleaved hist molecule conducting exclusively via a hydrogen bond and the models FB9 and FB8. Inset: the newly modified structure where the ethylamine chain is detached from the imidazole, and two new hydrogen atoms are attached to the structure to maintain structural integrity.

To validate the hypothesis that the intra-molecular H-bond serves as the main conducting channel, we calculate conductance through a modified structure in which the ethylamine chain is cut from the imidazole ring. We terminate with hydrogens where

necessary and allow only the carbon chain to relax while holding all other atoms, including the gold electrodes, the amine group, and imidazole, fixed to maintain the same H-bond length. Once we obtain the relaxed structure shown in the inset of Figure 6-6, we then compute the corresponding transmission spectrum. This modified structure maintains the same H-bonding and N-Au bond lengths as FB9 and has a similar calculated conductance to FB9, $7.2 \times 10^{-3} G_0$, as shown in Figure 6-6. We note that the only conducting channel in this geometry is through the H-bond as the saturated alkane chain moves away upon relaxation. This calculation further suggests that the intra-molecular H-bond provides the dominant conducting channel through the shorter hist molecular junctions, giving rise to feature B.

To validate this hypothesis experimentally, we perform flicker noise analysis which can distinguish between through space and bond interactions by detecting conductance fluctuations in the single-molecule junction.⁷⁶ To perform this analysis, we modify our standard pull out procedure, and pause junction elongation after a short initial pull of 2 nm. We then hold the electrodes fixed for 150 ms, as shown in Chapter 2. We repeat the procedure thousands of times and then select only those junctions which had a molecular conductance signature during the hold portion of the trace. We calculate the noise power and average conductance during the hold period for each single-molecule junction and analyze the correlation between these two parameters. Adak et al. demonstrated that the flicker noise power scales with the N^{th} power of the averaged conductance, G^N .⁷⁶ When the conductance occurs primarily through a covalent bond, the noise power scales with $N \sim 1$.

Instead, if the charge transport is mediated through space, such as in π stacking interactions, or hydrogen-bonding interactions, the noise power scales with $N \geq 1.4$.

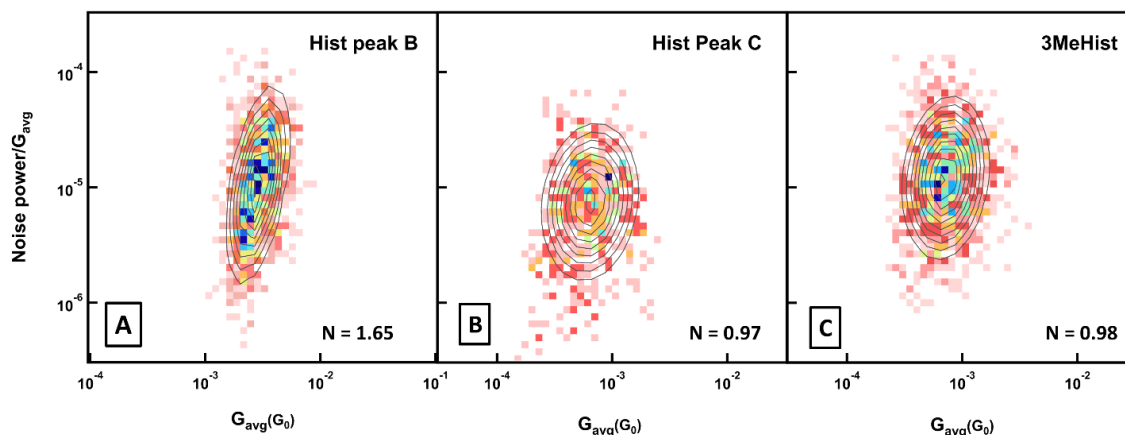


Figure 6-7. Two-dimensional histogram of normalized flicker noise power versus average conductance for A) hist feature B, B) hist feature C, and C) 3MeHist. The grey lines in each figure represent a two-dimensional Gaussian fit for each dataset.

Our flicker noise analysis results of features B and C are shown in Figures 6-7A and B, respectively. We plot the noise power normalized by the average conductance for each molecular plateau against the average conductance, as described by Adak et al.⁷⁶ We determine that feature B has a scaling coefficient of $N=1.65$, indicating substantial conductance fluctuations and suggesting through-space characteristics. On the other hand, the flicker noise analysis shows that feature C has through bond characteristics, with a scaling coefficient of $N=0.97$. In addition, we conduct a control flicker noise analysis experiment on 3MeHist, where the methyl group on N3 prevents H-bond formation. The observed scaling coefficient of $N=0.98$ suggests it shares the through-bond characteristics with feature C.

This flicker noise analysis aligns with our experimental data and DFT calculations, confirming that feature B corresponds to a through-space conducting pathway through the

intramolecular H-bond in the hist molecule. While most single-molecule conductance studies employ flicker noise analysis to examine π - π stacked or metal- π molecular junctions,⁷⁶ our results also indicate that H-bonding can be detected using this analysis. This is consistent with the fact that the typical moderate H-bond strength is comparable to metal- π and π - π interactions.^{201–203}

6.4 Conclusion

In conclusion, we use single-molecule conductance signals to investigate the pH-dependent binding configurations of hist on gold and discover and characterize conductance through intramolecular H-bonding in this molecule. Our measurements reveal that hist displays three unique conductance features, but only under basic conditions. Through careful and systematic comparative analysis using control molecules and the application of DFT calculations, we attribute these features to distinct binding configurations of hist. Most importantly, one of these geometries is a self-assembled intramolecular H-bonded structure of hist within a single-molecule junction, which displays higher conductance than that through the saturated ethylamine side chain. Lastly, we are able to differentiate between conductance signals originating from through covalent bond interactions and those from H-bonding interactions using flicker noise analysis. Our work not only elucidates the conductance characteristics of hist under different pH conditions and binding configurations, and identifies intermolecular H-bond as transparent to charge transfer.

BIBLIOGRAPHY

- (1) Willner, I.; Katz, E. *Bioelectronics: From Theory to Applications*; John Wiley & Sons, **2006**.
- (2) Jans, H.; Huo, Q. Gold Nanoparticle-Enabled Biological and Chemical Detection and Analysis. *Chemical Society Reviews* **2012**, *41* (7), 2849–2866. <https://doi.org/10.1039/C1CS15280G>.
- (3) Zeng, S.; Yong, K.-T.; Roy, I.; Dinh, X.-Q.; Yu, X.; Luan, F. A Review on Functionalized Gold Nanoparticles for Biosensing Applications. *Plasmonics* **2011**, *6* (3), 491–506. <https://doi.org/10.1007/s11468-011-9228-1>.
- (4) Saha, K.; Agasti, S. S.; Kim, C.; Li, X.; Rotello, V. M. Gold Nanoparticles in Chemical and Biological Sensing. *Chemical Reviews* **2012**, *112* (5), 2739–2779. <https://doi.org/10.1021/cr2001178>.
- (5) Walsh, T. R.; Knecht, M. R. Biointerface Structural Effects on the Properties and Applications of Bioinspired Peptide-Based Nanomaterials. *Chemical Reviews* **2017**, *117* (20), 12641–12704. <https://doi.org/10.1021/acs.chemrev.7b00139>.
- (6) Park, S. Y.; Lytton-Jean, A. K. R.; Lee, B.; Weigand, S.; Schatz, G. C.; Mirkin, C. A. DNA-Programmable Nanoparticle Crystallization. *Nature* **2008**, *451* (7178), 553–556. <https://doi.org/10.1038/nature06508>.
- (7) Young, K. L.; Ross, M. B.; Blaber, M. G.; Rycenga, M.; Jones, M. R.; Zhang, C.; Senesi, A. J.; Lee, B.; Schatz, G. C.; Mirkin, C. A. Using DNA to Design Plasmonic Metamaterials with Tunable Optical Properties. *Advanced Materials* **2014**, *26* (4), 653–659. <https://doi.org/10.1002/adma.201302938>.
- (8) Bayrak, T.; Helmi, S.; Ye, J.; Kauert, D.; Kelling, J.; Schönherr, T.; Weichelt, R.; Erbe, A.; Seidel, R. DNA-Mold Templated Assembly of Conductive Gold Nanowires. *Nano Letters* **2018**, *18* (3), 2116–2123. <https://doi.org/10.1021/acs.nanolett.8b00344>.
- (9) Dong, Y.; Yao, C.; Zhu, Y.; Yang, L.; Luo, D.; Yang, D. DNA Functional Materials Assembled from Branched DNA: Design, Synthesis, and Applications. *Chemical Reviews* **2020**, *120* (17), 9420–9481. <https://doi.org/10.1021/acs.chemrev.0c00294>.
- (10) Hu, Y.; Niemeyer, C. M. From DNA Nanotechnology to Material Systems Engineering. *Advanced Materials* **2019**, *31* (26), 1806294.
- (11) Seeman, N. C.; Sleiman, H. F. DNA Nanotechnology. *Nature Reviews Materials* **2017**, *3* (1), 17068. <https://doi.org/10.1038/natrevmats.2017.68>.

- (12) Breslauer, K. J.; Frank, R.; Blöcker, H.; Marky, L. A. Predicting DNA Duplex Stability from the Base Sequence. *Proceedings of the National Academy of Sciences* **1986**, *83* (11), 3746–3750.
- (13) Zwang, T. J.; Tse, E. C. M.; Barton, J. K. Sensing DNA through DNA Charge Transport. *ACS Chemical Biology* **2018**, *13* (7), 1799–1809. <https://doi.org/10.1021/acscchembio.8b00347>.
- (14) Genereux, J. C.; Barton, J. K. Mechanisms for DNA Charge Transport. *Chemical Reviews* **2010**, *110* (3), 1642–1662. <https://doi.org/10.1021/cr900228f>.
- (15) Arnold, A. R.; Grodick, M. A.; Barton, J. K. DNA Charge Transport: From Chemical Principles to the Cell. *Cell Chemical Biology* **2016**, *23* (1), 183–197. <https://doi.org/10.1016/j.chembiol.2015.11.010>.
- (16) Zhuravel, R.; Huang, H.; Polycarpou, G.; Polydorides, S.; Motamarri, P.; Katrivas, L.; Rotem, D.; Sperling, J.; Zotti, L. A.; Kotlyar, A. B.; Cuevas, J. C.; Gavini, V.; Skourtis, S. S.; Porath, D. Backbone Charge Transport in Double-Stranded DNA. *Nature Nanotechnology* **2020**, *15* (10), 836–840. <https://doi.org/10.1038/s41565-020-0741-2>.
- (17) Endres, R. G.; Cox, D. L.; Singh, R. R. P. Colloquium: The Quest for High-Conductance DNA. *Reviews of Modern Physics* **2004**, *76*(1), 195. <https://doi.org/10.1103/RevModPhys.76.195>.
- (18) Lewis, F. D.; Liu, X.; Liu, J.; Miller, S. E.; Hayes, R. T.; Wasielewski, M. R. Direct Measurement of Hole Transport Dynamics in DNA. *Nature* **2000**, *406* (6791), 51–53. <https://doi.org/10.1038/35017524>.
- (19) Wang, K. DNA-Based Single-Molecule Electronics: From Concept to Function. *Journal of Functional Biomaterials* **2018**, *9* (1). <https://doi.org/10.3390/jfb9010008>.
- (20) Xu, B.; Tao, N. J. Measurement of Single-Molecule Resistance by Repeated Formation of Molecular Junctions. *Science* **2003**, *301* (5637), 1221–1223. <https://doi.org/10.1126/science.1087481>.
- (21) Venkataraman, L.; Klare, J. E.; Tam, I. W.; Nuckolls, C.; Hybertsen, M. S.; Steigerwald, M. L. Single-Molecule Circuits with Well-Defined Molecular Conductance. *Nano Letters* **2006**, *6* (3), 458–462. <https://doi.org/10.1021/nl052373+>.
- (22) Su, T. A.; Neupane, M.; Steigerwald, M. L.; Venkataraman, L.; Nuckolls, C. Chemical Principles of Single-Molecule Electronics. *Nature Reviews Materials* **2016**, *1* (3), 1–15. <https://doi.org/10.1038/natrevmats.2016.2>.

- (23) Lv, S.-L.; Zeng, C.; Yu, Z.; Zheng, J.-F.; Wang, Y.-H.; Shao, Y.; Zhou, X.-S. Recent Advances in Single-Molecule Sensors Based on STM Break Junction Measurements. *Biosensors* **2022**, *12* (8), 565. <https://doi.org/10.3390/bios12080565>.
- (24) Quek, S. Y.; Kamenetska, M.; Steigerwald, M. L.; Choi, H. J.; Louie, S. G.; Hybertsen, M. S.; Neaton, J. B.; Venkataraman, L. Mechanically Controlled Binary Conductance Switching of a Single-Molecule Junction. *Nature Nanotechnology* **2009**, *4* (4), 230–234. <https://doi.org/10.1038/nnano.2009.10>.
- (25) Pan, X.; Qian, C.; Chow, A.; Wang, L.; Kamenetska, M. Atomically Precise Binding Conformations of Adenine and Its Variants on Gold Using Single Molecule Conductance Signatures. *Journal of Chemical Physics* **2022**, *157* (23). <https://doi.org/10.1063/5.0103642>.
- (26) Pan, X.; Lawson, B.; Rustad, A. M.; Kamenetska, M. pH-Activated Single Molecule Conductance and Binding Mechanism of Imidazole on Gold. *Nano Letters* **2020**, *20* (6), 4687–4692. <https://doi.org/10.1021/acs.nanolett.0c01710>.
- (27) Kamenetska, M.; Koentopp, M.; Whalley, A. C.; Park, Y. S.; Steigerwald, M. L.; Nuckolls, C.; Hybertsen, M. S.; Venkataraman, L. Formation and Evolution of Single-Molecule Junctions. *Physical Review Letters* **2009**, *102* (12), 2–5. <https://doi.org/10.1103/PhysRevLett.102.126803>.
- (28) Inkpen, M. S.; Liu, Z.; Li, H.; Campos, L. M.; Neaton, J. B.; Venkataraman, L. Non-Chemisorbed Gold–Sulfur Binding Prevails in Self-Assembled Monolayers. *Nature Chemistry* **2019**, *11* (4), 351–358. <https://doi.org/10.1038/s41557-019-0216-y>.
- (29) Capozzi, B.; Xia, J.; Adak, O.; Dell, E. J.; Liu, Z.-F.; Taylor, J. C.; Neaton, J. B.; Campos, L. M.; Venkataraman, L. Single-Molecule Diodes with High Rectification Ratios through Environmental Control. *Nature Nanotechnology* **2015**, *10* (6), 522–527. <https://doi.org/10.1038/nnano.2015.97>.
- (30) Kittel, C. Introduction to Solid State Physics, 8th Edition. *Wiley & Sons, New York, NY* **2004**.
- (31) Cuevas, J. C.; Scheer, E. *Molecular Electronics: An Introduction to Theory and Experiment*; World Scientific, **2010**.
- (32) Landauer, R. Electrical Resistance of Disordered One-Dimensional Lattices. *The Philosophical Magazine: A Journal of Theoretical Experimental and Applied Physics* **1970**, *21* (172), 863–867. <https://doi.org/10.1080/14786437008238472>.

- (33) Landauer, R. Spatial Variation of Currents and Fields Due to Localized Scatterers in Metallic Conduction. *IBM Journal of Research and Development* **1957**, *1* (3), 223–231. <https://doi.org/10.1147/rd.13.0223>.
- (34) Yanson, A. I.; Rubio Bollinger, G.; Van Den Brom, H. E.; Agraït, N.; Van Ruitenbeek, J. M. Formation and Manipulation of a Metallic Wire of Single Gold Atoms. *Nature* **1998**, *395* (6704), 783–785. <https://doi.org/10.1038/27405>.
- (35) Krans, J. M.; van Ruitenbeek, J. M.; Fisun, V. V.; Yanson, I. K.; de Jongh, L. J. The Signature of Conductance Quantization in Metallic Point Contacts. *Nature* **1995**, *375* (6534), 767–769. <https://doi.org/10.1038/375767a0>.
- (36) Gehring, P.; Thijssen, J. M.; van der Zant, H. S. J. Single-Molecule Quantum-Transport Phenomena in Break Junctions. *Nature Reviews Physics* **2019**, *1* (6), 381–396. <https://doi.org/10.1038/s42254-019-0055-1>.
- (37) Ishii, H.; Oji, H.; Ito, E.; Hayashi, N.; Yoshimura, D.; Seki, K. Energy Level Alignment and Band Bending at Model Interfaces of Organic Electroluminescent Devices. *Journal of Luminescence* **2000**, *87–89*, 61–65. [https://doi.org/https://doi.org/10.1016/S0022-2313\(99\)00230-6](https://doi.org/https://doi.org/10.1016/S0022-2313(99)00230-6).
- (38) Xin, N.; Guan, J.; Zhou, C.; Chen, X.; Gu, C.; Li, Y.; Ratner, M. A.; Nitzan, A.; Stoddart, J. F.; Guo, X. Concepts in the Design and Engineering of Single-Molecule Electronic Devices. *Nature Reviews Physics* **2019**, *1* (3), 211–230. <https://doi.org/10.1038/s42254-019-0022-x>.
- (39) Chen, F.; Li, X.; Hihath, J.; Huang, Z.; Tao, N. Effect of Anchoring Groups on Single-Molecule Conductance: Comparative Study of Thiol-, Amine-, and Carboxylic-Acid-Terminated Molecules. *Journal of the American Chemical Society* **2006**, *128* (49), 15874–15881. <https://doi.org/10.1021/ja065864k>.
- (40) Park, Y. S.; Whalley, A. C.; Kamenetska, M.; Steigerwald, M. L.; Hybertsen, M. S.; Nuckolls, C.; Venkataraman, L. Contact Chemistry and Single-Molecule Conductance: A Comparison of Phosphines, Methyl Sulfides, and Amines. *Journal of the American Chemical Society* **2007**, *129* (51), 15768–15769.
- (41) Hammett, L. P. The Effect of Structure upon the Reactions of Organic Compounds. Benzene Derivatives. *Journal of the American Chemical Society* **1937**, *59* (1), 96–103.
- (42) Venkataraman, L.; Park, Y. S.; Nuckolls, A. C. W. C.; Hybertsen, M. S.; Steigerwald, M. L. Electronics and Chemistry: Varying Single Molecule Junction Conductance Using Chemical Substituents. *Nano Letters* **2007**, *7* (2), 502–506. <https://doi.org/10.1021/nl062923j>.

- (43) Venkataraman, L.; Klare, J. E.; Tam, I. W.; Nuckolls, C.; Hybertsen, M. S.; Steigerwald, M. L. Single-Molecule Circuits with Well-Defined Molecular Conductance. *Nano Letters* **2006**, *6* (3), 458–462.
- (44) Quek, S. Y.; Venkataraman, L.; Choi, H. J.; Louie, S. G.; Hybertsen, M. S.; Neaton, J. B. Amine - Gold Linked Single-Molecule Circuits: Experiment and Theory. *Nano Letters* **2007**, *7* (11), 3477–3482. <https://doi.org/10.1021/nl072058i>.
- (45) Kamenetska, M.; Quek, S. Y.; Whalley, A. C.; Steigerwald, M. L.; Choi, H. J.; Louie, S. G.; Nuckolls, C.; Hybertsen, M. S.; Neaton, J. B.; Venkataraman, L. Conductance and Geometry of Pyridine-Linked Single-Molecule Junctions. *Journal of the American Chemical Society* **2010**, *132* (19), 6817–6821. <https://doi.org/10.1021/ja1015348>.
- (46) Schneebeli, S. T.; Kamenetska, M.; Cheng, Z.; Skouta, R.; Friesner, R. A.; Venkataraman, L.; Breslow, R. Single-Molecule Conductance through Multiple π - π -Stacked Benzene Rings Determined with Direct Electrode-to-Benzene Ring Connections. *Journal of the American Chemical Society* **2011**, *133* (7), 2136–2139. <https://doi.org/10.1021/ja111320n>.
- (47) Vazquez, H.; Skouta, R.; Schneebeli, S.; Kamenetska, M.; Breslow, R.; Venkataraman, L.; Hybertsen, M. S. Probing the Conductance Superposition Law in Single-Molecule Circuits with Parallel Paths. *Nature Nanotechnology* **2012**, *7* (10), 663–667. <https://doi.org/10.1038/nnano.2012.147>.
- (48) Wu, S.; González, M. T.; Huber, R.; Grunder, S.; Mayor, M.; Schönenberger, C.; Calame, M. Molecular Junctions Based on Aromatic Coupling. *Nature Nanotechnology* **2008**, *3* (9), 569–574. <https://doi.org/10.1038/nnano.2008.237>.
- (49) Martín, S.; Grace, I.; Bryce, M. R.; Wang, C.; Jitchati, R.; Batsanov, A. S.; Higgins, S. J.; Lambert, C. J.; Nichols, R. J. Identifying Diversity in Nanoscale Electrical Break Junctions. *Journal of the American Chemical Society* **2010**, *132* (26), 9157–9164. <https://doi.org/10.1021/ja103327f>.
- (50) Solomon, G. C.; Vura-Weis, J.; Herrmann, C.; Wasielewski, M. R.; Ratner, M. A. Understanding Coherent Transport through π -Stacked Systems upon Spatial Dislocation. *Journal of Physical Chemistry B* **2010**, *114* (45), 14735–14744. <https://doi.org/10.1021/jp103110h>.
- (51) Frisenda, R.; Janssen, V. A. E. C.; Grozema, F. C.; Van Der Zant, H. S. J.; Renaud, N. Mechanically Controlled Quantum Interference in Individual π -Stacked Dimers. *Nature Chemistry* **2016**, *8* (12), 1099–1104. <https://doi.org/10.1038/nchem.2588>.
- (52) González, M. T.; Leary, E.; García, R.; Verma, P.; Herranz, M. Á.; Rubio-Bollinger,

- G.; Martín, N.; Agraït, N. Break-Junction Experiments on Acetyl-Protected Conjugated Dithiols under Different Environmental Conditions. *Journal of Physical Chemistry C* **2011**, *115* (36), 17973–17978. <https://doi.org/10.1021/jp204005v>.
- (53) Crick, F.; Watson, J. Molecular Structure of Nucleic Acids: A Structure for Deoxyribose Nucleic Acid. *Nature* **1953**, *171*, 737–738. <https://doi.org/10.1038/171737a0>.
- (54) Ge, L.; Hou, S.; Chen, Y.; Wu, Q.; Long, L.; Yang, X.; Ji, Y.; Lin, L.; Xue, G.; Liu, J.; Liu, X.; Lambert, C. J.; Hong, W.; Zheng, Y. Hydrogen-Bond-Induced Quantum Interference in Single-Molecule Junctions of Regioisomers. *Chemical Science* **2022**, *13* (33), 9552–9559. <https://doi.org/10.1039/d2sc03229e>.
- (55) Li, Y.; Tu, X.; Wang, M.; Wang, H.; Sanvito, S.; Hou, S. Microscopic Mechanism of Electron Transfer through the Hydrogen Bonds between Carboxylated Alkanethiol Molecules Connected to Gold Electrodes. *Journal of Chemical Physics* **2014**, *141* (17). <https://doi.org/10.1063/1.4900511>.
- (56) Pirrotta, A.; De Vico, L.; Solomon, G. C.; Franco, I. Single-Molecule Force-Conductance Spectroscopy of Hydrogen-Bonded Complexes. *Journal of Chemical Physics* **2017**, *146* (9). <https://doi.org/10.1063/1.4976626>.
- (57) Wu, C.; Alqahtani, A.; Sangtarash, S.; Vezzoli, A.; Sadeghi, H.; Robertson, C. M.; Cai, C.; Lambert, C. J.; Higgins, S. J.; Nichols, R. J. In Situ Formation of H-Bonding Imidazole Chains in Break-Junction Experiments. *Nanoscale* **2020**, *12* (14), 7914–7920. <https://doi.org/10.1039/d0nr00630k>.
- (58) Zhou, C.; Li, X.; Gong, Z.; Jia, C.; Lin, Y.; Gu, C.; He, G.; Zhong, Y.; Yang, J.; Guo, X. Direct Observation of Single-Molecule Hydrogen-Bond Dynamics with Single-Bond Resolution. *Nature Communications* **2018**, *9* (1), 1–9. <https://doi.org/10.1038/s41467-018-03203-1>.
- (59) Nishino, T.; Hayashi, N.; Bui, P. T. Direct Measurement of Electron Transfer through a Hydrogen Bond between Single Molecules. *Journal of the American Chemical Society* **2013**, *135* (12), 4592–4595. <https://doi.org/10.1021/ja311463b>.
- (60) Chen, Y.; Wang, H.-C.; Tang, Y.; Zhou, Y.; Huang, L.; Cao, J.; Tang, C.; Zhang, M.; Shi, J.; Liu, J. Modulation of Charge Transport through Single-Molecule Bilactam Junctions by Tuning Hydrogen Bonds. *Chemical Communications* **2021**, *57* (15), 1935–1938. <https://doi.org/10.1039/D0CC07423C>.
- (61) Chang, S.; He, J.; Kibel, A.; Lee, M.; Sankey, O.; Zhang, P.; Lindsay, S. Tunnelling Readout of Hydrogen-Bonding-Based Recognition. *Nature Nanotechnology* **2009**, *4* (5), 297–301. <https://doi.org/10.1038/nnano.2009.48>.

- (62) Jones, L. O.; Mosquera, M. A.; Schatz, G. C.; Ratner, M. A. Molecular Junctions Inspired by Nature: Electrical Conduction through Noncovalent Nanobelts. *The Journal of Physical Chemistry B* **2019**, *123* (38), 8096–8102. <https://doi.org/10.1021/acs.jpcc.9b06255>.
- (63) Chen, H.; Fraser Stoddart, J. From Molecular to Supramolecular Electronics. *Nature Reviews Materials* **2021**, *6* (9), 804–828. <https://doi.org/10.1038/s41578-021-00302-2>.
- (64) Ayinla, R. T.; Shiri, M.; Song, B.; Gangishetty, M.; Wang, K. The Pivotal Role of Non-Covalent Interactions in Single-Molecule Charge Transport. *Materials Chemistry Frontiers* **2023**. <https://doi.org/10.1039/D3QM00210A>.
- (65) Wang, L.; Gong, Z.; Li, S.; Hong, W.; Zhong, Y.; Wang, D.; Wan, L. Molecular Conductance through a Quadruple-Hydrogen-Bond-Bridged Supramolecular Junction. *Angewandte Chemie International Edition* **2016**, *55* (40), 12393–12397.
- (66) Rodrigues, V.; Fuhrer, T.; Ugarte, D. Signature of Atomic Structure in the Quantum Conductance of Gold Nanowires. *Physical Review Letters* **2000**, *85* (19), 4124–4127. <https://doi.org/10.1103/PhysRevLett.85.4124>.
- (67) McNeely, J.; Miller, N.; Pan, X.; Lawson, B.; Kamenetska, M. Angstrom-Scale Ruler Using Single Molecule Conductance Signatures. *Journal of Physical Chemistry C* **2020**, *124* (24), 13427–13433. <https://doi.org/10.1021/acs.jpcc.0c02063>.
- (68) Arnold, A.; Weigend, F.; Evers, F. Quantum Chemistry Calculations for Molecules Coupled to Reservoirs: Formalism, Implementation, and Application to Benzenedithiol. *Journal of Chemical Physics* **2007**, *126* (17). <https://doi.org/10.1063/1.2716664>.
- (69) Blum, V.; Gehrke, R.; Hanke, F.; Havu, P.; Havu, V.; Ren, X.; Reuter, K.; Scheffler, M. Ab Initio Molecular Simulations with Numeric Atom-Centered Orbitals. *Computer Physics Communications* **2009**, *180* (11), 2175–2196. <https://doi.org/10.1016/j.cpc.2009.06.022>.
- (70) Wilhelm, J.; Walz, M.; Stendel, M.; Bagrets, A.; Evers, F. Ab Initio Simulations of Scanning-Tunneling-Microscope Images with Embedding Techniques and Application to C58-Dimers on Au(111). *Physical Chemistry Chemical Physics* **2013**, *15* (18), 6684–6690. <https://doi.org/10.1039/c3cp44286a>.
- (71) Perdew, J. P.; Burke, K.; Ernzerhof, M. Generalized Gradient Approximation Made Simple. *Physical Review Letters* **1996**, *77* (18), 3865–3868. <https://doi.org/10.1103/PhysRevLett.77.3865>.

- (72) Lawson, B.; Zahl, P.; Hybertsen, M. S.; Kamenetska, M. Formation and Evolution of Metallocene Single-Molecule Circuits with Direct Gold-III Links. *Journal of the American Chemical Society* **2022**, *144* (14), 6504–6515. <https://doi.org/10.1021/jacs.2c01322>.
- (73) van Setten, M. J.; Caruso, F.; Sharifzadeh, S.; Ren, X.; Scheffler, M.; Liu, F.; Lischner, J.; Lin, L.; Deslippe, J. R.; Louie, S. G.; Yang, C.; Weigend, F.; Neaton, J. B.; Evers, F.; Rinke, P. GW100: Benchmarking G0W0 for Molecular Systems. *Journal of Chemical Theory and Computation* **2015**, *11* (12), 5665–5687. <https://doi.org/10.1021/acs.jctc.5b00453>.
- (74) Bagrets, A. Spin-Polarized Electron Transport across Metal-Organic Molecules: A Density Functional Theory Approach. *Journal of Chemical Theory and Computation* **2013**, *9* (6), 2801–2815. <https://doi.org/10.1021/ct4000263>.
- (75) Hoffmann, R. Interaction of Orbitals through Space and through Bonds. *Accounts of Chemical Research* **1971**, *4* (1), 1–9. <https://doi.org/10.1021/ar50037a001>.
- (76) Adak, O.; Rosenthal, E.; Meisner, J.; Andrade, E. F.; Pasupathy, A. N.; Nuckolls, C.; Hybertsen, M. S.; Venkataraman, L. Flicker Noise as a Probe of Electronic Interaction at Metal-Single Molecule Interfaces. *Nano Letters* **2015**, *15* (6), 4143–4149. <https://doi.org/10.1021/acs.nanolett.5b01270>.
- (77) Meisner, J. S.; Ahn, S.; Aradhya, S. V.; Krikorian, M.; Parameswaran, R.; Steigerwald, M.; Venkataraman, L.; Nuckolls, C. Importance of Direct Metal- π Coupling in Electronic Transport through Conjugated Single-Molecule Junctions. *Journal of the American Chemical Society* **2012**, *134* (50), 20440–20445.
- (78) Sydoruk, V. A.; Xiang, D.; Vitusevich, S. A.; Petrychuk, M. V.; Vladyka, A.; Zhang, Y.; Offenhäusser, A.; Kochelap, V. A.; Belyaev, A. E.; Mayer, D. Noise and Transport Characterization of Single Molecular Break Junctions with Individual Molecule. *Journal of Applied Physics* **2012**, *112* (1), 14908. <https://doi.org/10.1063/1.4736558>.
- (79) Fu, T.; Smith, S.; Camarasa-Gómez, M.; Yu, X.; Xue, J.; Nuckolls, C.; Evers, F.; Venkataraman, L.; Wei, S. Enhanced Coupling through π -Stacking in Imidazole-Based Molecular Junctions. *Chemical Science* **2019**, *10* (43), 9998–10002. <https://doi.org/10.1039/c9sc03760h>.
- (80) Lucia Herrer, I.; K. Ismael, A.; C. Milán, D.; Vezzoli, A.; Martín, S.; González-Orive, A.; Grace, I.; Lambert, C.; L. Serrano, J.; J. Nichols, R.; Cea, P. Unconventional Single-Molecule Conductance Behavior for a New Heterocyclic Anchoring Group: Pyrazolyl. *The Journal of Physical Chemistry Letters* **2018**, *9* (18), 5364–5372. <https://doi.org/10.1021/acs.jpcclett.8b02051>.

- (81) Li, X.; He, J.; Hihath, J.; Xu, B.; M. Lindsay, S.; Tao, N. Conductance of Single Alkanedithiols: Conduction Mechanism and Effect of Molecule–Electrode Contacts. *Journal of the American Chemical Society* **2006**, *128* (6), 2135–2141. <https://doi.org/10.1021/ja057316x>.
- (82) A. Martin, C.; Ding, D.; Kryger Sørensen, J.; Bjørnholm, T.; M. van Ruitenbeek, J.; S. J. van der Zant, H. Fullerene-Based Anchoring Groups for Molecular Electronics. *Journal of the American Chemical Society* **2008**, *130* (40), 13198–13199. <https://doi.org/10.1021/ja804699a>.
- (83) Xiao; Xu; J. Tao, N. Measurement of Single Molecule Conductance: Benzenedithiol and Benzenedimethanethiol. *Nano Letters* **2004**, *4* (2), 267–271. <https://doi.org/10.1021/nl035000m>.
- (84) Joule, J. A.; Mills, K. *Heterocyclic Chemistry 5th Edition*; **2009**. <https://doi.org/10.1039/b614418g>.
- (85) Sundberg, R. J. Interactions of Histidine and Other Imidazole Derivatives with Transition Metal Ions in Chemical and Biological Systems. *Chemical Reviews* **1974**, *74* (4), 471–517. <https://doi.org/10.1021/cr60290a003>.
- (86) Xu, B. Q.; Xiao, X. Y.; Tao, N. J. Measurements of Single-Molecule Electromechanical Properties. *Journal of the American Chemical Society* **2003**, *125* (52), 16164–16165. <https://doi.org/10.1021/ja038949j>.
- (87) Hybertsen, M. S.; Venkataraman, L. Structure-Property Relationships in Atomic-Scale Junctions: Histograms and Beyond. *Accounts of chemical research* **2016**, *49*(3), 452-460. <https://doi.org/10.1021/acs.accounts.6b00004>.
- (88) Mishchenko, A.; Zotti, L. A.; Vonlanthen, D.; Bürkle, M.; Pauly, F.; Cuevas, J. C.; Mayor, M.; Wandlowski, T. Single-Molecule Junctions Based on Nitrile-Terminated Biphenyls: A Promising New Anchoring Group. *Journal of the American Chemical Society* **2011**, *133* (2), 184–187. <https://doi.org/10.1021/ja107340t>.
- (89) Hybertsen, M. S.; Venkataraman, L.; Klare, J. E.; Whalley, A. C.; Steigerwald, M. L.; Nuckolls, C. Amine-Linked Single-Molecule Circuits: Systematic Trends across Molecular Families. *Journal of Physics Condensed Matter* **2008**, *20* (37), 374115. <https://doi.org/10.1088/0953-8984/20/37/374115>.
- (90) Aoshima, S.; Higashimura, T. Living Cationic Polymerization of Vinyl Monomers by Organoaluminum Halides. 3. Living Polymerization of Isobutyl Vinyl Ether by EtAlCl₂ in the Presence of Ester Additives. *Macromolecules* **1989**, *22* (3), 1009–1013. <https://doi.org/10.1021/ma00193a001>.

- (91) Rumble, J. R. ed. *Handbook of Chemistry and Physics 100th Edition*; **2019**. https://doi.org/10.1007/978-3-642-14998-6_4.
- (92) ECHA. Support Document for Identification of N,N-Dimethylformamide As a Substance of Very High Concern Because of Its Cmr Properties. **2012**, 57 (November), 1–6.
- (93) Stone, K. R. Environmental Profile for Propylene Carbonate. *US Environmental Protection Agency* **1998**.
- (94) Silverstein, T. P.; Heller, S. T. PKa Values in the Undergraduate Curriculum: What Is the Real PKa of Water? *Journal of Chemical Education* **2017**, 94 (6), 690–695. <https://doi.org/10.1021/acs.jchemed.6b00623>.
- (95) Bauman, J. E.; Wang, J. C. Imidazole Complexes of Nickel(II), Copper(II), Zinc(II), and Silver(I). *Inorganic Chemistry* **1964**, 3 (3), 368–373. <https://doi.org/10.1021/ic50013a014>.
- (96) Park, K. S.; Ni, Z.; Côté, A. P.; Choi, J. Y.; Huang, R.; Uribe-Romo, F. J.; Chae, H. K.; O’Keeffe, M.; Yaghi, O. M. Exceptional Chemical and Thermal Stability of Zeolitic Imidazolate Frameworks. *Proceedings of the National Academy of Sciences of the United States of America* **2006**, 103 (27), 10186–10191. <https://doi.org/10.1073/pnas.0602439103>.
- (97) Fu, T.; Smith, S.; Camarasa-Gómez, M.; Yu, X.; Xue, J.; Nuckolls, C.; Evers, F.; Venkataraman, L.; Wei, S. Enhanced Coupling through π -Stacking in Imidazole-Based Molecular Junctions. *Chemical Science* **2019**, 10, 9998–10002. <https://doi.org/10.1039/c9sc03760h>.
- (98) Yanson, A. I.; Rubio Bollinger, G.; Van Den Brom, H. E.; Agraït, N.; Van Ruitenbeek, J. M. Formation and Manipulation of a Metallic Wire of Single Gold Atoms. *Nature* **1998**, 395 (6704), 783–785. <https://doi.org/10.1038/27405>.
- (99) Xue, Y.; Li, X.; Li, H.; Zhang, W. Quantifying Thiol-Gold Interactions towards the Efficient Strength Control. *Nature Communications* **2014**, 5(1), 4348. <https://doi.org/10.1038/ncomms5348>.
- (100) Frei, M.; Aradhya, S. V.; Koentopp, M.; Hybertsen, M. S.; Venkataraman, L. Mechanics and Chemistry: Single Molecule Bond Rupture Forces Correlate with Molecular Backbone Structure. *Nano Letters* **2011**, 11 (4), 1518–1523. <https://doi.org/10.1021/nl1042903>.
- (101) Tavazza, F.; Levine, L. E.; Chaka, A. M. Elongation and Breaking Mechanisms of Gold Nanowires under a Wide Range of Tensile Conditions. *Journal of Applied*

Physics **2009**, *106* (4). <https://doi.org/10.1063/1.3200957>.

- (102) Xue, G.; Dai, Q.; Jiang, S. Chemical Reactions of Imidazole with Metallic Silver Studied by the Use of SERS and XPS Techniques. *Journal of the American Chemical Society* **1988**, *110* (8), 2393–2395. <https://doi.org/10.1021/ja00216a009>.
- (103) Vladyka, A.; Perrin, M. L.; Overbeck, J.; Ferradás, R. R.; García-Suárez, V.; Gantenbein, M.; Brunner, J.; Mayor, M.; Ferrer, J.; Calame, M. In-Situ Formation of One-Dimensional Coordination Polymers in Molecular Junctions. *Nature Communications* **2019**, *10* (1), 1–9. <https://doi.org/10.1038/s41467-018-08025-9>.
- (104) Frisch, M. J.; Trucks, G. W.; Schlegel, H. B.; Scuseria, G. E.; Robb, M. A.; Cheeseman, J. R.; Scalmani, G.; Barone, V.; Petersson, G. A.; Nakatsuji, H.; Li, X.; Caricato, M.; Marenich, A. V.; Bloino, J.; Janesko, B. G.; Gomperts, R.; Mennucci, B.; Hratch, D. J. Gaussian 16. Gaussian, Inc.: Wallingford, CT **2016**.
- (105) Glendening, E.D.; Reed, A. E.; Carpenter, J. E.; Weinhold, F. NBO Version 3.1. Gaussian, Inc.
- (106) Perdew, J. P. Density-Functional Approximation for the Correlation Energy of the Inhomogeneous Electron Gas. *Physical Review B* **1986**, *33* (12), 8822–8824. <https://doi.org/10.1103/PhysRevB.33.8822>.
- (107) Perdew, J. P.; Burke, K.; Ernzerhof, M. Generalized Gradient Approximation Made Simple. *Physical Review Letters* **1997**, *78* (7), 1396–1396. <https://doi.org/10.1103/PhysRevLett.78.1396>.
- (108) Becke, A. D. Density-Functional Thermochemistry. III. The Role of Exact Exchange. *The Journal of Chemical Physics* **1993**, *98* (7), 5648–5652. <https://doi.org/10.1063/1.464913>.
- (109) Lee, C.; Yang, W.; Parr, R. G. Development of the Colle-Salvetti Correlation-Energy Formula into a Functional of the Electron Density. *Physical Review B* **1988**, *37* (2), 785–789. <https://doi.org/10.1103/PhysRevB.37.785>.
- (110) Weigend, F.; Ahlrichs, R. Balanced Basis Sets of Split Valence, Triple Zeta Valence and Quadruple Zeta Valence Quality for H to Rn: Design and Assessment of Accuracy. *Physical Chemistry Chemical Physics* **2005**, *7* (18), 3297–3305. <https://doi.org/10.1039/b508541a>.
- (111) Rappoport, D.; Furche, F. Property-Optimized Gaussian Basis Sets for Molecular Response Calculations. *Journal of Chemical Physics* **2010**, *133* (13), 134105. <https://doi.org/10.1063/1.3484283>.

- (112) Andrae, D.; Häußermann, U.; Dolg, M.; Stoll, H.; Preuß, H. Energy-Adjusted Ab Initio Pseudopotentials for the Second and Third Row Transition Elements. *Theoretica Chimica Acta* **1990**, *77* (2), 123–141. <https://doi.org/10.1007/BF01114537>.
- (113) Kamenetska, M.; Widawsky, J. R.; Dell'Angela, M.; Frei, M.; Venkataraman, L. Temperature Dependent Tunneling Conductance of Single Molecule Junctions. *The Journal of Chemical Physics* **2017**, *146* (9), 92311.
- (114) Perrin, M. L.; Verzijl, C. J. O.; Martin, C. A.; Shaikh, A. J.; Eelkema, R.; Van Esch, J. H.; Van Ruitenbeek, J. M.; Thijssen, J. M.; Van Der Zant, H. S. J.; Dulić, D. Large Tunable Image-Charge Effects in Single-Molecule Junctions. *Nature Nanotechnology* **2013**, *8* (4), 282–287. <https://doi.org/10.1038/nnano.2013.26>.
- (115) Neaton, J. B.; Hybertsen, M. S.; Louie, S. G. Renormalization of Molecular Electronic Levels at Metal-Molecule Interfaces. *Physical Review Letters* **2006**, *97* (21). <https://doi.org/10.1103/PhysRevLett.97.216405>.
- (116) Kim, Y.; Hellmuth, T. J.; Bürkle, M.; Pauly, F.; Scheer, E. Characteristics of Amine-Ended and Thiol-Ended Alkane Single-Molecule Junctions Revealed by Inelastic Electron Tunneling Spectroscopy. *ACS Nano* **2011**, *5* (5), 4104–4111. <https://doi.org/10.1021/nn200759s>.
- (117) Aviram, A.; Ratner, M. A. Molecular Rectifiers. *Chemical Physics Letters* **1974**, *29* (2), 277–283. [https://doi.org/10.1016/0009-2614\(74\)85031-1](https://doi.org/10.1016/0009-2614(74)85031-1).
- (118) Perrin, M. L.; Burzurí, E.; Van Der Zant, H. S. J. Single-Molecule Transistors. *Chemical Society Reviews* **2015**, *44* (4), 902–919. <https://doi.org/10.1039/C4CS00231H>.
- (119) Sun, L.; Diaz-Fernandez, Y. A.; Gschneidner, T. A.; Westerlund, F.; Lara-Avila, S.; Moth-Poulsen, K. Single-Molecule Electronics: From Chemical Design to Functional Devices. *Chemical Society Reviews*. 2014. <https://doi.org/10.1039/c4cs00143e>.
- (120) Evers, F.; Korytár, R.; Tewari, S.; Van Ruitenbeek, J. M. Advances and Challenges in Single-Molecule Electron Transport. *Reviews of Modern Physics* **2020**, *92* (3), 35001. <https://doi.org/10.1103/RevModPhys.92.035001>.
- (121) Perrin, M. L.; Perrin, M. L.; Eelkema, R.; Thijssen, J.; Grozema, F. C.; Van Der Zant, H. S. J. Single-Molecule Functionality in Electronic Components Based on Orbital Resonances. *Physical Chemistry Chemical Physics* **2020**, *22* (23), 12849–12866. <https://doi.org/10.1039/D0CP01448F>.

- (122) Skipper, H. E.; May, C. V.; Rheingold, A. L.; Doerrer, L. H.; Kamenetska, M. Hard–Soft Chemistry Design Principles for Predictive Assembly of Single Molecule–Metal Junctions. *Journal of the American Chemical Society* **2021**, *143* (40), 16439–16447. <https://doi.org/10.1021/JACS.1C05142>.
- (123) Wu, C.; Alqahtani, A.; Sangtarash, S.; Vezzoli, A.; Sadeghi, H.; Robertson, C. M.; Cai, C.; Lambert, C. J.; Higgins, S. J.; Nichols, R. J. In Situ Formation of H-Bonding Imidazole Chains in Break-Junction Experiments. *Nanoscale* **2020**, *12* (14), 7914–7920. <https://doi.org/10.1039/D0NR00630K>.
- (124) Li, S.; Jiang, Y.; Wang, Y.; Hou, S. The Formation and Conducting Mechanism of Imidazole-Gold Molecular Junctions. *ChemistrySelect* **2021**, *6* (12), 2959–2965. <https://doi.org/10.1002/slct.202100507>.
- (125) Li, X.; Wu, Q.; Bai, J.; Hou, S.; Jiang, W.; Tang, C.; Song, H.; Huang, X.; Zheng, J.; Yang, Y.; Liu, J.; Hu, Y.; Shi, J.; Liu, Z.; Lambert, C. J.; Zhang, D.; Hong, W. Structure-Independent Conductance of Thiophene-Based Single-Stacking Junctions. *Angewandte Chemie International Edition* **2020**, *59* (8), 3280–3286. <https://doi.org/10.1002/ANIE.201913344>.
- (126) Zhang, C.; Cheng, J.; Wu, Q.; Hou, S.; Feng, S.; Jiang, B.; Lambert, C. J.; Gao, X.; Li, Y.; Li, J. Enhanced π - π Stacking between Dipole-Bearing Single Molecules Revealed by Conductance Measurement. *Journal of the American Chemical Society* **2023**, *145* (3), 1617–1630. https://doi.org/10.1021/JACS.2C09656/ASSET/IMAGES/MEDIUM/JA2C09656_0007.GIF.
- (127) Reznikova, K.; Hsu, C.; Schosser, W. M.; Gallego, A.; Beltako, K.; Pauly, F.; van der Zant, H. S. J.; Mayor, M. Substitution Pattern Controlled Quantum Interference in [2.2]Paracyclophane-Based Single-Molecule Junctions. *Journal of the American Chemical Society* **2021**, *143* (34), 13944–13951. <https://doi.org/10.1021/jacs.1c06966>.
- (128) Soler, J. M.; Artacho, E.; Gale, J. D.; García, A.; Junquera, J.; Ordejón, P.; Sánchez-Portal, D. The SIESTA Method for Ab Initio Order-N Simulation. *Journal of Physics: Condensed Matter* **2002**, *14* (11), 2745. <https://doi.org/10.1088/0953-8984/14/11/302>.
- (129) Dion, M.; Rydberg, H.; Schröder, E.; Langreth, D. C.; Lundqvist, B. I. Van Der Waals Density Functional for General Geometries. *Physical Review Letters* **2004**, *92* (24), 22–25. <https://doi.org/10.1103/PhysRevLett.92.246401>.
- (130) Román-Pérez, G.; Soler, J. M. Efficient Implementation of a van Der Waals Density Functional: Application to Double-Wall Carbon Nanotubes. *Physical Review*

Letters **2009**, *103* (9), 1–4. <https://doi.org/10.1103/PhysRevLett.103.096102>.

- (131) Papior, N.; Lorente, N.; Frederiksen, T.; García, A.; Brandbyge, M. Improvements on Non-Equilibrium and Transport Green Function Techniques: The next-Generation TRANSIESTA. *Computer Physics Communications* **2017**, *212*, 8–24. <https://doi.org/10.1016/j.cpc.2016.09.022>.
- (132) Miao, Z.; Quainoo, T.; M. Czyszczonek-Burton, T.; Rotthowe, N.; M. Parr, J.; Liu, Z.-F.; S. Inkpen, M. Charge Transport Across Dynamic Covalent Chemical Bridges. *Nano Letters* **2022**, *22* (20), 8331–8338. <https://doi.org/10.1021/acs.nanolett.2c03288>.
- (133) Sautet, P.; Joachim, C. Electronic Interference Produced by a Benzene Embedded in a Polyacetylene Chain. *Chemical Physics Letters* **1988**, *153* (6), 511–516. [https://doi.org/https://doi.org/10.1016/0009-2614\(88\)85252-7](https://doi.org/https://doi.org/10.1016/0009-2614(88)85252-7).
- (134) Magoga, M.; Joachim, C. Conductance of Molecular Wires Connected or Bonded in Parallel. *Physical Review B* **1999**, *59* (24), 16011–16021. <https://doi.org/10.1103/PhysRevB.59.16011>.
- (135) Papior, N.; Lorente, N.; Frederiksen, T.; García, A.; Brandbyge, M. Improvements on Non-Equilibrium and Transport Green Function Techniques: The next-Generation Transiesta. *Computer Physics Communications* **2017**, *212*, 8–24. <https://doi.org/10.1016/J.CPC.2016.09.022>.
- (136) Román-Pérez, G.; Soler, J. M. Efficient Implementation of a van Der Waals Density Functional: Application to Double-Wall Carbon Nanotubes. *Physical Review Letters* **2009**, *103* (9), 096102. <https://doi.org/10.1103/PHYSREVLETT.103.096102/FIGURES/1/MEDIUM>.
- (137) Yoshida, K.; Pobelov, I. V.; Manrique, D. Z.; Pope, T.; Mészáros, G.; Gulcur, M.; Bryce, M. R.; Lambert, C. J.; Wandlowski, T. Correlation of Breaking Forces, Conductances and Geometries of Molecular Junctions. *Scientific Reports* **2015**, *5* (1), 9002. <https://doi.org/10.1038/srep09002>.
- (138) Untiedt, C.; Yanson, A. I.; Grande, R.; Rubio-Bollinger, G.; Agraït, N.; Vieira, S.; van Ruitenbeek, J. M. Calibration of the Length of a Chain of Single Gold Atoms. *Physical Review B - Condensed Matter and Materials Physics* **2002**, *66* (8), 854181–854186. <https://doi.org/10.1103/PhysRevB.66.085418>.
- (139) Doud, E. A.; Starr, R. L.; Kladnik, G.; Voevodin, A.; Montes, E.; Arasu, N. P.; Zang, Y.; Zahl, P.; Morgante, A.; Venkataraman, L.; Vázquez, H.; Cvetko, D.; Roy, X. Cyclopropenylidenes as Strong Carbene Anchoring Groups on Au Surfaces. *Journal of the American Chemical Society* **2020**, *142* (47).

<https://doi.org/10.1021/jacs.0c10743>.

- (140) Brédas, J. L.; Calbert, J. P.; Da Silva Filho, D. A.; Cornil, J. Organic Semiconductors: A Theoretical Characterization of the Basic Parameters Governing Charge Transport. *Proceedings of the National Academy of Sciences of the United States of America* **2002**, *99* (9). <https://doi.org/10.1073/pnas.092143399>.
- (141) Refaely-Abramson, S.; Liu, Z. F.; Bruneval, F.; Neaton, J. B. First-Principles Approach to the Conductance of Covalently Bound Molecular Junctions. *Journal of Physical Chemistry C* **2019**, *123* (11). <https://doi.org/10.1021/acs.jpcc.8b12124>.
- (142) Montes, E.; Vázquez, H. Calculation of Energy Level Alignment and Interface Electronic Structure in Molecular Junctions beyond DFT. *Journal of Physical Chemistry C* **2021**, *125* (46). <https://doi.org/10.1021/acs.jpcc.1c07407>.
- (143) Katz, E.; Willner, I. Integrated Nanoparticle-Biomolecule Hybrid Systems: Synthesis, Properties, and Applications. *Angewandte Chemie - International Edition* **2004**, *43* (45), 6042–6108. <https://doi.org/10.1002/anie.200400651>.
- (144) Kimura-Suda, H.; Petrovykh, D. Y.; Tarlov, M. J.; Whitman, L. J. Base-Dependent Competitive Adsorption of Single-Stranded DNA on Gold. *Journal of the American Chemical Society* **2003**, *125* (30), 9014–9015. <https://doi.org/10.1021/ja035756n>.
- (145) Barhoumi, A.; Zhang, D.; Tam, F.; Halas, N. J. Surface-Enhanced Raman Spectroscopy of DNA. *Journal of the American Chemical Society* **2008**, *130* (16), 5523–5529. <https://doi.org/10.1021/ja800023j>.
- (146) Giese, B.; McNaughton, D. Surface-Enhanced Raman Spectroscopic and Density Functional Theory Study of Adenine Adsorption to Silver Surfaces. *Journal of Physical Chemistry B* **2002**, *106* (1), 101–112. <https://doi.org/10.1021/jp010789f>.
- (147) Kundu, J.; Neumann, O.; Janesko, B. G.; Zhang, D.; Lal, S.; Barhoumi, A.; Scuseria, G. E.; Halas, N. J. Adenine-and Adenosine Monophosphate (AMP)-Gold Binding Interactions Studied by Surface-Enhanced Raman and Infrared Spectroscopies. *Journal of Physical Chemistry C* **2009**, *113* (32), 14390–14397. <https://doi.org/10.1021/jp903126f>.
- (148) Pagliai, M.; Caporali, S.; Muniz-Miranda, M.; Pratesi, G.; Schettino, V. SERS, XPS, and DFT Study of Adenine Adsorption on Silver and Gold Surfaces. *Journal of Physical Chemistry Letters* **2012**, *3* (2), 242–245. <https://doi.org/10.1021/jz201526v>.
- (149) Yao, G.; Zhai, Z.; Zhong, J.; Huang, Q. DFT and SERS Study of ¹⁵N Full-Labeled Adenine Adsorption on Silver and Gold Surfaces. *Journal of Physical Chemistry C*

- 2017**, *121* (18), 9869–9878. <https://doi.org/10.1021/acs.jpcc.7b00818>.
- (150) Watanabe, H.; Ishida, Y.; Hayazawa, N.; Inouye, Y.; Kawata, S. Tip-Enhanced near-Field Raman Analysis of Tip-Pressurized Adenine Molecule. *Physical Review B - Condensed Matter and Materials Physics* **2004**, *69* (15), 1–11. <https://doi.org/10.1103/PhysRevB.69.155418>.
- (151) Domke, K. F.; Zhang, D.; Pettinger, B. Tip-Enhanced Raman Spectra of Picomole Quantities of DNA Nucleobases at Au(111). *Journal of the American Chemical Society* **2007**, *129* (21), 6708–6709. <https://doi.org/10.1021/ja071107q>.
- (152) Madzharova, F.; Heiner, Z.; Gühlke, M.; Kneipp, J. Surface-Enhanced Hyper-Raman Spectra of Adenine, Guanine, Cytosine, Thymine, and Uracil. *Journal of Physical Chemistry C* **2016**, *120* (28), 15415–15423. <https://doi.org/10.1021/acs.jpcc.6b02753>.
- (153) Rodes, A.; Rueda, M.; Prieto, F.; Prado, C.; Feliu, J. M.; Aldaz, A. Adenine Adsorption at Single Crystal and Thin-Film Gold Electrodes: An in Situ Infrared Spectroscopy Study. *Journal of Physical Chemistry C* **2009**, *113* (43), 18784–18794. <https://doi.org/10.1021/jp906672u>.
- (154) Rosa, M.; Corni, S.; Felice, R. Di. Interaction of Nucleic Acid Bases with the Au(111) Surface. *Journal of Chemical Theory and Computation* **2013**, *9* (10), 4552–4561. <https://doi.org/10.1021/ct4002416>.
- (155) Piana, S.; Bilic, A. The Nature of the Adsorption of Nucleobases on the Gold [111] Surface. *Journal of Physical Chemistry B* **2006**, *110* (46), 23467–23471. <https://doi.org/10.1021/jp064438i>.
- (156) Harroun, S. G. The Controversial Orientation of Adenine on Gold and Silver. *ChemPhysChem* **2018**, *19* (9), 1003–1015. <https://doi.org/10.1002/cphc.201701223>.
- (157) Cohen, B.; Hare, P. M.; Kohler, B. Ultrafast Excited-State Dynamics of Adenine and Monomethylated Adenines in Solution: Implications for the Nonradiative Decay Mechanism. *Journal of the American Chemical Society* **2003**, *125* (44), 13594–13601. <https://doi.org/10.1021/ja035628z>.
- (158) Adamo, C.; Barone, V. Toward Reliable Density Functional Methods without Adjustable Parameters: The PBE0 Model. *The Journal of Chemical Physics* **1999**, *110* (13), 6158–6170. <https://doi.org/10.1063/1.478522>.
- (159) Grimme, S.; Antony, J.; Ehrlich, S.; Krieg, H. A Consistent and Accurate Ab Initio Parametrization of Density Functional Dispersion Correction (DFT-D) for the 94 Elements H-Pu. *The Journal of Chemical Physics* **2010**, *132* (15), 154104.

<https://doi.org/10.1063/1.3382344>.

- (160) Frisch, M. J.; Trucks, G. W.; Schlegel, H. B.; Scuseria, G. E.; Robb, M. a.; Cheeseman, J. R.; Scalmani, G.; Barone, V.; Petersson, G. a.; Nakatsuji, H.; Li, X.; Caricato, M.; Marenich, a. V.; Bloino, J.; Janesko, B. G.; Gomperts, R.; Mennucci, B.; Hratchian, H. P.; Ortiz, J. V.; Izmaylov, a. F.; Sonnenberg, J. L.; Williams; Ding, F.; Lipparini, F.; Egidi, F.; Goings, J.; Peng, B.; Petrone, A.; Henderson, T.; Ranasinghe, D.; Zakrzewski, V. G.; Gao, J.; Rega, N.; Zheng, G.; Liang, W.; Hada, M.; Ehara, M.; Toyota, K.; Fukuda, R.; Hasegawa, J.; Ishida, M.; Nakajima, T.; Honda, Y.; Kitao, O.; Nakai, H.; Vreven, T.; Throssell, K.; Montgomery Jr., J. a.; Peralta, J. E.; Ogliaro, F.; Bearpark, M. J.; Heyd, J. J.; Brothers, E. N.; Kudin, K. N.; Staroverov, V. N.; Keith, T. a.; Kobayashi, R.; Normand, J.; Raghavachari, K.; Rendell, a. P.; Burant, J. C.; Iyengar, S. S.; Tomasi, J.; Cossi, M.; Millam, J. M.; Klene, M.; Adamo, C.; Cammi, R.; Ochterski, J. W.; Martin, R. L.; Morokuma, K.; Farkas, O.; Foresman, J. B.; Fox, D. J. Gaussian 16, Revision A.03. 2016, p Gaussian 16, Revision A.03, Gaussian, Inc., Wallin.
- (161) Boys, S. F.; Bernardi, F. The Calculation of Small Molecular Interactions by the Differences of Separate Total Energies. Some Procedures with Reduced Errors. *Molecular Physics* **1970**, *19* (4), 553–566. <https://doi.org/10.1080/00268977000101561>.
- (162) Mao, Y.; Loipersberger, M.; Kron, K. J.; Derrick, J. S.; Chang, C. J.; Sharada, S. M.; Head-Gordon, M. Consistent Inclusion of Continuum Solvation in Energy Decomposition Analysis: Theory and Application to Molecular CO₂reduction Catalysts. *Chemical Science* **2021**, *12* (4), 1398–1414. <https://doi.org/10.1039/d0sc05327a>.
- (163) Shao, Y.; Gan, Z.; Epifanovsky, E.; Gilbert, A. T. B.; Wormit, M.; Kussmann, J.; Lange, A. W.; Behn, A.; Deng, J.; Feng, X.; Ghosh, D.; Goldey, M.; Horn, P. R.; Jacobson, L. D.; Kaliman, I.; Khaliullin, R. Z.; Kuš, T.; Landau, A.; Liu, J.; Proynov, E. I.; Rhee, Y. M.; Richard, R. M.; Rohrdanz, M. A.; Steele, R. P.; Sundstrom, E. J.; Woodcock, H. L.; Zimmerman, P. M.; Zuev, D.; Albrecht, B.; Alguire, E.; Austin, B.; Beran, G. J. O.; Bernard, Y. A.; Berquist, E.; Brandhorst, K.; Bravaya, K. B.; Brown, S. T.; Casanova, D.; Chang, C. M.; Chen, Y.; Chien, S. H.; Closser, K. D.; Crittenden, D. L.; Diedenhofen, M.; Distasio, R. A.; Do, H.; Dutoi, A. D.; Edgar, R. G.; Fatehi, S.; Fusti-Molnar, L.; Ghysels, A.; Golubeva-Zadorozhnaya, A.; Gomes, J.; Hanson-Heine, M. W. D.; Harbach, P. H. P.; Hauser, A. W.; Hohenstein, E. G.; Holden, Z. C.; Jagau, T. C.; Ji, H.; Kaduk, B.; Khistyayev, K.; Kim, J.; Kim, J.; King, R. A.; Klunzinger, P.; Kosenkov, D.; Kowalczyk, T.; Krauter, C. M.; Lao, K. U.; Laurent, A. D.; Lawler, K. V.; Levchenko, S. V.; Lin, C. Y.; Liu, F.; Livshits, E.; Lochan, R. C.; Luenser, A.; Manohar, P.; Manzer, S. F.; Mao, S. P.; Mardirossian, N.; Marenich, A. V.; Maurer, S. A.; Mayhall, N. J.; Neuscamman, E.; Oana, C. M.; Olivares-Amaya, R.; Oneill, D. P.; Parkhill, J. A.; Perrine, T. M.; Peverati, R.;

- Prociuk, A.; Rehn, D. R.; Rosta, E.; Russ, N. J.; Sharada, S. M.; Sharma, S.; Small, D. W.; Sodt, A.; Stein, T.; Stück, D.; Su, Y. C.; Thom, A. J. W.; Tsuchimochi, T.; Vanovschi, V.; Vogt, L.; Vydrov, O.; Wang, T.; Watson, M. A.; Wenzel, J.; White, A.; Williams, C. F.; Yang, J.; Yeganeh, S.; Yost, S. R.; You, Z. Q.; Zhang, I. Y.; Zhang, X.; Zhao, Y.; Brooks, B. R.; Chan, G. K. L.; Chipman, D. M.; Cramer, C. J.; Goddard, W. A.; Gordon, M. S.; Hehre, W. J.; Klamt, A.; Schaefer, H. F.; Schmidt, M. W.; Sherrill, C. D.; Truhlar, D. G.; Warshel, A.; Xu, X.; Aspuru-Guzik, A.; Baer, R.; Bell, A. T.; Besley, N. A.; Chai, J. Da; Dreuw, A.; Dunietz, B. D.; Furlani, T. R.; Gwaltney, S. R.; Hsu, C. P.; Jung, Y.; Kong, J.; Lambrecht, D. S.; Liang, W.; Ochsenfeld, C.; Rassolov, V. A.; Slipchenko, L. V.; Subotnik, J. E.; Van Voorhis, T.; Herbert, J. M.; Krylov, A. I.; Gill, P. M. W.; Head-Gordon, M. *Advances in Molecular Quantum Chemistry Contained in the Q-Chem 4 Program Package. Molecular Physics* **2015**, *113* (2), 184–215. <https://doi.org/10.1080/00268976.2014.952696>.
- (164) Chen, Y.; Huang, M.; Zhou, Q.; Li, Z.; Meng, J.; Pan, M.; Ye, X.; Liu, T.; Chang, S.; Xiao, S. Regio- and Steric Effects on Single Molecule Conductance of Phenanthrenes. *Nano Letters* **2021**, *21* (24), 10333–10340. <https://doi.org/10.1021/acs.nanolett.1c03565>.
- (165) Venkataraman, L.; Klare, J. E.; Nuckolls, C.; Hybertsen, M. S.; Steigerwald, M. L. Dependence of Single-Molecule Junction Conductance on Molecular Conformation. *Nature* **2006**, *442* (7105), 904–907. <https://doi.org/10.1038/nature05037>.
- (166) Rodrigues, V.; Fuhrer, T.; Ugarte, D. Signature of Atomic Structure in the Quantum Conductance of Gold Nanowires. *Physical Review Letters* **2000**, *85* (19), 4124–4127. <https://doi.org/10.1103/PhysRevLett.85.4124>.
- (167) Sabater, C.; Caturla, M. J.; Palacios, J. J.; Untiedt, C. Understanding the Structure of the First Atomic Contact in Gold. *Nanoscale Research Letters* **2013**, *8* (1), 257. <https://doi.org/10.1186/1556-276X-8-257>.
- (168) Lawson, B.; Zahl, P.; Hybertsen, M. S.; Kamenetska, M. Formation and Evolution of Metallocene Single-Molecule Circuits with Direct Gold- π Links. *Journal of the American Chemical Society* **2022**, *144* (14), 6504–6515. <https://doi.org/10.1021/jacs.2c01322>.
- (169) Toher, C.; Filippetti, A.; Sanvito, S.; Burke, K. Self-Interaction Errors in Density-Functional Calculations of Electronic Transport. *Physical Review Letters* **2005**, *95* (14), 1–4. <https://doi.org/10.1103/PhysRevLett.95.146402>.
- (170) Koentopp, M.; Burke, K.; Evers, F. Zero-Bias Molecular Electronics: Exchange-Correlation Corrections to Landauer's Formula. *Physical Review B - Condensed Matter and Materials Physics* **2006**, *73* (12), 1–4.

<https://doi.org/10.1103/PhysRevB.73.121403>.

- (171) Ke, S. H.; Baranger, H. U.; Yang, W. Role of the Exchange-Correlation Potential in Ab Initio Electron Transport Calculations. *Journal of Chemical Physics* **2007**, *126* (20). <https://doi.org/10.1063/1.2743004>.
- (172) Wu, T. P.; Wang, T.; Seetin, M. G.; Lai, Y.; Zhu, S.; Lin, K.; Liu, Y.; Byrum, S. D.; Mackintosh, S. G.; Zhong, M.; Tackett, A.; Wang, G.; Hon, L. S.; Fang, G.; Swenberg, J. A.; Xiao, A. Z. DNA Methylation on N6-Adenine in Mammalian Embryonic Stem Cells. *Nature* **2016**, *532* (7599), 329. <https://doi.org/10.1038/NATURE17640>.
- (173) Kool, E. T. Hydrogen Bonding, Base Stacking, and Steric Effects in DNA Replication. *Annual Review of Biophysics and Biomolecular Structure* **2001**, *30* (1), 1–22. <https://doi.org/10.1146/annurev.biophys.30.1.1>.
- (174) Eisenberg, D. The Discovery of the α -Helix and β -Sheet, the Principal Structural Features of Proteins. *Proceedings of the National Academy of Sciences of the United States of America* **2003**, *100* (20), 11207–11210. <https://doi.org/10.1073/pnas.2034522100>.
- (175) Correa, J. V.; Herrera, B.; Toro-Labbé, A. Characterization of the Reactive Conformations of Protonated Histamine through the Reaction Force Analysis and the Dual Descriptor of Chemical Reactivity. *Journal of Molecular Structure: THEOCHEM* **2007**, *817* (1–3), 111–118. <https://doi.org/10.1016/j.theochem.2007.04.028>.
- (176) Prins, L. J.; Reinhoudt, D. N.; Timmerman, P. Noncovalent Synthesis Using Hydrogen Bonding. *Angewandte Chemie International Edition* **2001**, *40* (13), 2382–2426. [https://doi.org/10.1002/1521-3773\(20010702\)40:13<2382::AID-ANIE2382>3.0.CO;2-G](https://doi.org/10.1002/1521-3773(20010702)40:13<2382::AID-ANIE2382>3.0.CO;2-G).
- (177) Ramírez, F. J.; Tuñón, I.; Collado, J. A.; Silla, E. Structural and Vibrational Study of the Tautomerism of Histamine Free-Base in Solution. *Journal of the American Chemical Society* **2003**, *125* (8), 2328–2340. <https://doi.org/10.1021/ja027103x>.
- (178) Zhu, H.; Liu, S.; Guo, Z.; Yan, K.; Shen, J.; Zhang, Z.; Chen, J.; Guo, Y.; Liu, L.; Wu, X. Strong Histamine Torsion Raman Spectrum Enables Direct, Rapid, and Ultrasensitive Detection of Allergic Diseases. *iScience* **2021**, *24* (11), 103384. <https://doi.org/10.1016/j.isci.2021.103384>.
- (179) Kodchakorn, K.; Nimmanpipug, P.; Phongtamrug, S.; Tashiro, K. pH-Induced Conformational Changes in Histamine in the Solid State. *RSC Advances* **2019**, *9* (34), 19375–19389. <https://doi.org/10.1039/c9ra03418h>.

- (180) Holgate, S. T.; Polosa, R. Treatment Strategies for Allergy and Asthma. *Nature Reviews Immunology* **2008**, *8* (3), 218–230. <https://doi.org/10.1038/nri2262>.
- (181) Akdis, M.; Akdis, C. A. Therapeutic Manipulation of Immune Tolerance in Allergic Disease. *Nature Reviews Drug Discovery* **2009**, *8* (8), 645–660. <https://doi.org/10.1038/nrd2653>.
- (182) Haas, H. L.; Sergeeva, O. A.; Selbach, O. Histamine in the Nervous System. *Physiological Reviews* **2008**, *88* (3), 1183–1241. <https://doi.org/10.1152/physrev.00043.2007>.
- (183) Passani, M. B.; Panula, P.; Lin, J. S. Histamine in the Brain. *Frontiers in Systems Neuroscience* **2014**, *8* (APR), 1–2. <https://doi.org/10.3389/fnsys.2014.00064>.
- (184) Yanai, K.; Tashiro, M. The Physiological and Pathophysiological Roles of Neuronal Histamine: An Insight from Human Positron Emission Tomography Studies. *Pharmacology and Therapeutics* **2007**, *113* (1), 1–15. <https://doi.org/10.1016/j.pharmthera.2006.06.008>.
- (185) Collado, J. A.; Tuñón, I.; Silla, E.; Ramírez, F. J. Vibrational Dynamics of Histamine Monocation in Solution: An Experimental (FT-IR, FT-Raman) and Theoretical (SCRF-DFT) Study. *Journal of Physical Chemistry A* **2000**, *104* (10), 2120–2131. <https://doi.org/10.1021/jp994084d>.
- (186) Nagy, P. I.; Durant, G. J.; Hoss, W. P.; Smith, D. A. Theoretical Analyses of the Tautomeric and Conformational Equilibria of Histamine and (AR, BS)- α,β -Dimethylhistamine in the Gas Phase and Aqueous Solution. *Journal of the American Chemical Society* **1994**, *116* (17), 7957. <https://doi.org/10.1021/ja00096a088>.
- (187) Ganellin, C. R.; Pepper, E. S.; Port, G. N. J.; Richards, W. G. Conformation of Histamine Derivatives. 1. Application of Molecular Orbital Calculations and Nuclear Magnetic Resonance Spectroscopy. *Journal of Medicinal Chemistry* **1973**, *16* (6), 610–616. <https://doi.org/10.1021/jm00264a007>.
- (188) Ham, N. S.; Casy, A. F.; Ison, R. R. Solution Conformations of Histamine and Some Related Derivatives. *Journal of Medicinal Chemistry* **1973**, *16* (5), 470–475. <https://doi.org/10.1021/jm00263a011>.
- (189) Bonnet, J. J.; Ibers, J. A. The Structure of Histamine. *Journal of the American Chemical Society* **1973**, *95* (15), 4829–4833. <https://doi.org/10.1021/ja00796a011>.
- (190) Cole, L. B.; Holt, E. M. Histamine Complexation: Structural Studies of $[\text{CaCl}_4(\text{H}_2\text{O})_2\text{CaCl}_2(\text{H}_2\text{O})_2(\text{Histamine})_2]$ and Histamine Hydrobromide. *Journal of the Chemical Society, Perkin Transactions 1* **1986**, No. 20, 151.

<https://doi.org/10.1039/p19860000151>.

- (191) Veidis, M. V.; Palenik, G. J.; Schaffrin, R.; Trotter, J. Crystal Structure of Histamine Diphosphate Monohydrate. *Journal of the Chemical Society A: Inorganic, Physical, and Theoretical Chemistry* **1969**, 2659–2666. <https://doi.org/10.1039/J19690002659>.
- (192) Louhibi, S.; Belfilali, I.; Boukli-Hacene, L.; Roisnel, T. Crystal Structure of 2-(1H-Imidazol-3-yl)ethanaminium Dichloride, a Re-Determination. *Acta Crystallographica Section E: Crystallographic Communications* **2015**, 71 (3), o844–o845. <https://doi.org/10.1107/S2056989015018848>.
- (193) Raczyńska, E. D.; Darowska, M.; Cyrański, M. K.; Makowski, M.; Rudka, T.; Gal, J.-F.; Maria, P. Ab Initio Study of Tautomerism and of Basicity Center Preference in Histamine, from Gas Phase to Solution— Comparison with Experimental Data (Gas Phase, Solution, Solid State). *Journal of Physical Organic Chemistry* **2003**, 783–796. <https://doi.org/10.1002/poc.670>.
- (194) Mukherjee, V.; Yadav, T. Conformational Study of Neutral Histamine Monomer and Their Vibrational Spectra. *Spectrochimica Acta - Part A: Molecular and Biomolecular Spectroscopy* **2016**, 165, 167–175. <https://doi.org/10.1016/j.saa.2016.04.041>.
- (195) Vianello, R.; Mavri, J. Microsolvation of the Histamine Monocation in Aqueous Solution: The Effect on Structure, Hydrogen Bonding Ability and Vibrational Spectrum. *New Journal of Chemistry* **2012**, 36 (4), 954–962. <https://doi.org/10.1039/c2nj20877f>.
- (196) Wimmer, M.; Palma, J. L.; Tarakeshwar, P.; Mujica, V. Single-Molecule Conductance through Hydrogen Bonds: The Role of Resonances. *Journal of Physical Chemistry Letters* **2016**, 7 (15), 2977–2980. <https://doi.org/10.1021/acs.jpcllett.6b01318>.
- (197) Xu, B.; Xiao, X.; Tao, N. J. Measurements of Single-Molecule Electromechanical Properties. *Journal of the American Chemical Society* **2003**, 125 (52), 16164–16165. <https://doi.org/10.1021/ja038949j>.
- (198) Ren, X.; Rinke, P.; Blum, V.; Wieferink, J.; Tkatchenko, A.; Sanfilippo, A.; Reuter, K.; Scheffler, M. Resolution-of-Identity Approach to Hartree-Fock, Hybrid Density Functionals, RPA, MP2 and GW with Numeric Atom-Centered Orbital Basis Functions. *New Journal of Physics* **2012**, 14. <https://doi.org/10.1088/1367-2630/14/5/053020>.
- (199) Li, C.; Pobelov, I.; Wandlowski, T.; Bagrets, A.; Arnold, A.; Evers, F. Charge

Transport in Single Au | Alkanedithiol | Au Junctions: Coordination Geometries and Conformational Degrees of Freedom. *Journal of the American Chemical Society* **2008**, *130* (1), 318–326. <https://doi.org/10.1021/ja0762386>.

- (200) Paulsson, M.; Krag, C.; Frederiksen, T.; Brandbyge, M. Conductance of Alkanedithiol Single-Molecule Junctions: A Molecular Dynamics Study. *Nano Letters* **2009**, *9* (1), 117–121. <https://doi.org/10.1021/nl802643h>.
- (201) Desiraju, G.; Steiner, T. *The Weak Hydrogen Bond*; Oxford University Press, 2001. <https://doi.org/10.1093/acprof:oso/9780198509707.001.0001>.
- (202) Steiner, T. The Hydrogen Bond in the Solid State. *Angewandte Chemie International Edition* **2002**, *41* (1), 48–76. [https://doi.org/10.1002/1521-3773\(20020104\)41:1<48::AID-ANIE48>3.0.CO;2-U](https://doi.org/10.1002/1521-3773(20020104)41:1<48::AID-ANIE48>3.0.CO;2-U).
- (203) Jeffrey, G. A. *An Introduction to Hydrogen Bonding*; Oxford University Press, **1997**.

CURRICULUM VITAE**EDUCATION**

Boston University, Graduate School of Arts and Sciences (Boston, MA)
Doctor of Philosophy – Ph.D., Chemistry Aug 2023

Boston University, College of Engineering (Boston, MA)
Master of Science, Materials Science and Engineering May 2019

Pennsylvania State University (State College, PA)
Bachelor of Science, Materials Science and Engineering May 2017

Minor Biomedical Engineering

PROFESSIONAL EXPERIENCE

Graduate Research Assistant March 2018 – Present
Boston University Kamenetska Group (Boston, MA)

Research Chemist Aug 2016 – July 2017
PPG Inc., Coatings Innovation Center (State College, PA)

Undergraduate Research Assistant October 2015 – May 2017
Penn State Kim Group, Glass Surface Science Research (State College, PA)

PUBLICATIONS

1. Lin, Y., Gao, T., Pan, X., Kamenetska, M. & Thon, S. M. Local Defects in Colloidal Quantum Dot Thin Films Measured via Spatially Resolved Multi-Modal Optoelectronic Spectroscopy. *Advanced Materials*. 32, 1–12 (2020).

2. Pan, X., Lawson, B., Rustad, A. M. & Kamenetska, M. pH-Activated Single Molecule Conductance and Binding Mechanism of Imidazole on Gold. *Nano Letters*. 20, 4687–4692 (2020).
3. McNeely, J., Miller, N., Pan, X., Lawson, B. & Kamenetska, M. Angstrom-Scale Ruler Using Single Molecule Conductance Signatures. *The Journal of Physical Chemistry C*. 124, 13427–13433 (2020).
4. Pan, X., Qian, C., Chow, A., Wang, L., Kamenetska, M. Atomically precise binding conformations of adenine and its variants on gold using single molecule conductance signatures. *The Journal of Chemical Physics*. 157, 234201 (2022).
5. Skipper, H. E., Lawson, B., Pan, X., Degtiareva, V., Kamenetska, M., Manipulating Quantum Interference Between σ and π Orbitals in Single Molecule Junctions via Chemical Substitution and Environmental Control. *ACS Nano*. ASAP.
6. Pan, X., Montes, E., Rojas, W., Lawson, B., Héctor, V., Kamenetska, M. Cooperative self-assembly of dimer junctions driven by π -stacking leads to conductance enhancement. *Nano Letters*. ASAP.
7. Pan, X., Matthews, K., Lawson, B., Kamenetska, M. Single Molecule Conductance Signature of Intramolecular Hydrogen Bonding in a Histamine Bound on Gold. In preparation.

CONFERENCE PRESENTATIONS

"Single Molecule Conductance and Binding Orientation of Adenine on Gold" Pan, X., Kamenetska., M; American Chemical Society 261st National Meeting, April 5-16, 2021, Virtual.

"Single Molecule Detection of Metal-Biomolecule Binding Conformations Using Conductance Signatures" Pan, X., Kamenetska., M; Materials Research Society national spring meeting, April 10-14, 2023, San Francisco, California.

TEACHING AND MENTOR EXPERIENCES

Student Mentor

Boston University & Haverford College Research Experience for Undergraduates (REU)

Summer 2021

Greater Boston Area Research Opportunities for Young Women (GROW)

Summer 2020

Boston University Undergraduate Research Opportunities Program (UROP)

Spring 2019

Teach Fellow

General Chemistry for Engineering Sciences

Fall 2019

General Chemistry

Summer 2020